



**BERGISCHE
UNIVERSITÄT
WUPPERTAL**

Lightning Detection at the
Pierre-Auger-Observatory

Dissertation
zur Erlangung des Grades
eines Doktors der Naturwissenschaften

dem Fachbereich Physik
der Bergischen Universität Wuppertal

vorgelegt von
Lukas Niemietz
aus
Bonn

Wuppertal, 08. Juni 2017

Die Dissertation kann wie folgt zitiert werden:

urn:nbn:de:hbz:468-20171012-105730-3

[<http://nbn-resolving.de/urn/resolver.pl?urn=urn%3Anbn%3Ade3A468-20171012-105730-3>]

1. Gutachter:

Prof. Dr. Karl-Heinz Kampert
Bergische Universität
Wuppertal

2. Gutachter:

Dr. Hernán Asorey
Universidad Nacional
de Río Negro (UNRN)

Contents

| | | |
|----------|---------------------------------------------------|-----------|
| 1 | Introduction | 1 |
| 2 | Cosmic Rays | 3 |
| 2.1 | Energy Spectrum | 5 |
| 2.2 | Chemical Composition | 6 |
| 2.3 | Acceleration and Possible Sources | 8 |
| 2.3.1 | Bottom-Up Models | 9 |
| 2.3.2 | Top-Down Models | 12 |
| 2.4 | Propagation | 12 |
| 2.5 | Anisotropy | 15 |
| 3 | Extensive Air Showers | 17 |
| 3.1 | Shower Development | 17 |
| 3.2 | Shower Components | 20 |
| 3.3 | Observation Methods | 22 |
| 3.3.1 | Surface Detectors | 22 |
| 3.3.2 | Fluorescence Detectors | 24 |
| 3.3.3 | Radio Detection | 25 |
| 3.3.4 | Additional Detection Techniques | 28 |
| 4 | The Pierre-Auger-Observatory | 29 |
| 4.1 | Fluorescence Detector | 30 |
| 4.2 | Surface Detector | 32 |
| 4.3 | Auger Engineering Radio Array | 33 |
| 4.4 | Offline Framework | 36 |
| 5 | Lightnings | 37 |
| 5.1 | General Information | 37 |
| 5.2 | Detection Techniques | 42 |
| 5.3 | Relativistic Runaway Electron Avalanche | 42 |
| 5.4 | Radio Emission | 44 |

CONTENTS

| | | |
|----------|----------------------------------------------------------|------------|
| 5.5 | Transient Luminous Events | 45 |
| 6 | Lightning Detection Devices | 49 |
| 6.1 | E-Field Mill | 49 |
| 6.1.1 | Detection Mechanism | 49 |
| 6.2 | Lightning Detection System | 53 |
| 6.2.1 | Data Acquisition | 53 |
| 6.2.2 | Sampling Rate Measurement | 54 |
| 6.2.3 | Timing | 57 |
| 6.2.4 | GPS-Extension for Boltek StormTracker | 60 |
| 6.2.5 | Dead Time | 64 |
| 6.3 | Integration in the Auger Monitoring Page | 65 |
| 6.4 | AERA-Stations | 73 |
| 6.4.1 | Implementation of Cross-Correlation in Offline | 74 |
| 6.4.2 | Data Analysis | 75 |
| 6.5 | SD Lightning Flag | 77 |
| 7 | Accuracy of Lightning Position | 79 |
| 8 | Lightning Data Comparison | 87 |
| 8.1 | CheckUp-System in Germany | 87 |
| 8.1.1 | Number of Triggers | 88 |
| 8.1.2 | Direction | 90 |
| 8.1.3 | Distance | 92 |
| 8.1.4 | Cable Length | 92 |
| 8.2 | SD Lightning Flag | 93 |
| 8.2.1 | Timing | 93 |
| 8.2.2 | Reconstruction Position | 96 |
| 8.2.3 | Uptime and Detection Rate | 97 |
| 8.3 | World Wide Lightning Location Network | 99 |
| 8.3.1 | Timing | 99 |
| 8.3.2 | Uptime and Detection Efficiency | 102 |
| 8.3.3 | Reconstruction Position | 109 |
| 8.4 | E-Field Mill | 112 |
| 8.4.1 | Comparison of the E-Field Mills to each other | 112 |
| 8.4.1.1 | E-Field Value | 112 |
| 8.4.1.2 | IsTS-Flag Correlation | 113 |
| 8.4.2 | Comparison to SD Lightning Flag | 116 |
| 8.4.3 | Comparison to Lightning Detection System | 120 |
| 9 | SD Lightning Trigger | 125 |

CONTENTS

| | |
|-------------------------------------------------|------------|
| 10 Outlook | 127 |
| 10.1 Additional Lightning Information | 127 |
| 10.1.1 Polarisation | 127 |
| 10.1.2 Lightning Strength | 128 |
| 10.2 Interpolation | 128 |
| 10.3 Elves | 128 |
| 10.4 SD-Rings | 130 |
| 11 Summary | 133 |
| Appendix | 137 |
| A MySQL Table Structure | 139 |

Chapter 1

Introduction

Since the discovery of cosmic rays by Victor F. Hess in 1912 scientists all over the world study cosmic rays, but there are still open fundamental questions:

- Where do the cosmic rays come from?
- How are the particles accelerated?
- Is there an maximum energy the particles can achieve?

Today, over 100 years later, these questions have still not been clarified. That's why there are numerous projects which get the bottom of these matters. By measuring the flux, the direction and the chemical composition of the particles reaching the detectors scientists try to get answers and a better understanding of the high energy cosmic rays.

The world's largest detector for the study of high energy cosmic rays is the Pierre Auger Observatory in the Argentinean Pampa Amarilla. With this hybrid detector, consisting of 1660 water Cherenkov detectors and 27 fluorescence telescopes, particle showers are investigated at energies above 10^{18} eV. The large exposure of the surface detectors (SD), which detects the lateral distribution of secondary particles, in combination with the precise measurements of the longitudinal shower development measured by the fluorescence detectors (FD) provide a unprecedented high quality dataset.

On the one hand to lower the energy threshold, on the other hand to gain additional information of the chemical composition, several extensions, like the HEAT extension for the FD, tilted standard FD-telescopes with a higher field of view, the Infill area, SD-detectors with a smaller spacing of the detectors or the AMIGA counters, muon counters burrowed under SD-detectors in the Infill area, were developed and deployed.

Another extension is the Auger Engineering Radio Array (AERA). A new detector type for the detection of air showers, based on radio pulses in the MHz range emitted during the propagation of the shower front through the atmosphere. The strength of the emitted signal is highly influenced by large electric fields, in particular, amplified signals up to an order of magnitude have been detected as an effect of thunderstorms. This makes it necessary to monitor the local atmospheric conditions. For a more detailed investigation and the detection of thunderstorms, within this thesis a new lightning detection system has been developed. In addition, electric field mills measure the electric field strength at ground level at the antenna array. With these measurements, data periods can be classified for their influence by thunderstorms.

A general overview of cosmic rays will be given in chapter 2. Chapter 3 is about the development of extensive air showers (EAS) and the detection methods, while chapter 4 describes the Pierre Auger Observatory. General information on lightnings are provided in chapter 5. The lightning detection systems at the Pierre Auger Observatory are introduced in chapter 6 and it is shown how they are integrated in the Auger monitoring. The expectable accuracy of the new lightning detection system will be determined in chapter 7, while in chapter 8 the different lightning detection methods will be compared to each other. An new SD-Trigger based on the lightning detection system is presented in chapter 9. Finally chapter 10 and 11 will give a short outlook for future analyses and a summary of the thesis.

Chapter 2

Cosmic Rays

Cosmic rays are under investigation for more than 100 years. In general Cosmic Rays can be all particles originating from astrophysical sources and propagating through the interstellar medium to Earth, but we mostly refer only to the charged particles. These particles can be detected and categorized by their energy and the chemical composition. The energy spectrum, especially the low energetic part, which can be detected directly from space, is well understood. But the high energy part, where only indirect measurements are possible, still keeps fundamental open questions. This section will give a brief overview of the current state of knowledge for the particles with the highest energies.

The story of cosmic rays began in 1900. Wilson, Elster and Geitel dealt with the residual conductivity of air. For this purpose they set up electroscopes, which measure charges and determined the time that was required for a discharge of the electroscopes. Rutherford discovered in 1903, that this time can be extended by shielding the electroscopes with lead plates. Because of this, it was assumed, that a radioactive background radiation ionizes the air, which leads to the discharge. Terrestrial radiation originating from ores in the ground should be the reason for this background radiation. Wulf confirmed this hypothesis in 1910 in an experiment at the Eiffel Tower in Paris. He measured that the intensity of the background radiation decreases up to the height of 267 meters with the altitude, but it was still higher than expected.

In 1912 Victor F. Hess concluded, that there must be an extra-terrestrial component of background radiation on Earth, by measuring the intensity of the ionization as a function of height during balloon flights up to a height 5 km. As expected, the intensity initially decreased, but from an altitude



Figure 2.1: Hess in the balloon basket [2].

of about 1000 meters increased again [1]. For the discovery of the *Cosmic Radiation* he received the Nobel price in 1936.

Three years later Pierre Auger discovered in the Swiss alp events coincident in time of detectors with a spacing of 300 m. He concluded, that not single particles reach the detectors, but a cascade of secondary particles. These can be generated if the energy of the primary particle is high enough [3]. Chapter 3 will focus on so-called extensive air showers (EAS).

Cosmic rays played also a big role in the understanding of the standard model of particle physics. Anderson proved 1932 in a cloud chamber for the first time the existence of the positron, the antiparticle of the electron [4]. 1937 followed the discovery of the muon as part of cosmic rays [5].

2.1 Energy Spectrum

The energy spectrum of cosmic rays, Fig. 2.2, describes the particle flux with respect to their energy, starting with an energy of about 10^6 eV extending up to more than 10^{20} eV, an energy much larger than of man made particle accelerators, as well as a flux ranging over 32 decades. Because of the huge variation in the flux of about one particle per second and m^2 at energies of $\sim 10^{11}$ eV to only one particle per century and km^2 at the highest energies it is a challenging measurement. The low energy particles can be detected in direct measurements, for example in balloons or from space to reduce the absorption of the atmosphere, while at the highest energies the particles can be only detected indirectly on ground by their secondary particles as described in chapter 3.

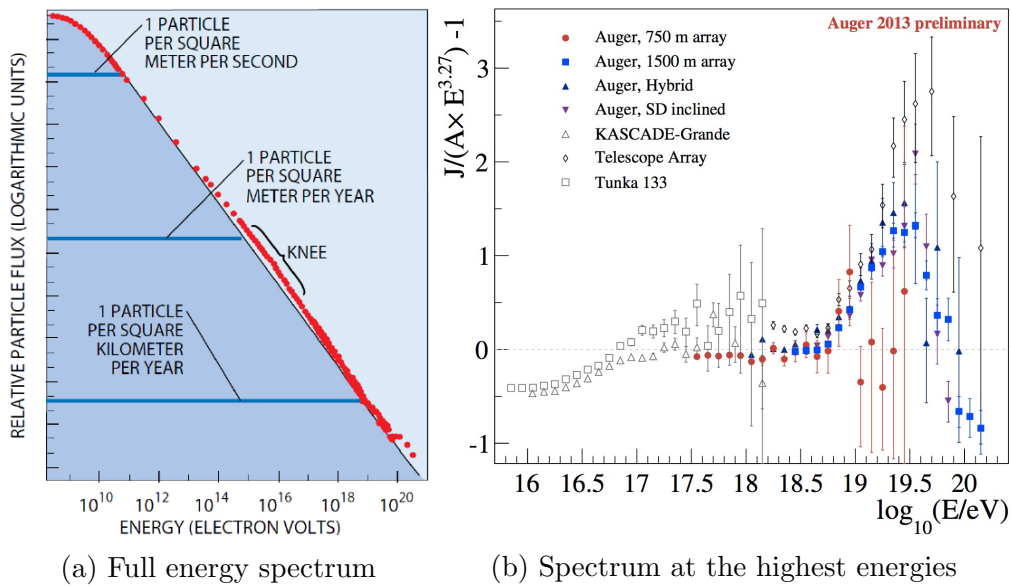


Figure 2.2: a) the full energy spectrum in a double logarithmic plot, from [8] and b) zooms to the data at the highest energies of different experiments folded with the energy to the power of 3.27, from [9].

The flux of the cosmic rays decreases continuously with the energy. The differential flux can be described by an power law:

$$\frac{dE}{dN} \propto E^{-\gamma}. \quad (2.1)$$

The spectrum can be divided into three parts: First, the area to the so-called knee at about $3 \cdot 10^{15}$ eV with a spectral index of $\gamma \approx 2.7$, the area from the

knee to the ankle at about $4 \cdot 10^{18}$ eV with a spectral index of $\gamma \approx 3.0$, and the region beyond the ankle with a again lower spectral index of $\gamma \approx 2.6$. The change in the knee region can be explained by the acceleration processes of the particles. The galactic sources are not able to accelerate the lighter particles to higher energies [10]. For the change in the ankle region there are different explanations. The most common one is the transition from galactic to extragalactic component of the cosmic ray composition [11]. Another approach is the so called *dip model*, the high energetic protons lose energy due to e^\pm pair production during their propagation [12].

At the highest energies above $\sim 6 \cdot 10^{19}$ eV a suppression is observed which can be explained with the expectations of Greisen [13], Zatsepin and Kuzmin [14], who calculated a cut off due to the interaction of high energetic protons with the 2.7 K background radiation (*GZK-cut off*), see section 2.4.

Due to the steep falling of the energy spectrum, all described features are easier to see by scaling the spectrum with the energy to a power of ~ 3 , as in Fig. 2.2b, which shows the results of different experiment.

2.2 Chemical Composition

Since the low-energy particles are dominant due to the strong decrease of the particle flux, the composition of the charged component can be determined very good in direct measurement, for example by satellite measurements. It consists to 98% of atomic nuclei and 2% of electrons. While the atomic nuclei are mostly protons (85%) and α -particles (12%). The remaining 3% comes from heavier nuclei with an atomic number $Z \geq 3$.

Comparing the frequency of elements in cosmic rays with the abundance of the elements in our solar system, Fig. 2.3, the two curves look similar to each other. However, there are significant deviations. Cosmic rays show an excess of lithium ($Z = 3$), beryllium ($Z = 4$), and boron ($Z = 5$) as well as the elements having an atomic number just below iron ($Z = 26$). Suppose the origin of the solar and cosmic matter is the same, it is possible to explain this behavior with the spallation of heavier nuclei as carbon ($Z = 8$) during the propagation through the interstellar medium to Earth. They can interact with other particles, burst and divide to cores with smaller atomic numbers.

Due to the low particle flux at the higher energies direct measurements of the chemical composition are not possible, but there are observables of the secondary particles from the EAS (chapter 3) which give indications to the primary particles. But these observables suffer of course from statistical fluctuations as well as systematic uncertainties.

2.2. CHEMICAL COMPOSITION

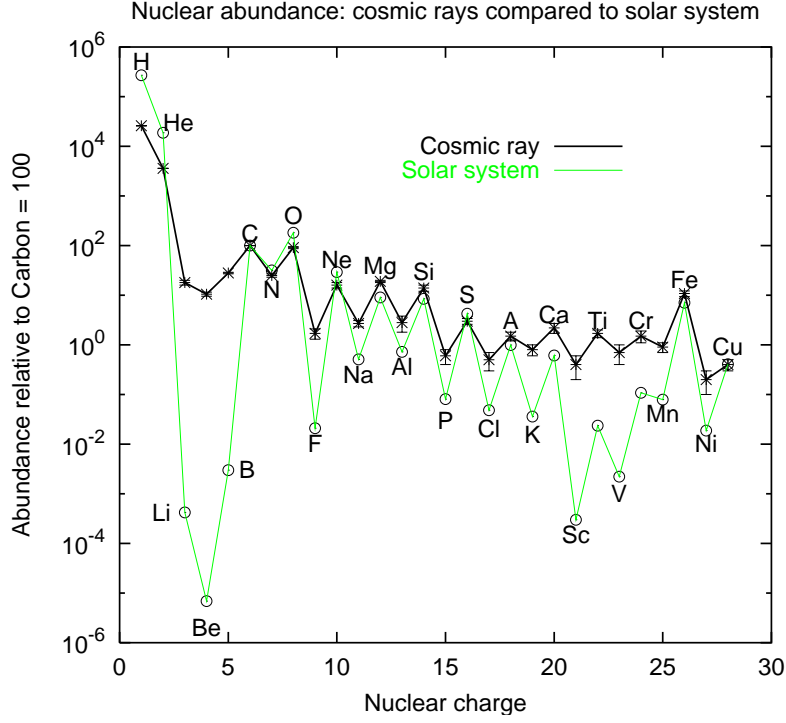


Figure 2.3: Relative abundances of chemical elements on Earth and in the cosmic ray composition normalized to carbon, from [15].

The logarithmic mass, defined as:

$$\langle \ln A \rangle = \sum r_i \ln A_i, \quad (2.2)$$

with r_i as the relative fraction of the atomic nuclei A_i , is a often used quantity to characterize the composition. In air shower experiments $\langle \ln A \rangle$ can be obtained by two approaches. First by measuring the ratio of electrons and muons on ground level:

$$\langle \ln A \rangle \propto \log_{10} \left(\frac{N_\mu}{N_e} \right), \quad (2.3)$$

or by observing the shower maximum X_{\max} , which will be discussed in more detail in section 3.1:

$$X_{\max} \propto \left\langle \ln \frac{E}{A} \right\rangle. \quad (2.4)$$

The average X_{\max} measurements with respect to the primary energy E_0 of different experiment are shown in Fig. 2.4. In addition, the expectations for

simulations with different interaction models for pure protons and pure iron nuclei as primary particle are plotted. Below the knee ($\sim 4 \cdot 10^{15}$ eV) the composition gets lighter as function of the energy. Between $\sim 4 \cdot 10^{15}$ eV and $\sim 4 \cdot 10^{16}$ eV the composition changes to heavier nuclei, which can be explained with breaks in the energy spectra for the elements from light to heavy nuclei [16]. Above $\sim 4 \cdot 10^{17}$ eV the composition changes slowly to lighter nuclei again.

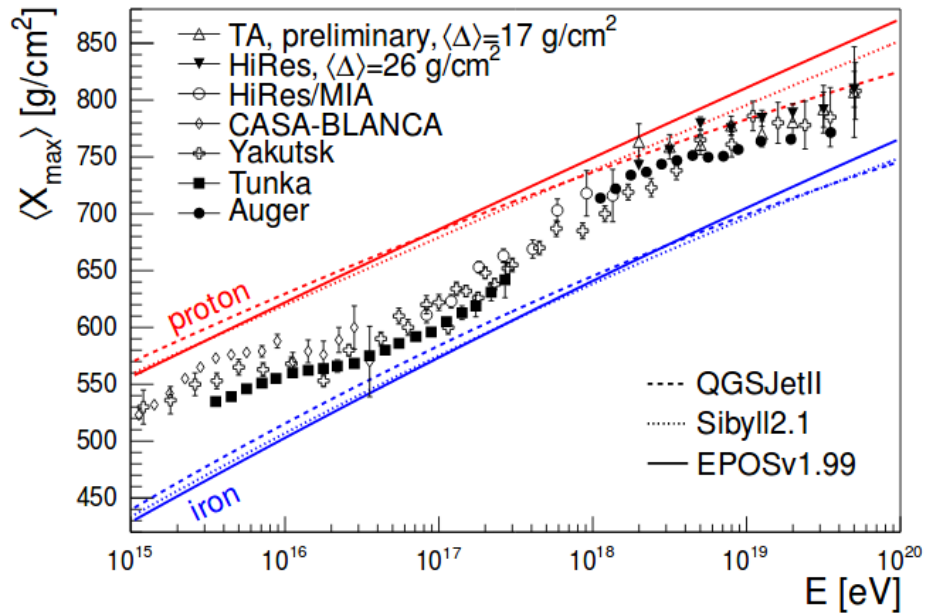


Figure 2.4: Average depth of the shower maximum X_{\max} as function of primary energy, from [17].

For the highest energies the composition is not measured to a highly certainty, due to the low flux in the ultra-high energy range. But the recent results from the Pierre Auger Observatory indicate a transition back to heavier elements for energies larger than $\sim 10^{19}$ eV, Fig. 2.5.

2.3 Acceleration and Possible Sources

After describing the energy spectrum of cosmic rays, the focus of this section is the origin and the acceleration process of the particles. This question is over 100 years of studying cosmic rays and lots of research not solved up to now. But there are different approaches which can explain the origin and the energy spectrum of the high energetic particles. First the *bottom-up*

2.3. ACCELERATION AND POSSIBLE SOURCES

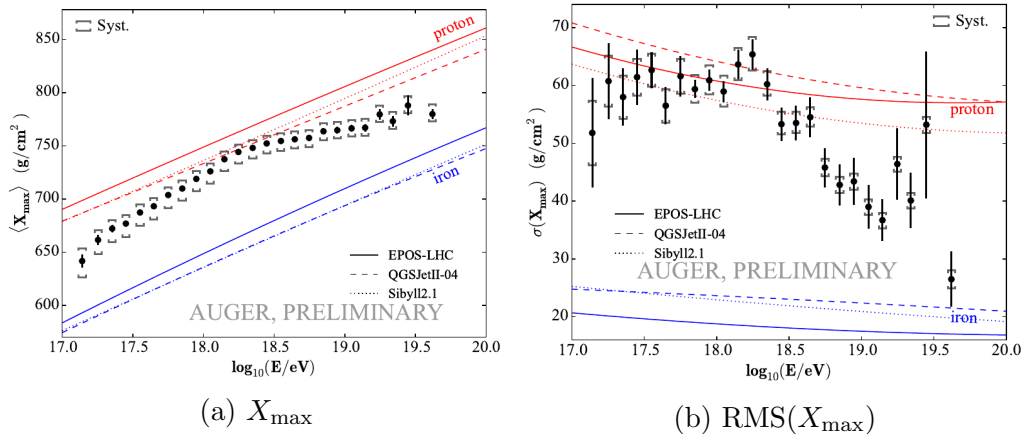


Figure 2.5: Measurements of X_{\max} (a) and $\text{RMS}(X_{\max})$ of the Pierre Auger Observatory as function of the energy of the primary particle E_0 , from [18]. In addition the predictions for pure proton and iron primary from different interaction models are drawn.

models, where low energetic particles get accelerated to the highest energies, and second the *top-down models*, where exotic particles decay into very high energetic particles.

2.3.1 Bottom-Up Models

The most prominent candidate of the bottom-up mechanism is the Fermi acceleration, which was proposed by Enrico Fermi in 1949 [19]. In this stochastic model particles gain or lose energy during their propagation through interstellar medium by interacting with magnetic clouds, which move with random direction and velocity.

Consider an energy gain of $\Delta E = \xi E$ by encountering a magnetized cloud. This results in the energy E_n of the particle after n encounters and an injection energy E_0 :

$$E_n = E_0(1 + \xi)^n. \quad (2.5)$$

This leads to:

$$n = \frac{\ln(E_n/E_0)}{\ln(1 + \xi)}. \quad (2.6)$$

If the probability P_{esc} , that a particle leaves the system after a collision, is constant, then the probability of a particle to encounter n times is $(1 - P_{\text{esc}})^n$.

Thus, the number of particles with an energy above E_n can be estimated by:

$$N(E_n) = N(E > E_n) = N_0 \sum_{m=n}^{\infty} (1 - P_{\text{esc}})^m \propto \frac{1}{P_{\text{esc}}} \left(\frac{E}{E_0} \right)^{-\gamma}, \quad (2.7)$$

with:

$$\gamma = \frac{\ln(1/(1 - P_{\text{esc}}))}{\ln(1 + \xi)} \approx \frac{P}{\xi}. \quad (2.8)$$

This results naturally in a power law for the energy spectrum from the stochastic acceleration.

Fermi argued, that for particles the probability for head on collisions is higher, than a head tail collision to a magnetic cloud, which leads in total to an acceleration. For this so-called *second order Fermi acceleration* scenario, can be shown, that the fractional energy gain per cycle is

$$\xi \propto \frac{4}{3} \beta^2 E, \quad (2.9)$$

with β as the velocity of the magnetic cloud in units of the speed of light [20]. Thus the energy gain of this mechanism is only second order, it takes a long time to accelerate particles to the highest energies.

In the 1970's another mechanism was proposed by Blandford and Ostriker [21]. Based on the inefficient mechanism, the acceleration is not due encountering magnetized clouds, but plane shock fronts. Behind the shock front, the gas expands slower than the shock front itself. The velocity of the shock front v_s is greater than the velocity of the gas v_g and it applies: $v_s = \frac{4}{3} v_g$. If a shock front spreads out in the interstellar medium (ISM) at the speed v_s , the ISM flows in the rest frame of the shock front with $u_1 = v_s$ to the shock front and behind the shock front with a smaller velocity u_2 . In the laboratory system the gas moves behind it away from the shock front at a velocity of $u_1 - u_2$ and the matter before the shock front passes with u_1 the shock front.

Some particles of the ISM flow away with matter behind the shock front, others are backscattered and encounter the shock front again. By averaging over again all possible angles, we obtain a fractional energy change per crossing of the shock front of:

$$\xi \propto \frac{4}{3} \beta E. \quad (2.10)$$

Since the energy gain is proportional to β this mechanism is called *first order Fermi acceleration* and it is much more efficient than the second order Fermi

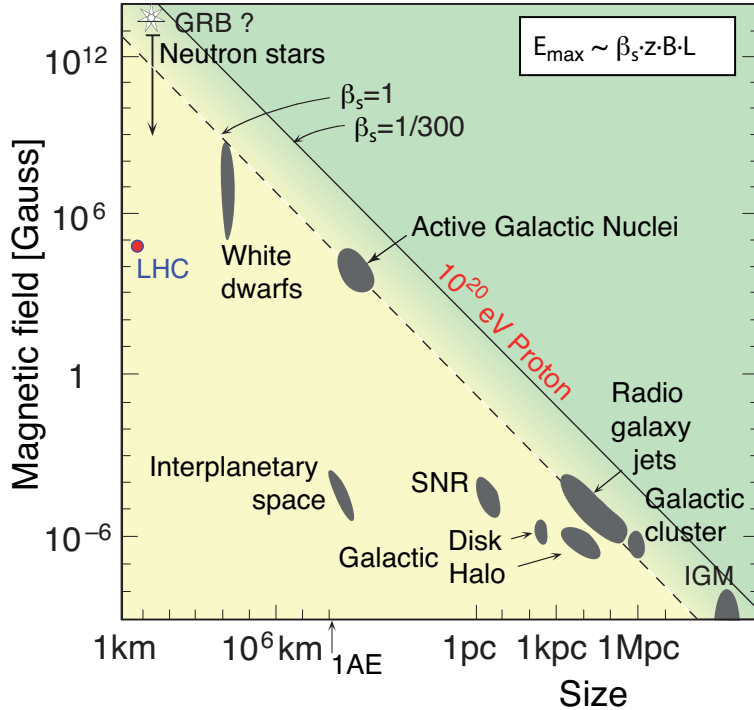


Figure 2.6: The *Hillas Plot* shows source candidates of high energetic cosmic rays. The magnetic field of the sources is drawn against their size. The candidates have to lie on or above the diagonal line to reach maximum energies of 10^{20} eV, assuming a shock velocity of $\beta = 1$ for the dashed and $\beta = 1/300$ for the solid line, from [22], according to [11].

acceleration, since $\beta < 1$.

Taking both acceleration models into account the particles can only be accelerated, if they are within the acceleration region. Particles can only be kept inside the acceleration region, if the size of the region L is larger than the Larmor radius r_L of the particle $r_L < L$. This leads to a maximum energy which can be achieved proportional to L and the magnetic field B of the source:

$$E_{\max} \approx \frac{1}{2} \frac{B}{\mu\text{G}} \frac{L}{\text{kpc}} \beta_s \cdot Z \cdot 10^{18} \text{ eV} \quad (2.11)$$

with the shock velocity β_s and the atomic number Z , which was firstly summarized by Hillas [11]. In a diagram of the magnetic field strength against the size of source candidates for high energetic cosmic rays results in the so called *Hillas Plot*, which is shown in Fig. 2.6. The sources have to lay on or

above diagonal line to be able to accelerate particles up to 10^{20} eV. Only a few remain as source candidates: Active galactic nuclei (AGN), gamma ray bursts (GRB), neutron stars and radio galaxy jets.

AGNs are the most favoured source of Ultra High Energy Cosmic Rays (UHECR). Considering them as the source of UHERC would result in a correlation of the arrival directions of cosmic rays and the near by AGNs. This correlation study was performed at the Pierre Auger Observatory, see section 2.5.

For a detailed description of the sources see [23].

2.3.2 Top-Down Models

In contrast to the bottom-up models, where low energetic particle get slowly accelerated to high energies, in the top down models the particles originate from the decay of super-massive particles X with masses $m_X > 10^{20}$ eV. These are assumed to be relicts of high energetic processes in the beginning of the universe. There are several candidates, as topological defects [24, 25], super heavy dark matter [26, 27], QCD fragmentation [28] or the Z-burst model [29–31]. The X particles mostly decay to quarks and leptons and the quarks produce hadronic jets mostly consisting of mesons (pions), with a low fraction of baryons (nucleus). The pions itself decay afterwards to electrons (e^\pm), neutrinos ($\nu\bar{\nu}$) and photons (γ) [32]. Due to the high fraction of photons and the experimental limits on the photon flux [33] these models are highly disfavored in comparison to the bottom-up models.

2.4 Propagation

Due to magnetic fields the particles are deflected on their way to Earth, after leaving the source regions. The magnetic field within our galaxy are known to be mostly uniform with a value of a few μG over the range of kpc. As already mentioned, with these field strengths and size high energetic particles can not be confined. Depending on their charge they leave the galaxy at different energies corresponding to their Larmor radius. With this the increase of the spectral index around the knee can be explained. The particles with higher energies may be from extragalactic sources.

The extragalactic magnetic fields are only poorly known, but are estimated to be in the region of nanogauss [34, 35]. The distance between galaxies are in the order of several 100 kpc, which lead to a huge deflection of the particles. Only the ultra-high energetic ones are slightly deflected.

There are not only the deflection by magnetic fields during the propagation of the particles, but also processes leading to energy losses.

In 1965 Penzias and Wilson discovered a signal at an antenna temperature of 3.5 K, during measurements with a horn antenna at the Crawford Hill location of Bell Telephone Laboratories, which they could not explain [36]. Later it turned out, that this is the cosmic microwave background (CMB), a relict of the beginning of the universe and was honored with the Nobel prize in 1978.

Protons with high enough energies are expected to interact with the photons of the CMB and create via a delta resonance pions, which results in a huge energy loss and makes the universe intransparent for these particles:

$$p + \gamma_{\text{CMB}} \longrightarrow \Delta^+(1232) \longrightarrow n + \pi^+ \quad (2.12)$$

$$p + \gamma_{\text{CMB}} \longrightarrow \Delta^+(1232) \longrightarrow p + \pi^0. \quad (2.13)$$

The energy threshold E_{th}^π for a head-on collision is defined as:

$$E_{\text{th}}^\pi = \frac{m_\pi(2m_p + m_\pi)}{4\epsilon} \simeq 6.8 \times 10^{19} \text{ eV}, \quad (2.14)$$

with the typical CMB photon energy of about 10 meV, the pion mass m_π , and the proton mass m_p . This cut-off was firstly proposed by Greisen [13], Zatsepin and Kuzmin [14] in 1966 and is called *GZK-suppression*.

Even for particles with lower energies, energy losses are possible due to e^\pm pair production, also called Bethe-Heitler process:

$$p + \gamma_{\text{CMB}} \longrightarrow p + e^+ + e^-. \quad (2.15)$$

The energy threshold E_{th}^e of this process is:

$$E_{\text{th}}^e = \frac{m_e(m_p + m_e)}{\epsilon} \simeq 4.8 \times 10^{17} \text{ eV}, \quad (2.16)$$

with the electron mass m_e and the proton mass m_p . The characteristic time for this process is in the order of 10^9 years, which makes the GZK-suppression dominant for the highest energies.

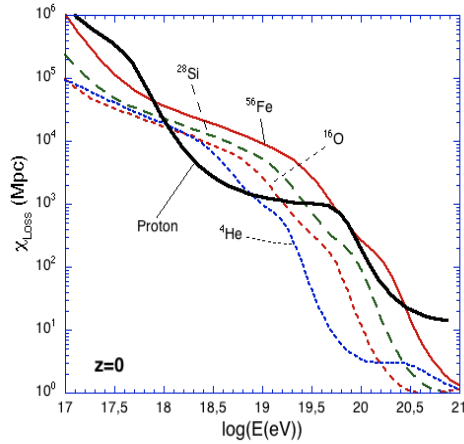


Figure 2.7: For different primary particles the attenuation length is given as function of the cosmic ray energy for redshift $z = 0$. The initiation of the Bethe-Heitler process and GZK-suppression at their respective energies are clearly visible for protons (solid black line), from [37].

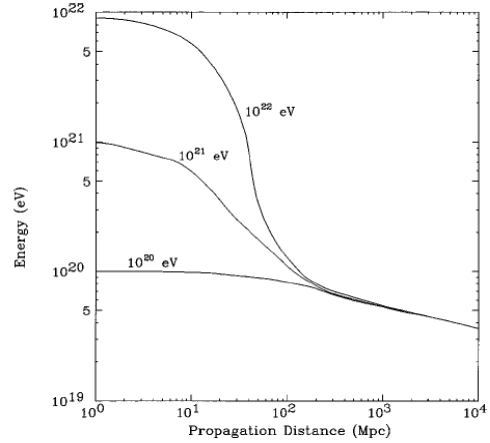


Figure 2.8: Development of the mean proton energy for different source energies E_0 , with respect to the propagation distance through the extragalactic CMB radiation, from [38].

Figure 2.7 shows the impact of the above mentioned processes to the attenuation length of different particle types. The decrease at the corresponding energies is clearly visible. Several experiments have measured particles with energies higher than 10^{20} eV, first the Volcano Ranch [39] experiment in 1966. Recent measurements of different experiments have shown a break in the flux of cosmic rays: HiRes at 6×10^{19} eV with 4σ significance [40] and the Pierre Auger Observatory at at $\sim 4 \times 10^{19}$ eV with 20σ significance [41].

The energy of a proton primary with respect to the propagation distance is shown in Fig. 2.8. For distance larger than 100 Mpc the energy averages for all primary particles, with energies larger than 10^{20} eV, to the same energy smaller than 10^{20} eV. The observation of particles larger than this cut-off energy implies, that the sources of UHECR must be near by the Earth.

2.5 Anisotropy

In section 2.4 it was mentioned, that for particles with lower energies no point sources within the Milky Way can be expected, due to the high deflection of magnetic fields. But it was also mentioned, that this deflection is much lower for the particles with the highest energies, which makes a search for point sources a promising approach to find possible sources of UHECR.

In 1998 an excess from the region of the Galactic Center and Centaurs A at energies of $\sim 10^{18}$ eV was found by the AGASA collaboration [42], which was later confirmed by SUGAR [43]. In contrast the Pierre Auger Collaboration could not confirm these discoveries [44].

In 2007 the Pierre Auger Collaboration performed an anisotropy analysis of AGN positions, taken from the Véron-Cetty & Véron catalog [45] within a distance cut in the red-shift of $z_{\max} < 0.017 \hat{=} D_{\max} < 75$ Mpc and the arrival direction of cosmic rays [46]. A significant correlation was found for energies $E_{\text{th}} = 5.7 \times 10^{19}$ eV. 8 of 13 events were correlated to the AGN positions within an angular window of $\psi = 3.1^\circ$. The isotropic expectations are 2.7 events (21%) which leads to a probability that this happens by chance of 1.7×10^{-3} . An update on the analysis in 2010 shows a lower correlation $37_{-6}^{+7}\%$ which is still above the isotropic expectation [47]. Figure 2.9 shows the used AGN

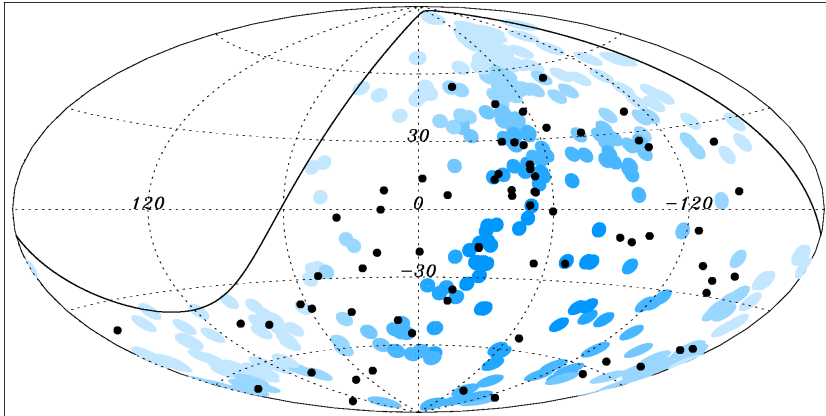


Figure 2.9: The arrival directions of CRs with energy $E \geq 55$ EeV detected by the Pierre Auger Observatory up to 31 December 2009 are plotted as black dots in galactic coordinates. The solid line represents the field of view of the Southern Observatory for zenith angles smaller than 60° . Blue circles of radius 3.1° are centred at the positions of the 318 AGNs in the VCV catalog that lie within 75 Mpc and that are within the field of view of the Observatory. Darker blue indicates larger relative exposure. The exposure-weighted fraction of the sky covered by the blue circles is 21%, from [47].

and the arrival directions of cosmic rays. The latest publication, based on almost 10 years Auger data, shows again a still lower correlated of $28.1_{3.6}^{3.8}\%$, which is only 2σ above the isotropic expectation of 21% [48]. This leads to the conclusion, that the previous results are affected by statistical fluctuation and does not any more allow the significant conclusion of anisotropy.

Other anisotropy tests in the same publication show no evidence for a non-isotropic distribution of UHECR. Figure 2.10 shows the result for a blind search for an excess in the visible sky. For varying radii of $1^\circ < \psi < 30^\circ$ on a $1^\circ \times 1^\circ$ grid the binomial probability to find an equal or larger amount of events in an isotropic flux than found in data were calculated. At the galactic coordinates $(l, b) = (-51.1^\circ, 37.6^\circ)$ with an window of 12° and an energy threshold of $E_{\text{th}} = 5.4 \times 10^{19}$ eV the lowest probability was found, which leads to a Li-Ma significance of 4.3σ . This excess is compatible to the maximum excess of isotropic simulations.

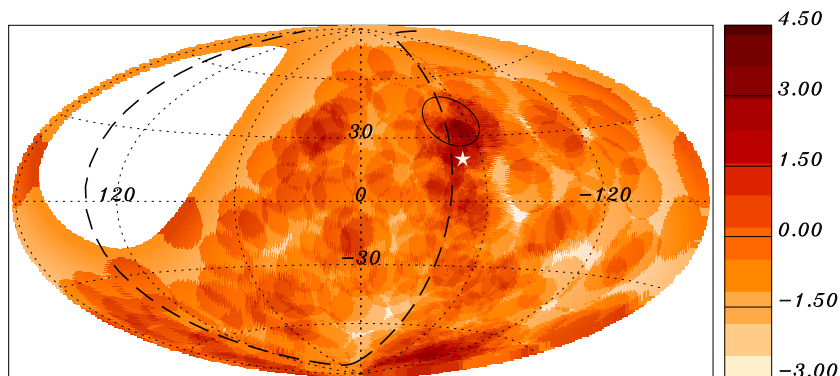


Figure 2.10: Map in galactic coordinates of the Li-Ma significances of overdensities in 12° -radius windows for the events with $E \geq 54$ EeV. The region with the highest significance, at longitude and latitude $(l, b) = (-51.1^\circ, 37.6^\circ)$, is marked with a black circle. Also indicated are the supergalactic plane (dashed line) and Centaurus A (white star), from [48].

Chapter 3

Extensive Air Showers

High energetic primary particles ($E > \sim 10^{14}$ eV), which reach the atmosphere, interact with air nuclei and generate secondary particles in these collisions. The energy is split to the generated particles, which themselves are high energetic enough to generate further generations of particles. This cascade of particles is called *extensive air showers* (EAS). The detection of EAS is, due to the low flux, the only practical way to measure particles with energies larger than 10^{14} eV. The discovery of EAS goes back to Pierre Auger, as described in the beginning of chapter 2, who detected, in a similar set up to Kohlhörster before, coincident events in detectors separated by up to 300 m.

3.1 Shower Development

These EAS propagate as a thin layer with a longitudinal thickness of some meters and a lateral radius, depending on the energy of the primary particle, up to several km with almost the speed of light through the atmosphere.

The transversed matter of the particles is of course an important parameter, which is called *slant depth*, X , and measured in g/cm^2 from the top of the atmosphere. The transversed matter is related to the density profile ρ_h of the atmosphere and has to be corrected for the zenith angle θ of the incoming particle:

$$X = \frac{X_v}{\cos(\theta)}, \quad (3.1)$$

with X_v as the transversed atmospheric depth:

$$X_v = \int_h^\infty \rho(h') dh'. \quad (3.2)$$

CHAPTER 3. EXTENSIVE AIR SHOWERS

The Heitler-Model is a very simple toy-model for the development of EAS [49]. In this model a primary particle generates after one interaction length λ a secondary particle and splits the primary energy E_0 to both particles $E_1 = E_0/2$, figure 3.1. As long as the remaining energy of each particle E_i is larger than the critical energy E_C after each interaction length secondary particles will be generated. For the number of particles N and the energy of the particles E_i within the shower after an atmospheric depth X applies as long as $E_i > E_C$:

$$N(X) = 2^{X/\lambda}, \quad (3.3)$$

$$E_i(X) = \frac{E_0}{N(X)} = \frac{E_0}{2^{X/\lambda}}. \quad (3.4)$$

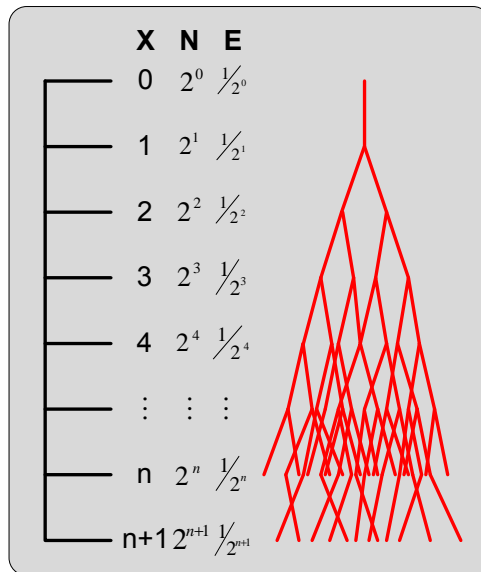


Figure 3.1: Heitler-Model of the shower development. E: energy of the single particles, N: number of particles, X: atmospheric slant depth X/λ , modified from [6].

If the energy of the single particles is equal to the critical energy, the shower has reached the maximum number of particles:

$$N_{\max} = \frac{E_0}{E_C}. \quad (3.5)$$

3.1. SHOWER DEVELOPMENT

The slant depth at this point is:

$$X_{\max} = \lambda \cdot \log_2 \left(\frac{E_0}{E_C} \right). \quad (3.6)$$

This model represents the processes very simplified, but it provides information about essential things. On the one hand, that the number of particles in a shower is approximately proportional to the primary energy and, secondly, that the X_{\max} logarithmically increases with the primary energy.

The dependence of the slant depth on the mass of the primary particle can be understood easily. Considering heavier nuclei with mass number A , so the energy is distributed among all nuclides and the energy of a single core particle is E_0/A . It follows that heavier nuclei forming its maximum earlier and it applies to the X_{\max} :

$$X_{\max} \propto \frac{E_0}{A \cdot E_C}. \quad (3.7)$$

This behavior can be confirmed by simulations. Figure 3.2 shows the simulation of the development of a 10^{14} eV shower with proton and iron as primary. The iron primary develops earlier in the atmosphere. Additionally, one can see, that for the heavier nuclei the lateral distribution is wider.

The Gaisser-Hillas function [51] is a parametrization of the longitudinal shower profile with a mean free path length λ , the point of the first interaction X_0 :

$$N(X) = N_{\max} \left(\frac{X - X_0}{X_{\max} - X_0} \right)^{(X_{\max} - X)/\lambda} \exp \left(\frac{X_{\max} - X}{\lambda} \right). \quad (3.8)$$

The lateral distribution at ground level is strongly depending on the energy of the primary particle. The number of particles can be calculated by integrating over the particle density with respect to the distance from the shower core r :

$$N(r) = \int n(r) dr \propto \int S(r) dr. \quad (3.9)$$

For real measurements it is impossible to measure each particle. The detectors are spread over huge areas with discrete distance in between. From these observation points a lateral distribution function (LDF) can be calculated with respect to the distance from the shower core, which leads to a continuous estimation of the particle density, see section 3.3.

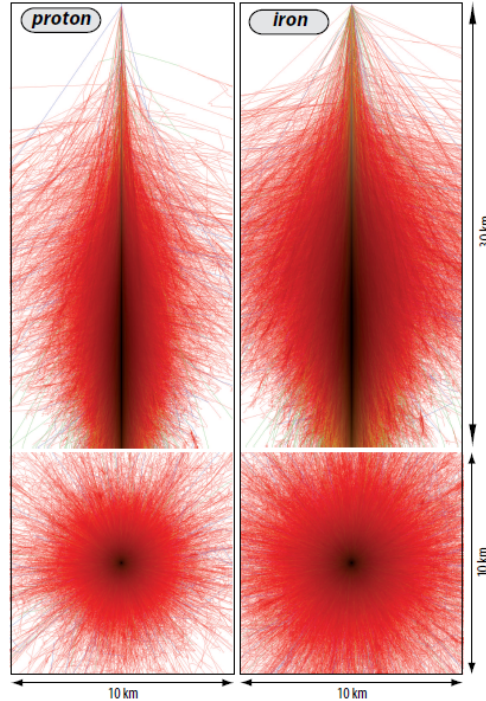


Figure 3.2: Top: Longitudinal shower development of proton and iron induced showers of 10^{14} eV, using CORSIKA [50] simulations, from [6]. The particle type is color coded with red (e^\pm , γ), green (μ^\pm) and blue (hadrons). Bottom: x-y projection of the shower.

3.2 Shower Components

During their propagation through the atmosphere the shower splits up to three components, a hadronic, electromagnetic and muonic component due to the different interaction processes, figure 3.3. Usually the first interaction is a hadronic, since the primary particles are nuclei. This interaction produces further hadrons, mostly pions and kaons. These initiate the other components, while the hadronic component is mainly centered in the so called *shower core* as one can see in figure 3.2.

The electromagnetic component in hadron induced EAS are mainly due to the decay of neutral mesons, mostly pions:

$$\pi^0 \longrightarrow \gamma + \gamma \quad (3.10)$$

$$\pi^0 \longrightarrow \gamma + e^+ + e^-, \quad (3.11)$$

while the first process is with $\sim 99\%$ the dominant one.

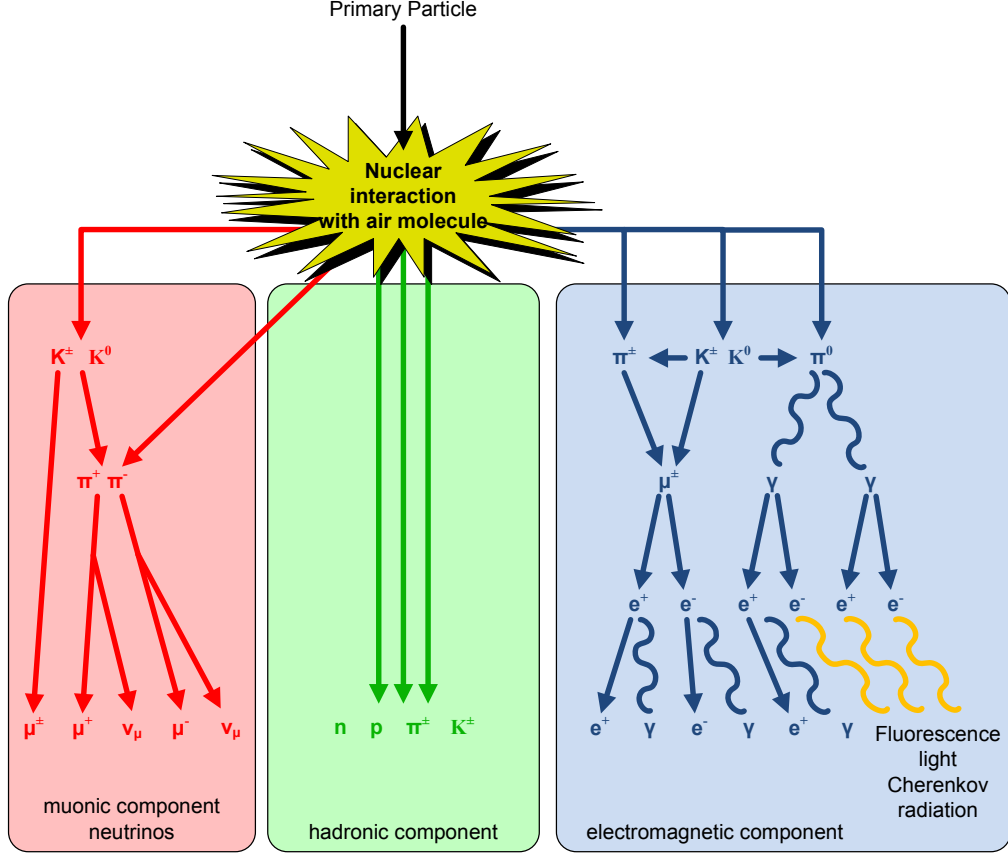


Figure 3.3: Schematic view on the development of EAS. The three main components due to the interactions are indicated. Modified from [6].

High energetic photons or electrons can also initiate the electromagnetic cascade directly by pair production or bremsstrahlung in the electromagnetic field of a nucleus N :

$$e^\pm + N \longrightarrow N + e^\pm + \gamma \quad (3.12)$$

$$\gamma + N \longrightarrow N + e^+ + e^-. \quad (3.13)$$

By pair production the photons can produce additional e^+, e^- pairs. This chain production proceeds until the energy of the single particles reaches the critical energy $E_C \approx 81 \text{ MeV}$. For particles with lower energy $E_i < E_C$ the energy loss is due to ionization. Within one radiation length the electrons get attenuated and the electromagnetic component dies out.

The muonic component is created by the decay of charged mesons, mainly

kaons and pions, of the hadronic component:

$$\pi^\pm \longrightarrow \mu^\pm + \nu_\mu(\bar{\nu}_\mu) \quad (3.14)$$

$$K^\pm \longrightarrow \mu^\pm + \nu_\mu(\bar{\nu}_\mu). \quad (3.15)$$

The created muons have typically an energy of some GeV and a lifetime of ($\tau_\mu \approx 2.2\mu\text{s}$). Due to time dilatation most of them reach the ground. As already mentioned the number of muons is an indicator of the primary particle. The muons are created in the early stage of the shower and are not heavily affected by multiple scattering. Therefore, they contain information which helps to reconstruct the early shower development.

3.3 Observation Methods

Due to the low flux of the high energetic particles the observation of EAS is the only reasonable detection mechanism for energies $E > 10^{14}$ eV. In the last years two different detection methods have been well established, on the one hand the direct detection of secondary particles on ground level with water cherenkov detectors, or scintillators spread over huge areas with distances in the order of km between them, section 3.3.1, and on the other hand measuring the longitudinal shower profile in the atmosphere with fluorescence telescopes, section 3.3.2. Section 3.3.3 will give a short overview of the detection with radio signals, while section 3.3.4 gives an overview of additional detection techniques.

3.3.1 Surface Detectors

The secondary particles of the EAS can be detected with water Cherenkov detectors or plastic scintillators. These detectors are usually placed on a approximately regular grid and provide the measurement of the energy deposit as function of time. Due to the low flux the equipped areas are in the order of up to several 1000 km², with a spacing of the detectors of about 1 km, on the one hand to be able to equip the large areas and on the other hand to collect sufficient signal.

The arrival direction is reconstructed from the relative timing of each detector. As described in the previous section the energy of the primary particle E_{primary} is proportional to the number of particles N_{total} :

$$N_{\text{total}} \propto E_{\text{primary}} \quad (3.16)$$

3.3. OBSERVATION METHODS

With the separated detectors the lateral distribution can only be measured at discrete points. To get a continuous lateral distribution function (LDF) fitting the Nishimura-Kamada-Greisen (NKG) function [52] is a good approach:

$$S(r) = k \left(\frac{r}{r_0} \right)^{-\alpha} \left(1 - \frac{r}{r_0} \right)^{-(\eta-\alpha)}, \quad (3.17)$$

with the Molière radius of the air shower r_0 , a scaling factor k and two independent functions α and η , which need to be empirically determined from data for each experiment. Figure 3.4 shows an example LDF from the Pierre Auger Observatory.

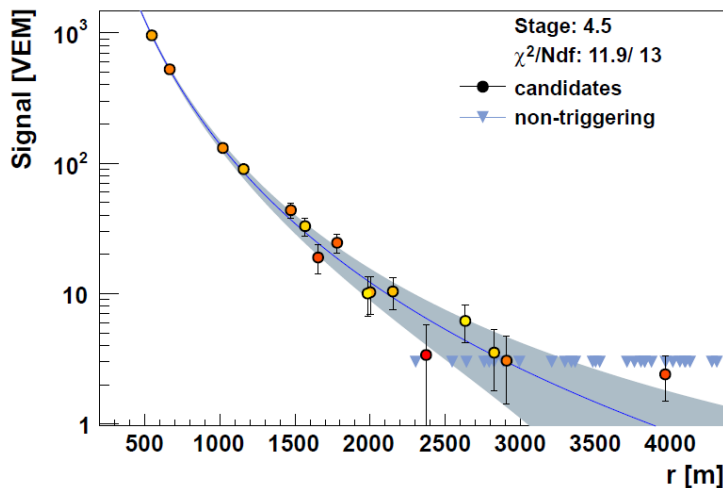


Figure 3.4: Example of a LDF based on measurements of the Pierre-Augur surface detectors. The detector signal is plotted against the distance to the shower axis in units of a Vertical Equivalent Muon (VEM), corresponding to the signal magnitude of an averaged vertical muon. The station timing is color-coded from early (yellow) to late (red), with respect to the signal arrival time. The solid line represents a fit of a lateral distribution function (modified version of equation 3.17), from [7].

The big advantage of particle detection at ground level is the high duty cycle of about 100%. Also the exposure can be easily calculated. The disadvantage is the detection at only one short time slot of the total shower development, which needs a lot of correction effort, based on simulations using hadronic interaction models, to obtain the energy or the particle type of the primary particle.

3.3.2 Fluorescence Detectors

During the propagation of particle showers through the atmosphere, they interact with the surrounding air molecules, which get excited. During the de-excitation they emit photons isotropically, the fluorescence light. It follows that high-energy particles produce a light trace in the atmosphere. The air essentially consists of nitrogen, thus, the nitrogen-transitions are dominant. In Fig. 3.5 one realizes that the greatest emissions of the fluorescence radiation is between 300 and 400 nm. The intensity of the light is proportional

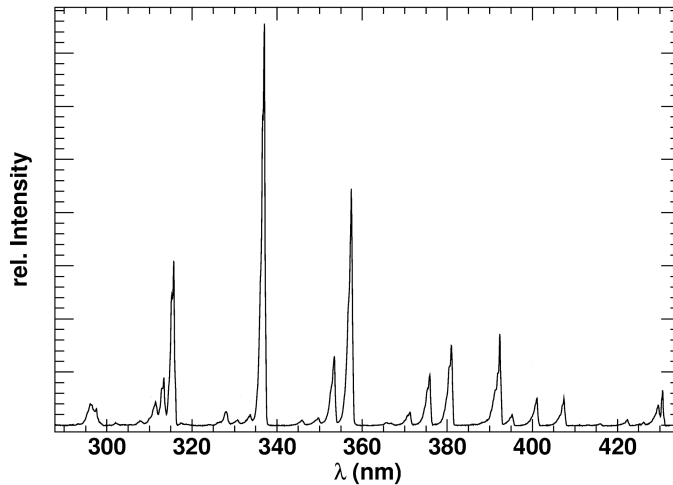


Figure 3.5: Spectrum of the fluorescence light. The relative intensity is drawn against the wavelength, from [53].

to the number of particles in the shower. The fluorescence yield, the number of photons per energy deposit, has been measured in experiments [54], which allows the calculation of the deposited energy in the atmosphere. Due to the relative low fluorescence yield the detection of showers with energies $E < 10^{17}$ eV is difficult. The total deposited electromagnetic shower energy can be calculated by integrating:

$$E_{\text{cal}} = \alpha_{\text{loss}} \int N(X) dX \quad (3.18)$$

$$= \int \frac{dE}{dX} dX. \quad (3.19)$$

with the mean energy loss for relativistic electrons in the atmosphere α_{loss} [55]. The fluorescence light is in contrast to the Cherenkov radiation emitted isotropically. Therefore, it is possible to observe from the side, which enables a detection of the longitudinal shower profile and a very precise direct

measurement of the shower maximum X_{\max} with a resolution of $\Delta X_{\max} = 20 \text{ g/cm}^2$ [56]. This is usually done by fitting the Gaisser-Hillas-Profile, equation 3.8, to the measured trace. But the observation is affected by atmospheric conditions which have to be considered. The observation can only be performed in dark and nearly cloudless nights, which limits the duty cycle to $\sim 15\%$. An example trace measured of the longitudinal shower profile by the Pierre Auger Observatory is given in Fig. 3.6. The air shower with the highest energy so far, $E = 3.2 \cdot 10^{20} \text{ eV}$, measured with a fluorescence detector has been reported by the Fly's Eye experiment [57].

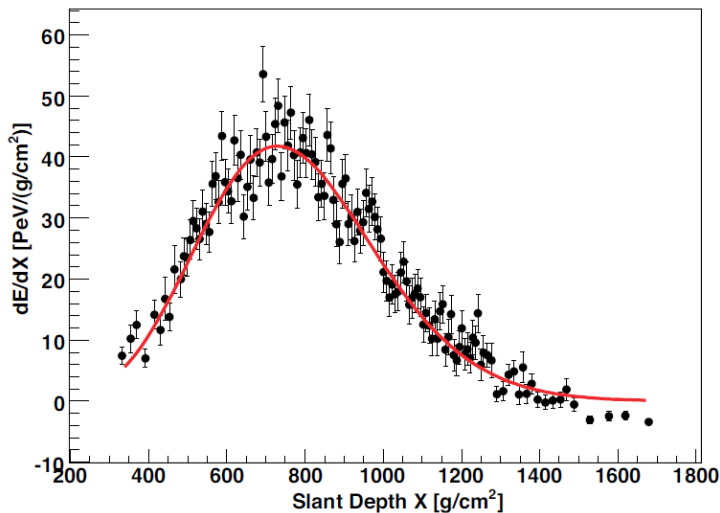


Figure 3.6: Example of a longitudinal shower profile measured by the fluorescence detectors of the Pierre Auger Observatory. The deposited energy is plotted as a function of slant depth. The red line indicates a fit of the Gaisser-Hillas function (Eq. 3.8), from [7].

3.3.3 Radio Detection

The detection of EAS, based on their radio emission in the MHz region, goes back to Askaryan in 1962 [58]. Due to a lack of sufficient hardware the radio detection got lost due to the success in the fluorescence and surface detection. But in the last years, based on the digital antenna arrays, there was a revival of this technique. Experiments like, LOPES [59], CODALEMA [60], AERA [61], LOFAR [62] and Tunka-Rex [63] re-explored the capability of the radio technique in the MHz regime for the detection of cosmic rays with energies $E > 10^{16} \text{ eV}$.

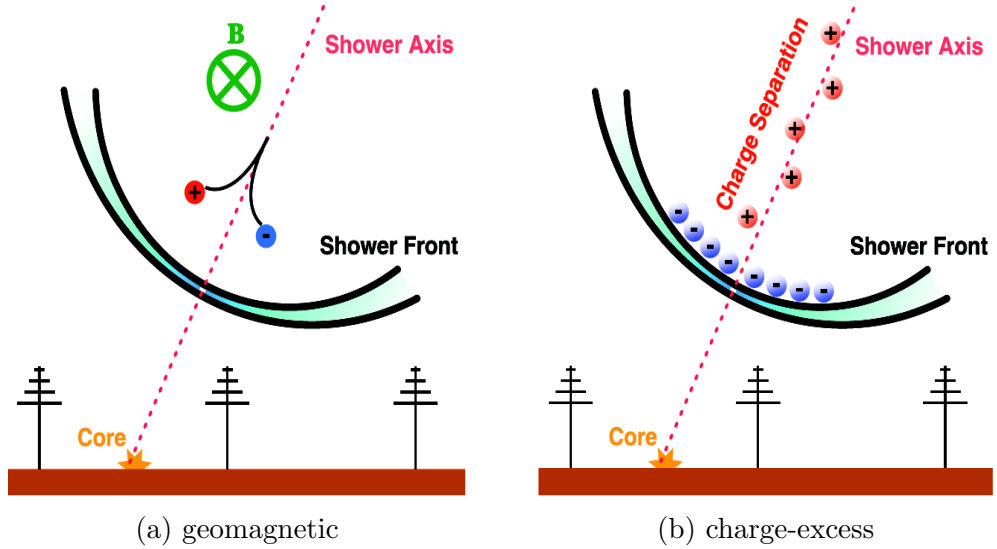


Figure 3.7: Schematic overview of the geomagnetic (a) and charge-excess (b) emission mechanisms, from [66].

The radio emission is a superposition of different effects, on the one hand the geomagnetic emission and on the other hand the emission due to a charge-excess.

The geomagnetic emission results from a charge separation due to the magnetic field of the Earth and the linked Lorentz force:

$$\vec{F}_L = q(\vec{v} \times \vec{B}). \quad (3.20)$$

This leads to a transverse current, which emits dipole radiation. Due to the relativistic speed of the dipole this is strongly beamed forward. Kahn and Lerche proposed firstly this process in 1966 and stated that this could be dominant from 30 MHz to 300 MHz [64,65]. A sketch is given in Fig. 3.7a.

Askaryan proposed in 1962 a radiation due to a superposition of Cherenkov effect and the charge-excess. The particles in the air shower move faster than the speed of light in air, which leads to Cherenkov radiation, with the Cherenkov angle α_{Ch} , which depends on the refraction index n and the relativistic velocity, β . For a typical air shower this leads to $\alpha_{\text{Ch}} \sim 1^\circ$, which corresponds to a ring of enhanced emission with a radius of about 100 m from the shower axis. If positrons and electrons are produced in the shower in the same amount, their signals would cancel out, due to their opposite phase. The annihilation of shower positrons with electrons from air molecules was suggested by Askaryan, which leads to a negative charge-excess. Today we

know, that the dominant part of the charge-excess results from knock-on electrons and Compton recoil electrons. Figure 3.7b shows a schematic view of the emission.

Additionally, strong atmospheric electric fields can produce a similar radiation mechanism as the geomagnetic field, for example during thunderstorm conditions. The perpendicular field component to the shower direction results in a charge separation. Under normal atmospheric conditions this effect can be neglected [67], but it plays a role at high field gradients, where huge amplification of the radio signal can be observed [7]. The particles emit, without a sufficient strong electric field, only synchrotron radiation. An additional electric field aligned parallel to the shower direction leads to an acceleration of one component, while the other gets decelerated, which leads to an asymmetry. If the electric field is perpendicular to the shower direction the electric field force is in the same or opposite direction as the Lorentz force, which leads to an amplification or attenuation of the radio emission. For electric field strength of ~ 100 V/cm the emission of this process is in the same order as the emission of the geomagnetic mechanism. A schematic view is given in Fig. 3.8.

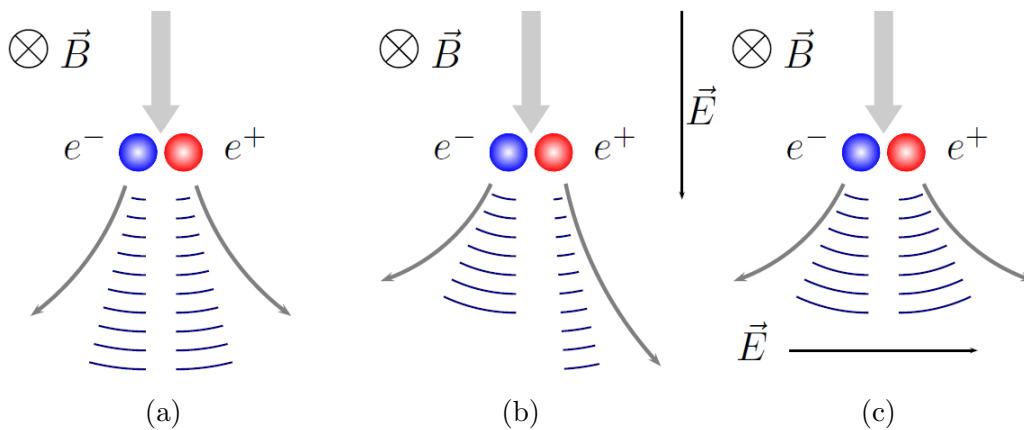


Figure 3.8: Schematic view of the change in the particle trajectory due to additional electric fields and the resulting difference in the radio emission. Standard geometry for no electric field (a), asymmetric trajectories for a parallel electric field (b) and amplified emission for a perpendicular electric field (c), from [68].

The typical thickness of the showerfront, where the main contribution of the radio emission gets generated, is in the order of a few meters. For the

geomagnetic as well as the charge-excess mechanism this leads to a coherent broad-band pulse with frequencies below 100 MHz.

The energy of the primary particle can be obtained by measuring the power of the emitted signal [69, 70]:

$$P_{\text{single}} = \frac{2\gamma^2}{3c^3} \cdot \frac{q^4}{m^2} \cdot \beta_{\perp}^2 \cdot |\vec{B}|^2, \quad (3.21)$$

with charge q , mass m , transverse particle velocity β_{\perp} , Lorentz factor γ and the Earth's magnetic field \vec{B} . By adding the coherence assumption of the whole shower one achieves by setting $q_{\text{shower}} = N \cdot q$ and $m_{\text{shower}} = N \cdot m$:

$$P_{\text{shower}} = \frac{2\gamma^2}{3c^3} \cdot \frac{(Nq)^4}{(Nm)^2} \cdot \beta_{\perp}^2 \cdot |\vec{B}|^2 = N^2 \cdot P_{\text{single}}. \quad (3.22)$$

The emitted signal power scales with the orientation and with the strength of the geomagnetic field, which leads to different detection thresholds for the arrival directions of the primary particle which has to be considered for calorimetric measurements. The radio noise leads to a power limit on the detection of primary particles with at least $\sim 10^{16}$ eV.

3.3.4 Additional Detection Techniques

Measurements by Gorham et al. [71] gave the indication of the possibility to measure the molecular bremsstrahlung radiation in the microwave regime, from collisions of free electrons in the post-shower. The results of different test facilities have been published, for example in [72–74].

Chapter 4

The Pierre-Auger-Observatory

The Pierre Auger Observatory is located in the Pampa Amarilla, in the province Mendoza and north of the town Malargüe and is currently the largest detector for ultra-high energy cosmic rays (UHECR). Fig. 4.1a shows the position in a map of South America, while Fig. 4.1b gives a schematic overview of the array. The basic design as a hybrid detector consists of the Fluorescence Detector (FD) and of the Surface Detector (SD), which are described in more detail in sections 4.1 and 4.2. The aim is to study cosmic rays, via the detection of air showers, at the highest energies $E > 10^{17}$ eV. When both detectors observe the same showers, this delivers the capability of studying systematic effects, as well as an improvement of the shower parameters, as for example arrival direction, energy or composition by the combination of measured data.

In 2004 the data taking was started with the first several hundreds of deployed detectors, while in 2008 the array was completed. Several low energy extensions were deployed, as the SD-Infill, a region with a lower spacing of the SD-Detectors, AMIGA, a muon counter burrowed under the SD-Detector or the HEAT extension of the FD, a standard FD telescope which is tilted by 30° to a higher field of view. Another enhancement is the *Auger Engineering Radio Array* (AERA), an original test facility for the radio detection of cosmic rays, which is today running stable as one detection component. A more detailed description follows in section 4.3.

Today the international collaboration consists of ~ 500 scientists from more than 60 institutions spread around the world.

Section 4.4 will give a short introduction of the Auger software analysis framework, called Offline.

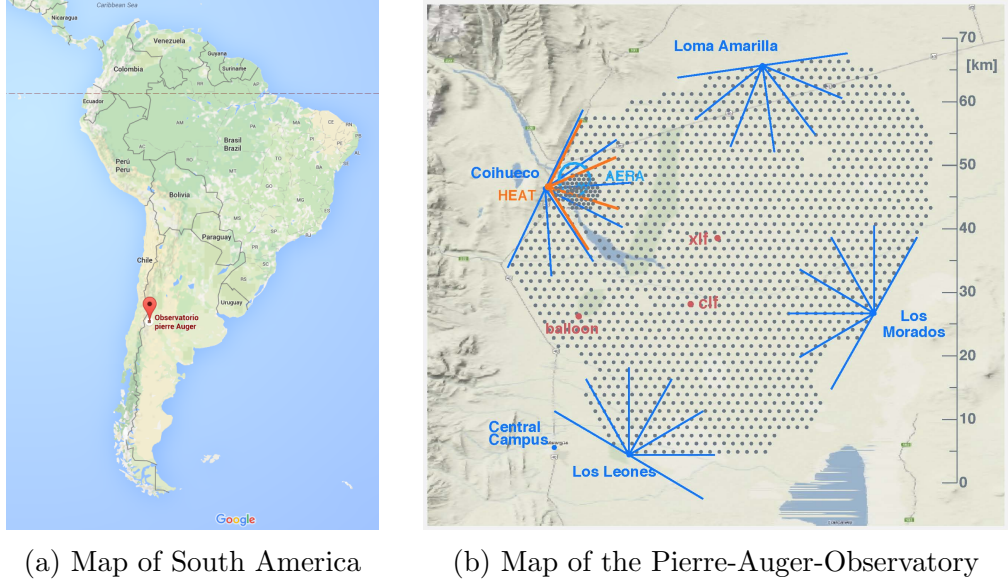


Figure 4.1: (a) shows the location of the Pierre-Augur-Observatory near Malargüe, Mendoza in Argentina, from [75]. (b) gives an overview of the Pierre Augur Observatory. Each dot indicates the position of a water-Cherenkov detector, the fluorescence telescopes and their field of view are represented by the solid blue lines, for the HEAT extension orange lines. Additionally the positions of AERA as well as the atmospheric monitoring facilities Balloon Launching Site BLS (‘balloon’), Central Laser Facility CLF and eXtreme Laser Facility XLF are indicated, from [76].

4.1 Fluorescence Detector

As already described, the frequency range of the fluorescent light is in a wavelength range of 300-400 nm. Thus, the telescopes are optimized for this range. The incoming light is first filtered by a MUG-6-filter which is transparent up to 410 nm in the ultraviolet. The camera is constructed following a Schmidt camera scheme, but with some modifications. To enlarge the field of view, a correction ring is located behind the filter, which directs light, which would pass on the edge of the camera, back on this. A 13 m² large mirror of several segments reflects the incident photons to the camera. The camera is composed of 440 hexagonal photomultiplier tubes (PMTs), which are arranged in a honeycomb structure with 20 x 22 PMTs. The entire camera has a size of approximately 90 x 90 cm, while a PMT has the width of about 4.3 cm. The field of view of a camera is 30° x 30°. The three telescopes of the HEAT extension can be inclined by 30°, which leads to a vertical viewing angle of 30° - 60°. The measured signals are digitized with a sampling rate of

4.1. FLUORESCENCE DETECTOR

10 MHz. A trigger decision is formed afterwards by a hierarchical structure of signal patterns and sent to the Central Data Acquisition System (CDAS), where even single SD detectors, corresponding to the FD event, are read out.

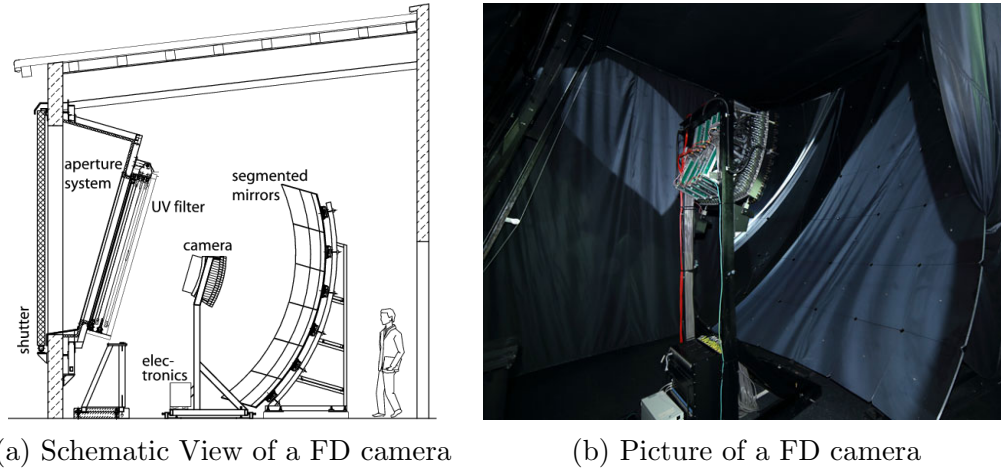


Figure 4.2: Schematic view [77] (a) and a picture [78] (b) of a fluorescence telescope of the Pierre Auger Observatory.

Six of these telescopes are housed in each of the four buildings in a kind of semi-circle. These are located, as can be seen in Figure 4.1b, at the edges of the observatory: Los Leones in the South, Los Morados in the East, Loma Amarilla in the North and in the West Coihueco. The three telescopes of the HEAT extension are located at Coihueco.

Using the pointing direction of the pixels and the time information the shower axis can be determined. In addition the SD data can be used to restrict the geometry. This results in a resolution of the arrival direction below 1° . As described in section 3.3.2 the Gaisser-Hillas function is fitted to describe the longitudinal shower profile, which leads to an accuracy of $\sim 20\%$ in the energy estimation, including systematic uncertainties and a resolution of $\sim 20 \text{ g/cm}^2$ in the position of the shower maximum X_{max} [79].

For energies above $\sim 10^{18}$ eV the detection of the FD gets fully efficient. Due to the limited observation time (dark, cloud less night) the uptime is about only $\sim 15\%$. To ensure high quality data, the atmospheric conditions, especially the aerosols, are monitored during each FD shift with the XLF and CLF laser facilities [80] inside the array. An additional LIDAR system is located at each FD building [81].

4.2 Surface Detector

The Surface Detector (SD) consists of 1660 water-Cherenkov detectors, which cover a area of $\sim 3000 \text{ m}^2$. The stations are deployed in a triangular grid with a spacing of 1.5 km. The full detection efficiency is reached for particles with energies above $3 \times 10^{18} \text{ eV}$.

Each surface detector station consist of a plastic container filled with 12 m^3 ultrapure water in a Tyvek bag. The stations have a radius of about 1.8 m and a height of about 1.2 m. The Cherenkov light emitted from particles in the tank gets measured by three PMTs, which are mounted in the lid of the station. These are read out with a flash analog-to-digital converter running at 40 MHz. The stations are shown in Fig. 4.1b as each point and Fig. 4.3 shows an individual station.

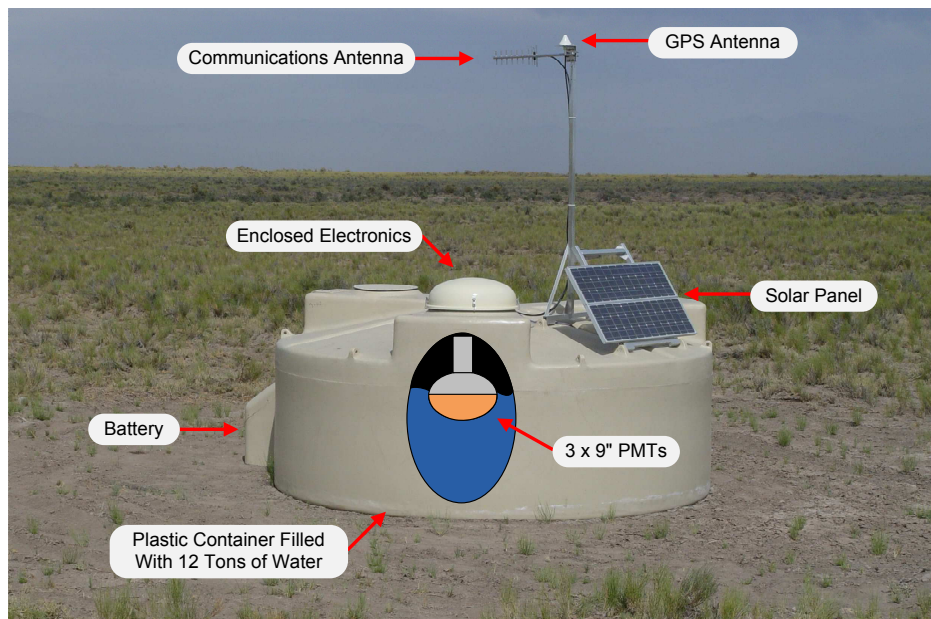


Figure 4.3: Picture of a water-Cherenkov detector deployed in the Argentine Pampas, modified from [76].

The power is supplied by a battery which is charged via a solar panel. Thus, the surface detectors take data around the clock independently. Several trigger algorithm are running on each station and provide a local station trigger. Via radio connection, the data are sent from the stations to the next FD-building. From there, they are forwarded to the CDAS. In the case of a coincidence of at least three stations, the full station data, containing for example the PMT traces, are read out. As for later shower reconstruction

the time information must be very accurate, a GPS clock is used, which time stamps each event with a precision of about 10 ns.

The direction and shower core are calculated by using the arrival time of the signals. The reconstruction accuracy which can be achieved for zenith angles up to 55° is approximately 2° for events measured with 3 stations and below 1° for 6 or more stations [82]. The core position can be obtained within a precision in the order of 50 m. The energy estimation is done by fitting the LDF with a modified NKG-function, which was described in section 3.3.1 and cross calibrated with the fluorescence detector. The signal in each station is then converted to the number of particles in each detector and defined in units of Vertical Equivalent Muons (VEM), which is the average charge signal produced by a penetrating down going vertical muon.

4.3 Auger Engineering Radio Array

The Auger Engineering Radio Array (AERA) was designed as a follow up of LOPES and CODALEMA. It was constructed at the Pierre Auger Observatory and aims to prove the capability of digital radio experiments for large scale applications.

AERA followed the first test set-ups at the Pierre Auger Observatory with antennas located at the BLS and CLF. It is located inside the Infill, a region with SD stations with a lower spacing, in the north-western part of the SD array and in the field of view of the FD telescopes Coihueco and HEAT. The deployment was done in different phases, with different hardware, a map of the antennas and their hardware is shown in Fig. 4.4. In the first phase 24 Logarithmic Periodic Dipole Antennas (LPDA), which are similar to the used antennas at the BLS test set-up, were deployed with a spacing of 150 m. In the second and third phase 100 respectively 25 so-called “Bow-Tie” or “Butterfly” antennas, which has already been used by CODALEMA, were mounted with a spacing of 250 m and 375 m at the second phase and 375 m and 750 m for the third phase. Both antenna types are designed for frequencies between 30 MHz and 80 MHz and the capability of dual polarization measurements is created by the perpendicular combination of two antenna elements. The stations are powered with solar panels and batteries. A photo and drawing of the antennas and the stations is given in Fig. 4.5.

For both station types a low-noise amplifier (LNA) amplifies the signal, which is guided to the electronics box. Within this box additional amplification and

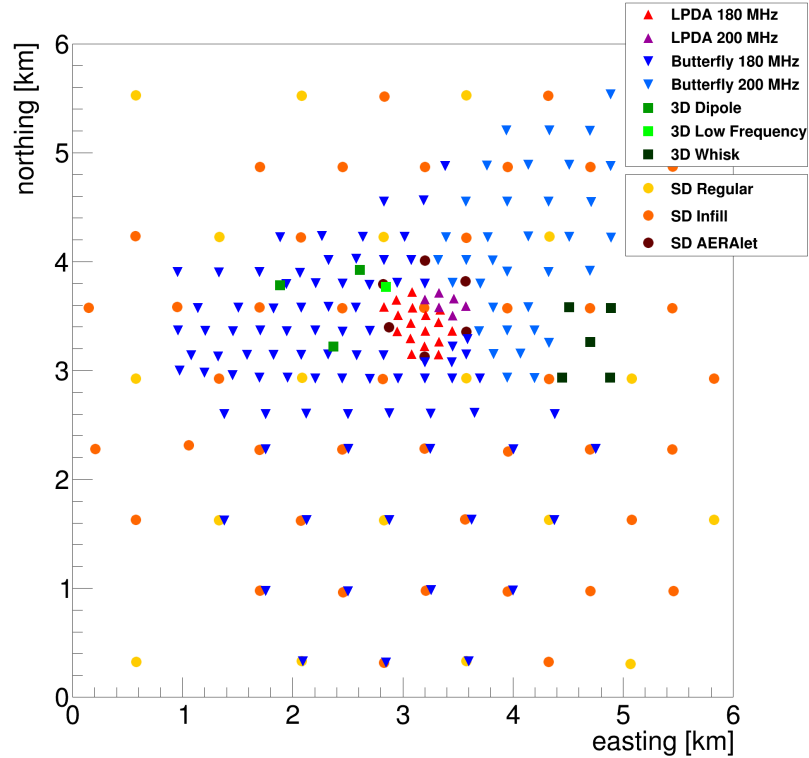


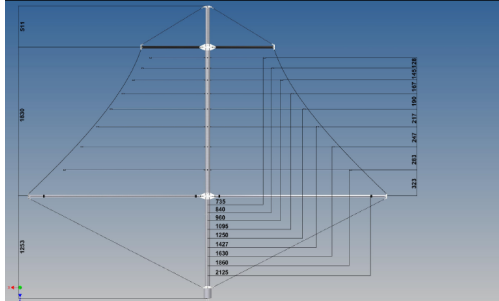
Figure 4.4: Map of the AERA array. The position of the AERA antennas for the different hardware types and SD stations are shown.

filtering are performed. Afterwards the signal is digitized using flash analog-to-digital converters depending on the station type with a sampling rate of 180 MHz and 12 bits depths or 200 MHz and 14 bit depths. A field programmable gate array (FPGA) makes a real-time trigger decision based on pulse shapes. In the electronics the full trace is buffered for two seconds and an event can be read out for a given event time.

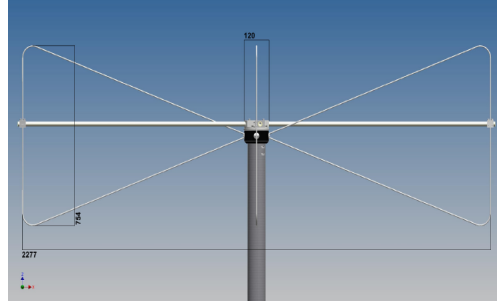
For the reconstruction of the shower a precise timing is needed. The stations are equipped with GPS receivers, which reach an accuracy of $\sim 10\text{--}20\text{ ns}$ [84]. This lasts for a reconstruction, but not for using the beam forming method based on interferometry, which was successfully applied at LOPES [85]. Therefore the timing accuracy can be improved by using the beacon, originally developed at LOPES [86]. This is a signal generator which emits continuous sine waves, that can be filtered in later analysis and enables a timing on nanosecond level [87].

The Central Radio Station (CRS), a shipping container powered by solar panels, contains one part of the DAQ. The other part is located in the Coihueco

4.3. AUGER ENGINEERING RADIO ARRAY



(a) Drawing LPDA



(b) Drawing Butterfly antenna



(c) Station with LPDA



(d) Station with Butterfly antenna

Figure 4.5: Drawing of the antennas from with dimensions in mm (a), (b) and photos of the station with the different antenna types (c), (d). From [7, 83].

FD building. The stations of phase one are connected with optical fibers to the CRS, the later deployed stations use a commercial 5.7 GHz wireless communication system. There are several trigger possibilities, which force a read out of the single stations, for example by an external trigger from the CDAS in case of SD or FD events nearby or self triggered by several algorithms running on the DAQ software.

As discussed in section 3.3.3 electric fields have a influence on the radio emission. In particular, an effect was detected, which amplifies the signals as a result of thunderstorms up to an order of magnitude. For that reason E-field mills have been installed which measure the electric field at ground level every second. These are described in more detail in section 6.1.

4.4 Offline Framework

The Offline software framework is the infrastructure for different computational purposes related to the data analysis [88]. In an open modular structure the collaborators can apply their own structures and algorithms they need for their particular analysis. Offline has the possibility to read different input formats, as real detector data, or data from simulations. The user can make use of own configuration files for the different software parts and many applications provided by the software framework. The main structures are the detector description, the algorithms and finally the event data, as can be seen in Fig. 4.6.

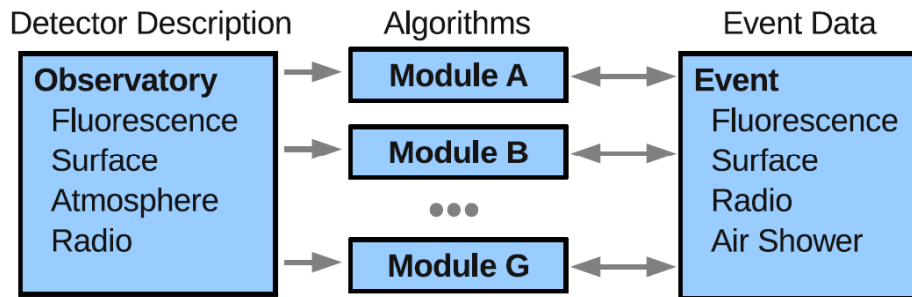


Figure 4.6: Main structure of the Offline software framework, from [89].

The modules are containing the algorithms for the specific purposes. The different modules do not interact directly with each other. They relay data from one to the other by the event structure. This makes it easy to change modules in the analysis chain and use them for analysis of data or simulations. Via XML-cards the input-parameter for each module can be changed. The data of the input-file, as detector traces, as well as information derived during the reconstruction, as the direction and energy of an air shower, are stored in the event class. The modules have access to the data in the event class, and the possibility to add or change parameters.

The configuration of the observatory at the specific measurement time as the detector positions or the atmospheric conditions are stored in the detector class as XML-files or in databases.

The Offline framework provides not only the analysis tools, but also the possibility to visualize the data, the so-called EventBrowser can be used to display the events of the different detectors. For example a view of the SD array and detailed information of the triggered stations, pixel maps and shower properties of FD data or the traces of radio stations.

Chapter 5

Lightnings

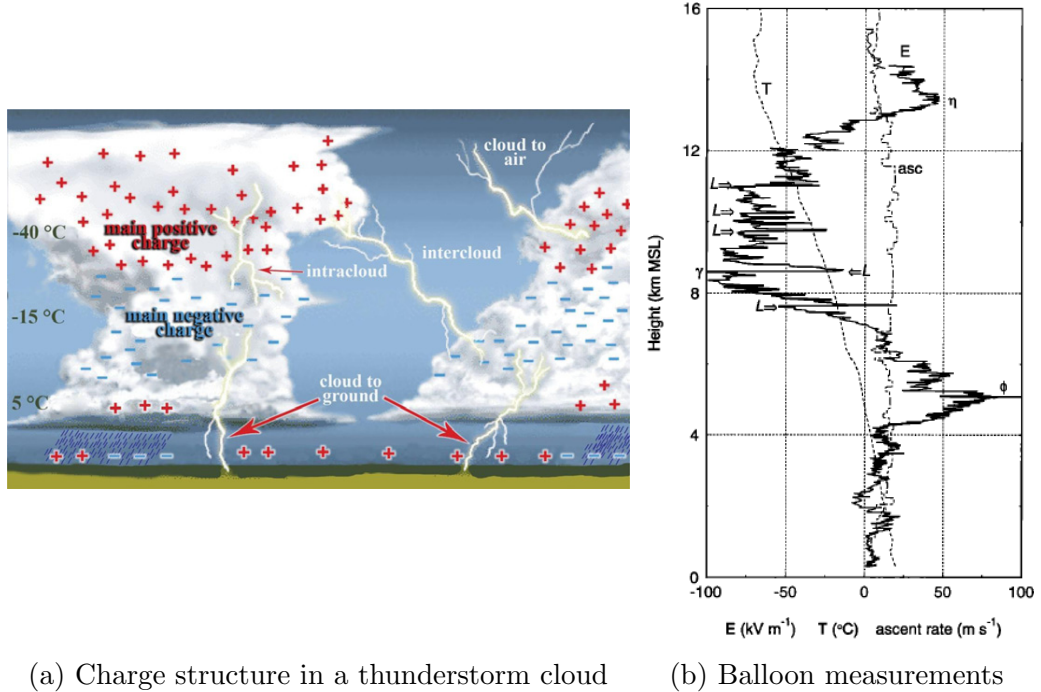
Lightnings are a well known geophysical phenomenon. There are roughly 9 million discharges per year, which results in 6 per km² per year averaged over the Earth. But the physics of lightnings is not well understood up to now [90].

This chapter will give an overview of the lightning theory. Section 5.1 will provide general information on lightnings, how they are generated and an overview on the different lightning types, while in section 5.4 the generation of radio signals will be described, which will be important for the detection of lightnings described in section 6.2. There are additional so-called *Transient Luminous Events* (TLE) which will be mentioned in section 5.5. A mechanism to lower the voltage threshold needed for a charge breakthrough in the atmosphere, connected to cosmic rays, can be found in section 5.3.

5.1 General Information

The beginning of the lightning research can be dated to Benjamin Franklin in 1746, where he began to study electricity in laboratory experiments. In 1750 he reported the similarity of lightnings and the laboratory sparks he created and proposed an experiment to prove that lightning is electricity by flying a kite in a thunderstorm. The modern research on lightning started with Wilson, who used ground-based electric field measurements for the estimation of the charge structure in the thunderstorm clouds and the charge involved in the lightning discharge [91, 92].

An idealized charge structure of thunderclouds is shown in Fig. 5.1a. The primary charge transfer is thought to result from collisions of soft hail (graupel) particles on the one hand, which are so heavy, that they fall or at least



(a) Charge structure in a thunderstorm cloud (b) Balloon measurements

Figure 5.1: (a) shows an idealized charge structure for two isolated simplified thunderclouds. In addition locations where lightnings can occur are indicated. From [90] adapted from [93]. (b) shows balloon measurements of the electrical structure inside a thunderstorm convective region. The electric field (E) as well as temperature (T) and ascent rate (asc) are plotted versus height for the updraft region. Heights of maximal field strength are marked with Greek labels, lightning-related field changes with L , from [94].

stay stationary in the thunderstorm's updraft and small ice crystals which are carried upwards in those updrafts, surrounded by supercooled water droplets. For the production of the primary thundercloud charge this has to take place in an altitude where the temperature is about -20° to -10° . The positively charged ice crystals are carried upwards to the top of thundercloud to an altitude of ~ 10 km, while the negatively charged hail particles remain in the lower part at 6-8 km. This results in a charge separation of typically many tens of Coulomb on both polarities. Another positive charge region can be found below the main negative charge, at altitudes with temperatures slightly above the freezing temperature. The charge structure in a real thunderstorm cloud is actually more complex than shown in Fig. 5.1a and varies from storm to storm and can differ much from the illustrated structure, even up side down. The measurement of the E-field inside thunderstorm clouds is

challenging as was done by Stolzenburg [94]. Figure 5.1b shows the results of a balloon sounding in the updraft region. The data confirm the above mentioned charge distribution.

Typical thunderstorms last for 40-60 min and produce lightning flashes every 20-30 s, covering an area of 100-300 km² while the size of the cloud is roughly a circle with a diameter of 6 to 10 km.

Lightning strikes can be divided into two categories:

- those that bridge the gap between cloud and ground,
- those that do not, so called *cloud discharges*.

The cloud discharges which occur totally within a single cloud are called *intracloud lightning* (IC), the ones which take place between the cloud and the surrounding charge regions are called *cloud-to-air lightning*.

The cloud to ground (CG) lightnings can be divided into four types, which are illustrated in Fig. 5.2. They are distinguished from each other by the sign of the charge and the propagation direction of the initial charge leader. Figures 5.2a and 5.2c refer to the downward lightning. 90% of cloud to ground lightnings are initiated by a negative charged and down-going initial leader, and 10% by a positive charged down-going initial leader. The upward lightning, figures 5.2b and 5.2d, are relatively uncommon and are initiated by the top of mountains or high man made buildings towards the cloud charge region.

The development of a negative cloud-to-ground lightning with respect to the time is shown in Fig. 5.3. Usually, they begin with a first discharge between the bottom of the main negative charge region and the positive region below. During this discharge free electrons are provided, previously attached to hail or other particles, which are due to their low mass extremely mobile and build the primary contributor of the lightning current. These free electrons over run the small positive charged region, neutralize a significant amount of the positive charge and propagate to the ground. The negative charge moves from cloud to ground in discrete luminous steps with a length of tens of meters within a microsecond or less and a pause in between the steps of about 50 μ s far above the ground and 10 μ s near the ground. This physical mechanism is called *stepped leader*. The averaged speed of the stepped leader is $\sim 2 \times 10^5$ m/s which leads to a duration of 20 ms for the propagation from the cloud to ground. Typically the total stepped leader has a charge of 5 C over its length, which leads to a current of at least 100-200 Amperes during

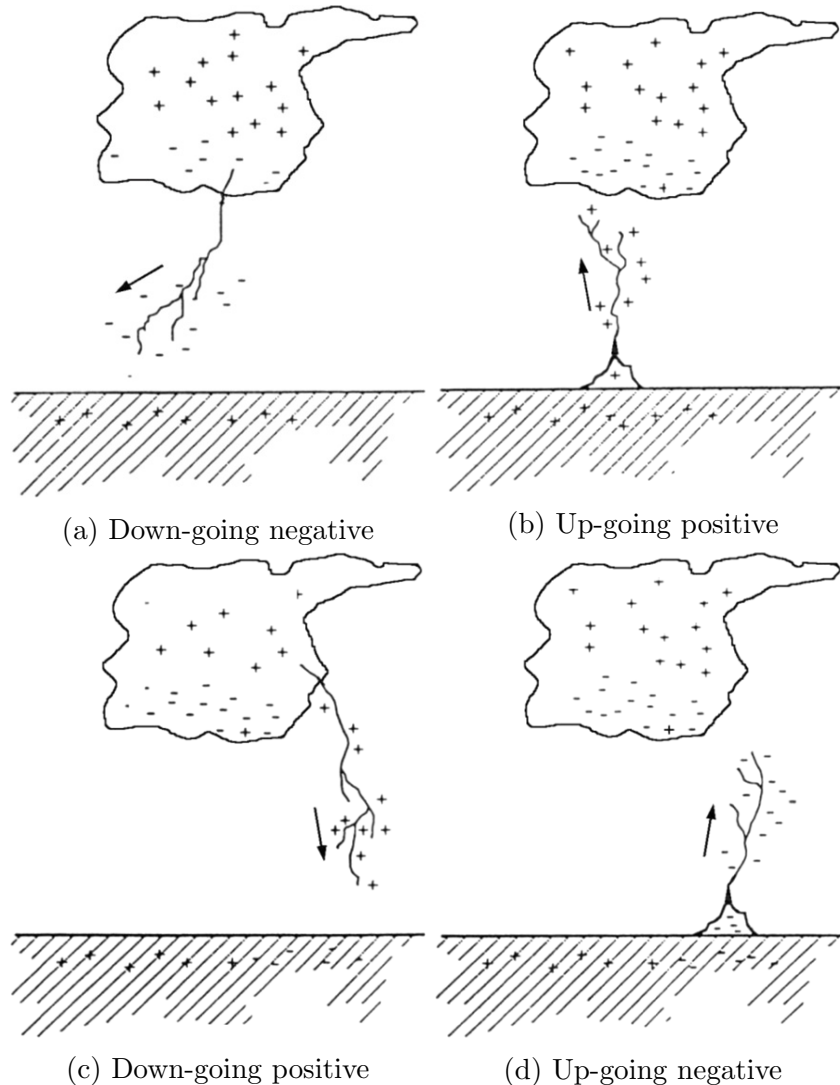


Figure 5.2: Sketch of the four cloud-to-ground lightning types, defined from the directional propagation and charge of the initiating leader. Modified from [95] according to [96].

this process. Each step has a peak current in the order 1000 A and generates a pulse of visible light, radio-frequency energy and X-rays.

The large negative charge induces a positive charge on the conducting Earth's surface beneath it and especially objects on the surface. When the electric field of this charge gets large enough, an upward-going discharge carrying positive charge will be initiated, Fig. 5.3 at 20.00 ms. This upward moving discharge contacts a branch of the downward going leader and the negative

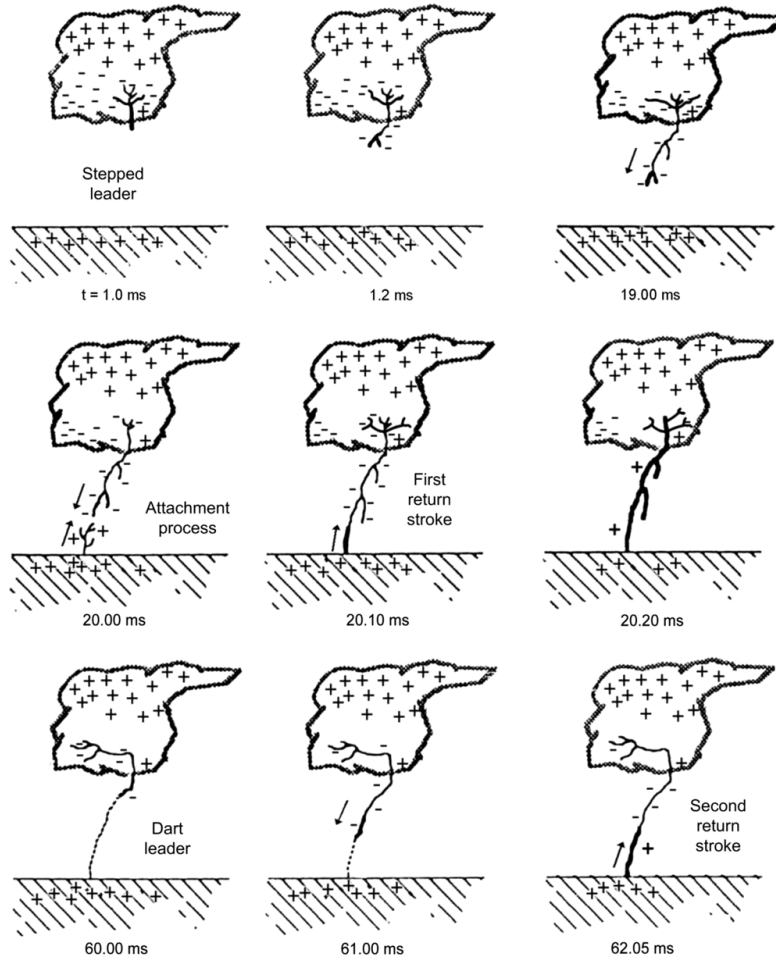


Figure 5.3: Drawing of the development of a negative cloud to ground lightning, adapted from [95].

charge near the bottom moves violently into the earth. This causes large currents through the previous current path, the so called *channel*, which gets highly luminous and conducting. The process of the first upward going charge is called *first return stroke*, figure 5.3 at 20.10 ms and 20.20 ms. Even if the return stroke moves upward, the free electrons, representing the primary current, always move downwards. The return stroke generates the high temperatures in the atmosphere, about $30\,000^{\circ}\text{C}$, we commonly observe. The human eye is not fast enough to see the dimmer downgoing stepped leader. The expansion due to the heating of the air generates the thunder, we hear. 80% of the lightnings contain more than one stroke, typically four to five. These are separated by 40-50 ms. Subsequent strokes are only generated if within ~ 100 ms enough charge is made available in the region of the previ-

ous stepped leader. A so-called *dark leader* moves down the defunct channel, creating negative charged regions, Fig. 5.3 at 60.00 ms and 61.00 ms. The dark leader induce a second return stroke. This process can take place more times. The subsequent strikes lead to half or less of the current flow of the first return stroke, but the risetimes are much faster, $\sim 0.1 \mu\text{s}$ in comparison to a few milliseconds.

Typically about 30 C are transfered from the main negative part of the thunderstorm cloud to the earth.

For downgoing positive stepped leaders the steps can not be distinguished optically as for the negative stepped leader, if there are steps et all. With 30 kV the median peak values of positive and negative stepped leaders are similar, but the maximum peaks of the positive one can reach up to 300 kA, while the negative ones rarely exceed 100 kA. The positive discharges usually generate only one return strike, which leads to a relative long period of charge transfer. Overall the total charge transfered can exceed that for negative strikes.

5.2 Detection Techniques

The lightning detection is based basically on two types of systems. On the one hand optical observation from space, as the Optical Transient Detector (OTD) [97] or the Lightning Imaging Sensor (LIS) [98] and on the other hand the detection of the radio noise generated by the lightning in the VLF/LF band with multiple antennas and a time of arrival reconstruction, as National Lightning Detection Network (NLDP) [99], the European lightning location system (EUCLID) [100] or the World Wide Lightning Location Network (WWLLN) [101] which is described in section 8.3 in more detail.

5.3 Relativistic Runaway Electron Avalanche

The threshold for a conventional breakdown is $E_{th} \approx 2 \text{ MV/m}$. As can be seen in figures 5.1b and 5.4 the measured field strengths are about one order of magnitude smaller. Thus a mechanism is needed which describes the lower threshold needed for the lightning initiation. Gurevich introduced a process taking relativistic seed electrons from EAS into account, which get accelerated in the electric field and generate secondary particles. This leads to an electron avalanche, which lowers the needed threshold to the observed ones [102, 103].

5.3. RELATIVISTIC RUNAWAY ELECTRON AVALANCHE

The loss due to ionization determines the braking force F of an energetic particle [104]. The Rutherford cross section σ of the Coulomb scattering is proportional $1/\epsilon^2$, with ϵ the mean energy of the particle. Therefore, the braking force is, within the non relativistic regime, proportional to the molecular density N_m and inverse proportional to the electron energy:

$$F \propto \epsilon \sigma N_m \propto 1/\epsilon. \quad (5.1)$$

The cross section decreases with the electron energy to a minimum at 1.5 MeV. This leads to the minimum braking force F_{\min} which then grows slowly increasing logarithmically.

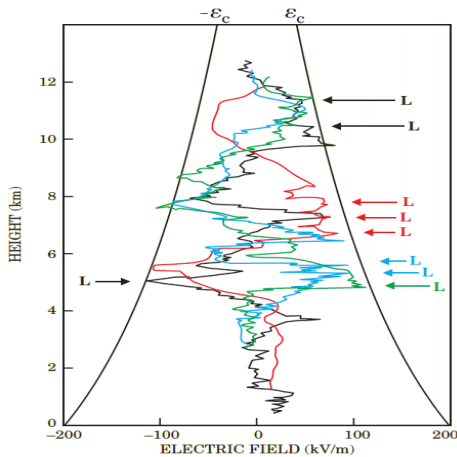


Figure 5.4: Electric field in a thundercloud as a function of the altitude. The calculated runaway breakdown critical field is indicated by the curved black lines. Modified from [103].

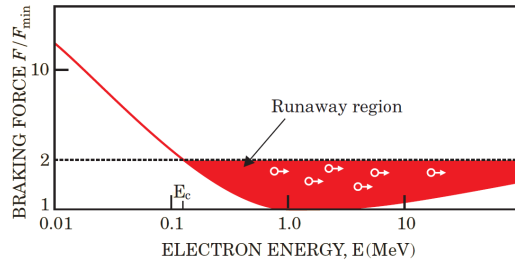


Figure 5.5: Braking force F acting on an electron transversing matter as a function of electron energy E . Inside the red shaded area runaway breakdown can occur. Modified from [103].

The reduced scattering friction leads to the possibility of accelerated electrons within the thunderclouds. An electric field E that exceeds the critical field E_c , with

$$E_c = F_{\min}/e, \quad (5.2)$$

leads to a continuous acceleration of electrons with a sufficient high energy

$$\epsilon > \epsilon_c \approx mc^2 E_c / 2E. \quad (5.3)$$

This region is indicated in Fig. 5.5 with the red shaded area. These electrons were firstly predicted by Wilson 1924 [105] and later called *runaway electrons*. The majority of electrons from the ionization of neutral molecules have low energies, but some will have rather high energy $\epsilon > \epsilon_c$. These electrons will be accelerated in the field, either, and generate new electrons with $\epsilon > \epsilon_c$, which leads to an exponential growing runaway avalanche. The large number of generated slow electrons lead to an electrical breakdown of matter.

Taking the threshold for the classical breakdown of 2 MV/m into account, the critical energy is for the same conditions only 200 keV. This results in a runaway breakdown at electric fields one order smaller than needed conventionally.

Beside the condition $E > E_c$ seed electrons with energies above the critical energy of 0.1-1 MeV are needed. These are in the atmosphere electrons produced as secondary particles of EAS. As the velocity of the particles is close to the speed of light, the dispersion along the axis of the EAS is very small. As mentioned in chapter 3 the number of secondary particles n_s within an EAS is proportional the energy of the primary particle ϵ_p , for example $\epsilon_p = 10^{15}$ eV, $n_s = 10^6$ or $\epsilon_p = 10^{19}$ eV, $n_s = 10^{10}$. The rate of lightnings and the flux of cosmic rays can be compared to derive the needed energy threshold of $10^{16} - 10^{17}$ eV for the primary particles.

The average energy of the secondary EAS electrons is about 30 MeV. If these electrons propagate through a thundercloud's electric field close to the critical value E_c , the number of secondary electrons with $\epsilon > \epsilon_c$ grows exponentially and leads together with the low energetic electrons to an EAS induced runaway breakdown discharge.

Fig. 5.4 shows the measured electric field in thunderclouds as a function of the altitude, and in addition the corresponding critical energy. The critical energy decreases with the altitude because of the air density. The observed lightnings, indicated with the letter L at the side, occur within the critical field envelope, when the field is nearly equal to E_c . [103]

5.4 Radio Emission

Lightning strikes can be detected by their emitted signal in the low-frequency (LF) region, as well as in the very high frequency (VHF) region. CG flashes mainly radiate in the LF or very low frequency (VLF) band. As the typical wavelength of the emission is related to the length of the radiating element, this leads to long wavelength for large charge carried over the length up to

kilometers. Cloud lightnings produce a lower current of about 1 kA, over the length of kilometers, which makes them detectable in the LF, too, but with typically one order of magnitude lower amplitudes. The detection in the LF region enables only to detect the position of the highest current derivative di/dt , which is usually the point just above the ground of the return strike for CG lightnings. Due to the conductivity of the ground the signals are predominantly vertical.

The stepped leaders have a much smaller dimension in the order of tens of meter and carry less current, which results in a lower signal in the VHF region. As the size of the single steps is rather small, a large number of them are generated in CG flashes and each one can be detected, which leads to the possibility of creating a map of the development of a lightning with respect to the time and the position of the discharges [106]. The frequency spectrum of the emitted signal of a lightning is given in Fig. 5.6.

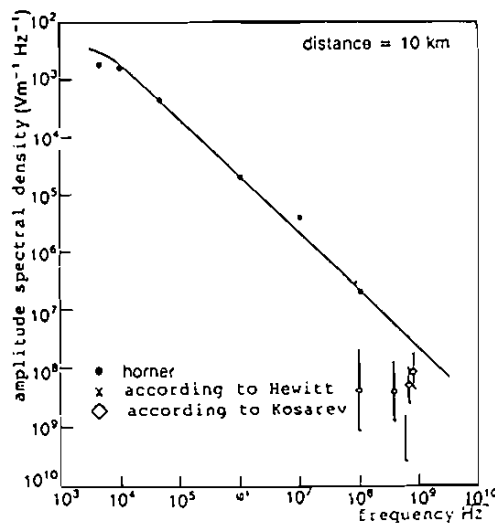


Figure 5.6: Amplitudes of the radiated signal of a lightning at 10 km distance, from [107], referring to [108–110].

5.5 Transient Luminous Events

Transient luminous events (TLE) are optical emissions above thunderclouds in the stratosphere, mesosphere, and lower ionosphere. They are generated by discharges or in response to CG or IC lightnings. TLEs have been reported for at least 100 years, but their existence was not established until 1990 by

Franz et. al. [111], who accidental recorded a Sprite during tests of a low-light video camera. Figure 5.7 sketches the different types of TLEs, which will be shortly described in the following and their corresponding height in the upper atmosphere.

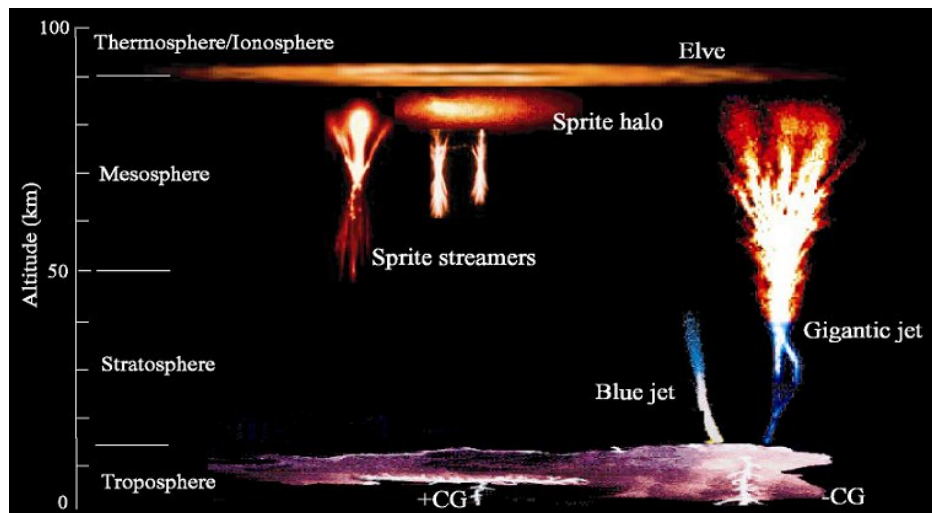


Figure 5.7: Sketch of TLE types and their height in the atmosphere, from [112].

- **Sprites and Halos:**

Sprites last for up to few tens of ms and are visible to dark adapted eyes [113]. There are about 1000 Sprites per day world-wide [114]. Halos are a glow below the ionosphere, produced by ionization waves and have a diameter less than 100 km. Sometimes Halos go ahead or go along with Sprites.

In the current models, based on a proposal of Wilson in 1924 [105], Sprites are conventional discharges, involving downward propagating streamers, accompanied sometimes by diffuse negative upward going discharge. Mostly they are generated in response to large positive CG lightnings. Above the thundercloud the atmosphere is highly conducting and the charge movement of the lightning initiates a rapid dipole-moment change in the mesosphere. This leads to an electric field in the upper atmosphere, which is generated faster than the Maxwell relaxation time, extended up to the ionosphere. The field strength is falling with the cube of the altitude above the thundercloud. The conventional

breakdown field scales linear to the exponential decrease with altitude of the air density. Sufficient large lightning flashes can produce a field which exceeds the conventional breakdown field typically in a height of about 70 km and initiates positive streamers, which grow and branch, forming a Sprite.

The charge moment change of positive CG flashes can exceed the ones of negative CG flashes. For that reason the Sprites are generally initiated by the positive CG lightnings.

- **Elves:**

Emission of Light and Very Low Frequency perturbations due to Electromagnetic Pulse Sources (ELVES) were discovered one year after Sprites [115]. They are rapidly expanding rings of light emission in the lower ionosphere. Elves are generated by electromagnetic pulses (EMP) of lightning return strikes. These propagate as spherical waves up from the lightning channel and intersect the ionosphere as a ring, which expands outward faster than the speed of light. The EMPs electric field leads to a heating of the free electrons, which enhances the collisions inducing excitations and the optical light emission [116]. The number of Elves is 9 times the number of sprites [117], which makes them the most common TLE. Elves can be detected with the Fluorescence Detector of the Pierre Auger Observatory, which will be mentioned in section 10.3.

- **Blue Jets and Gigantic Jets:**

Blue Jets are a kind of upward lightning, which exits the top of the thundercloud and reaches the upper atmosphere at approximately 25 to 40 km [118–121]. They last for about 300 s and are also bright enough to be seen by dark adapted eyes. Gigantic jets are some kind of analogy of CG lightnings, not propagating to ground, but to the conductive ionosphere at about 90 km [122–126].

Blue Jets are modeled to begin as an electrical breakdown between the upper charge regions in a thunderstorm cloud, shortly after a charge imbalance due to a lightning discharge. This results in an upward propagating lightning, which extends to the stratosphere. Gigantic jets are modeled as an upward analogy to a negative bolt from the blue [127].

CHAPTER 5. LIGHTNINGS

Chapter 6

Lightning Detection Devices

At the Pierre Auger Observatory different lightning detection systems are available, namely E-field mill, lightning detection system and the SD lightning flag. In this section the detection mechanisms of these systems are described. It is also shown how the data are provided in the Auger Monitoring System.

6.1 E-Field Mill

E-field mills measure the E-field at ground level. Two Campbell Scientific CS110¹ E-field mills are installed inside the Pierre Auger Observatory and can be seen in Fig. 6.1. One is located at the Central Radio Station (CRS). The other one was located at the Balloon Launching Site (BLS) until it was dismantled in March 2013 and then redeployed inside the AERA field in August 2014, the positions are indicated in Fig. 6.2.

The sampling rate of the E-field mills is 1 Hz.

6.1.1 Detection Mechanism

The CS110 works with a shutter mechanism. Behind the shutter a measuring plate is mounted. This gets charged by the electric field, if the shutter is opened and discharged if the shutter is closed. The amplitude of this signal is proportional to the electric field.

Lightnings and especially lightning clouds have a large influence on the electric field on ground. Under fair weather conditions the E-field is lower than ~ 50 V/m. Under thunderstorm condition the E-field can reach values larger

¹<http://www.campbellsci.com/cs110-sensor>



Figure 6.1: Mounted CS110 E-field mill in Karlsruhe

than 10000 V/m. If a cloud moves over the field mill, the electric field changes slowly in the order of minutes. If there is a lightning fast jumps appear in the electric field due to the discharging in the atmosphere which is drafted in figure 6.3. This is used for the lightning analysis of the E-field data for the Pierre Auger Observatory, which was adapted from LOPES in Karlsruhe. They used the same field mill to set their DAQ into a lightning mode [128]. The analysis differentiates between thunderstorm condition and lightning discharges. For both the absolute value of the measured E-field at one second E_i needs to be larger than the threshold of 500 V/m.

If the change in the slope of the E-field data seconds before and after E_i is larger than 40° the point is marked as thunderstorm indication point.

If there is a jump which is larger than two times the RMS of the E-field data in the minute before and at least 300 V/m, then the point is also marked as lightning indication point.

$$\Delta_{E\text{-field}} = |E_i - E_{i-1}| \quad (6.1)$$

$$TS = (\Delta_{E\text{-field}} > 2 \cdot \text{RMS}_{1\text{min}}) \text{ AND } (\Delta_{E\text{-field}} > 300 \text{ V/m}) \quad (6.2)$$

If there is sudden discharge $\Delta_{E\text{-field}} > 15 \cdot \text{RMS}_{1\text{min}}$ this point is marked as lightning discharge.

10 minutes before and after an identified lightning indication point or lightning discharge are marked as thunderstorm condition (ISTS) [128].

A typical trace of the E-field mills on thunderstorm conditions is shown in Fig. 6.4.

6.1. E-FIELD MILL

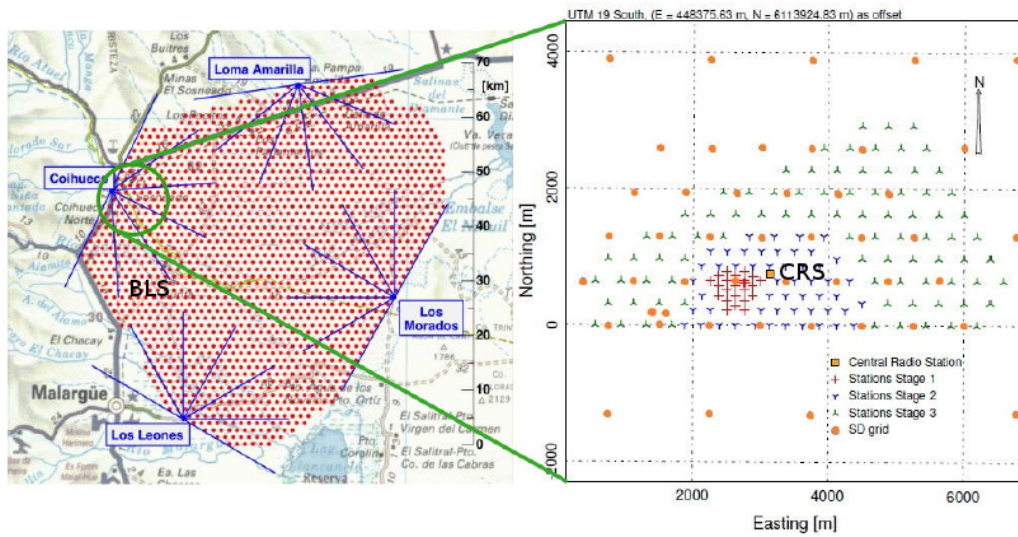


Figure 6.2: Pierre Auger Observatory Map. The location of the BLS and CRS are marked. From [76].

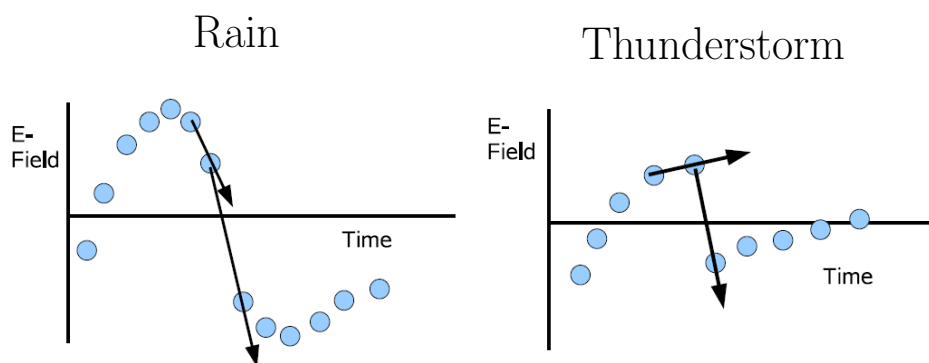


Figure 6.3: Sketch of E-field discharge. Left: Slowly discharge due to rain. Right: Sudden discharge due to lightning. From [128].

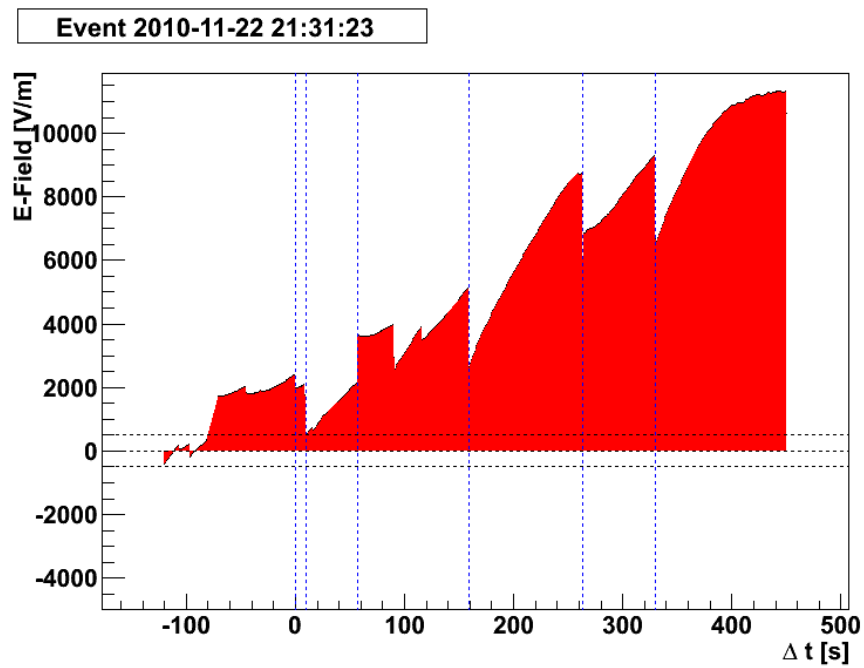


Figure 6.4: Example of the measured E-field under thunderstorm conditions. The E-field in V/m is plotted against the time in seconds on the x-axis. $\Delta t = 0$ refers to 2010-11-22 21:31:23, which is the thunderstorm event. The horizontal dashed lines indicate the threshold of 500 V/m and the vertical lines mark the lightning events found by the thunderstorm algorithm.

6.2 Lightning Detection System

After discussing E-field mills the following paragraph now treats a different method for lightning detection. The StormTracker from Boltek² is a lightning detection device which consist of a PCI card and an external antenna which is connected via a Cat5 patch cable. Fig. 6.5 shows a picture of the PCI card and the antenna. This device is able to detect lightnings within a radius of up to 1000km and more. It detects radio signals in the kHz-region ($\sim 10 - 90$ kHz) which are initiated by lightnings. Five Lightning Detection Stations (LDS) based on the Boltek StormTracker are deployed at the Pierre Auger Observatory. One at the campus in Malargüe (MG), and the other ones at each of the FD-buildings in Los Leones (LL), Los Morados (LM), Coihueco (CO) and Loma Amarilla (LA), which are marked in Fig. 6.6. The antenna has two polarizations, North-South (NS) and East-West (EW). An estimation of the direction of the lightning is done by each single detector via the fraction of the signal amplitude in both directions. By taking the amplitude into account the distance is estimated, but lightnings which generate a weaker signal get detected too far away, the ones with higher amplitude get detected too close. Therefore an averaged distance is calculated by taking older lightnings from the same direction into account to minimize event to event fluctuations. Traces with a higher frequency than 90 kHz are rejected as high frequent noise.

6.2.1 Data Acquisition

Each StormTracker PCI card is plugged into a small PC with low power consumption (Intel D2700MUD³). The StormTracker PCI Card has the advantage, that it is possible to read out the traces and not only reconstructed values for a detected lightning. The read out of the module is done using a program developed within this thesis, based on the standard application of the Boltek Linux software development kit⁴. The detector returns values based on a single detector reconstruction. The PC-time of the detected event, the direction, the distance to the lightning and an averaged distance which is calculated with respect to former events from the same direction. These values are directly written into the Auger Monitoring MySQL Database and in addition the data are stored with the traces of the raw events as root files on the local hard disk. An example trace is shown in Fig. 6.7.

²<http://www.boltek.com/product/stormpci-long-range-detection-kit>

³<http://www.intel.de/content/www/de/de/motherboards/desktop-motherboards/desktop-board-d2700mud.html>

⁴not longer available at <http://www.boltek.com>



Figure 6.5: Boltek StormTracker PCI Card with antenna. From [129].

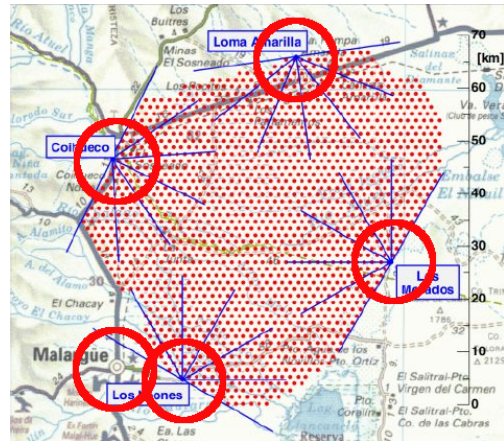


Figure 6.6: Map of the Pierre Auger Observatory. The sites of the lightning detectors are marked with red circles. Modified from [76].

6.2.2 Sampling Rate Measurement

For the StormTracker no manual with technical information is available. To obtain the sampling rate of the raw detector traces a function generator was used. A 13m long cable was plugged into the function generator, wound around the StormTracker antenna and used as antenna. The signal, a sine wave with a known frequency, was measured and a sine was fitted to the measured signal trace. From the fitted frequency measured in bins and the known frequency of the original signal the time per bin was calculated. The result of 594 measurements was filled into a histogram and a Gaussian fitted to this, which is shown in figure 6.8. This results in 125 ns per time bin, corresponding to a sampling frequency of 8 MHz.

6.2. LIGHTNING DETECTION SYSTEM

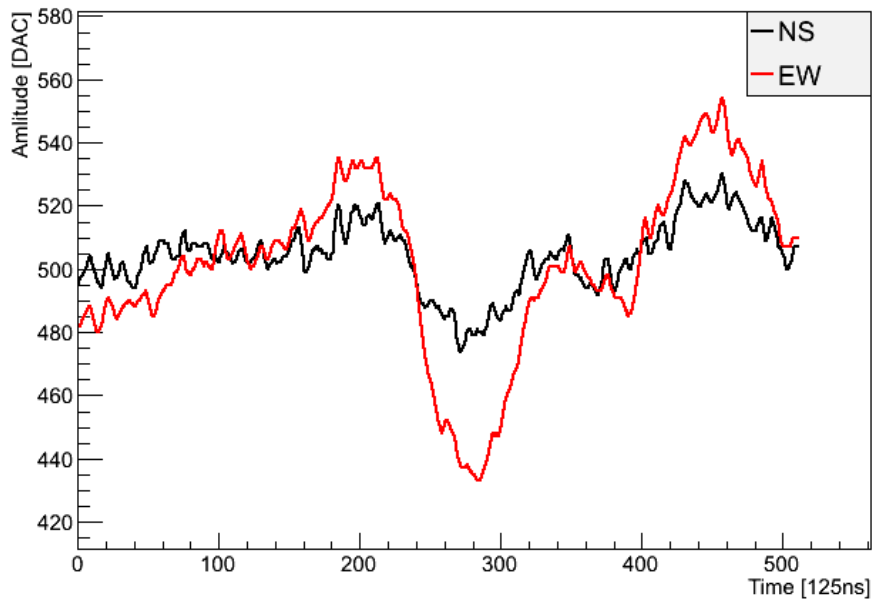
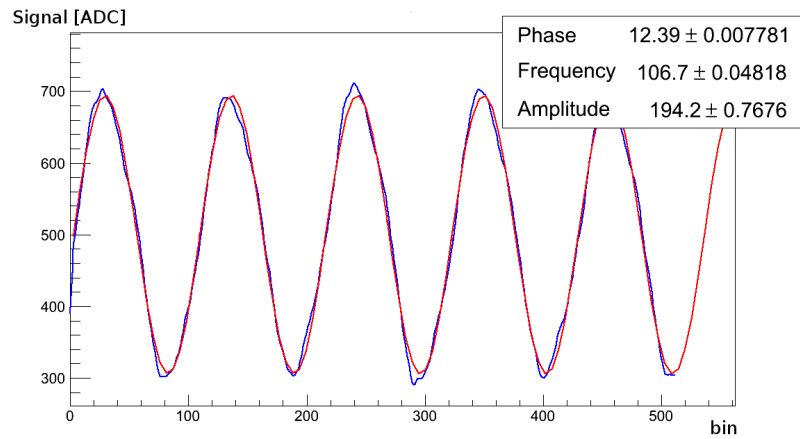
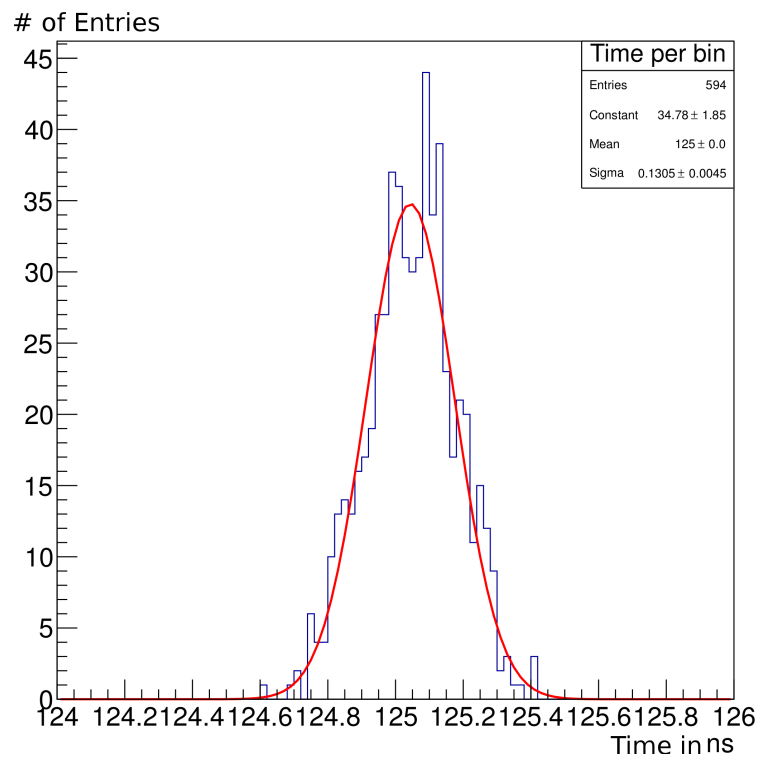


Figure 6.7: Example trace of a Boltek Lightning Detector. Amplitude of the the north-south (black) and the east-west polarization (red) plotted against the time in bins per 125 ns, compare section 6.2.2.



(a) Trace of the StormTracker (blue) and sine fit (red)



(b) Histogram of the measured time per bin

Figure 6.8: Result of the measurement of the sampling frequency

6.2.3 Timing

Since the Boltek StormTracker itself has no timing module different methods are investigated in the following. The accuracy of time coincident events of the local PC-time using a ntp-server and a ptp-server as well as an external GPS-Timing Module, which is described in section 6.2.4, is compared.

First tries to get a good timing accuracy were done by using the local Auger Network Time Protocol (NTP) server. But the time deviation between coincident lightnings measured in the single detectors shows a large uncertainty, which can be seen in Fig. 6.9.

To get a better relative timing of the detectors to each other the Precision Time Protocol daemon⁵ (ptpd) was used. The Malargüe PC was chosen as ptpd-server. On the other PCs the daemon sent a message to the server and wait for the answer, containing the server time. By calculating the runtime of the message this can increase the timing accuracy up to milliseconds [130], depending on the network quality. The daemon assumes, that the runtime for the message to and from the server is the same, which must not be the case and calculates a delay by building the mean of the measured delays. This results in an deviation of the arrival time for the stations MG and LL between -200 and 600 μ s for an example data period in Fig. 6.10, taking the distance between both detectors into account, the deviation should be in the region of 30 ns. Using this method has shown, that after times with a lot of network communication the delay grows, which results in a larger uncertainty. After network problems the calculated delay remained large, even if the problem is solved and the real delay is small, which results in a systematic error because of the over estimation of the network delay. This could only be solved by restarting the ptpd. Another disadvantage of ptpd is, that only a relative timing is possible which results in an uncertainty of the absolute timing for the lightnings. For this reason in the course of this thesis a GPS-extension is developed since it allows the best temporal accuracy.

⁵<http://sourceforge.net/projects/ptpd>

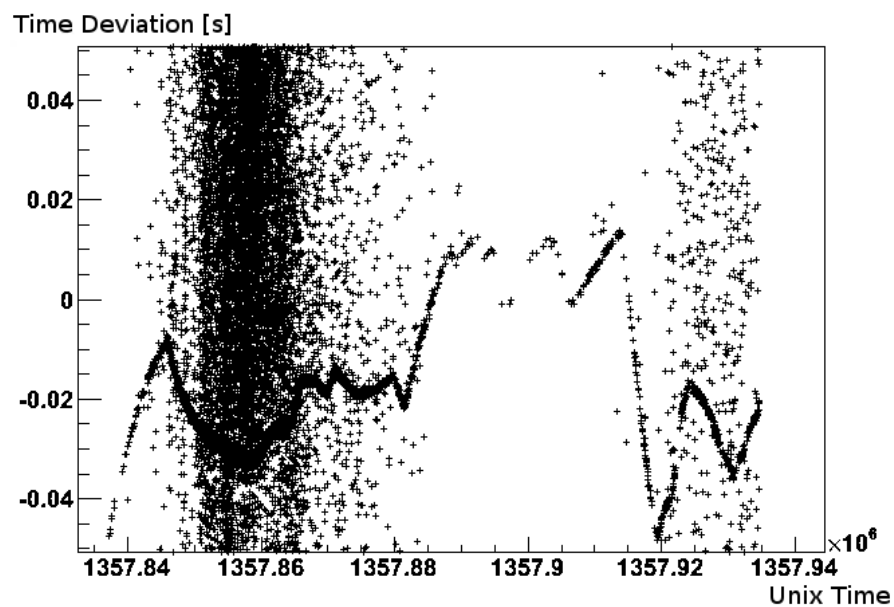
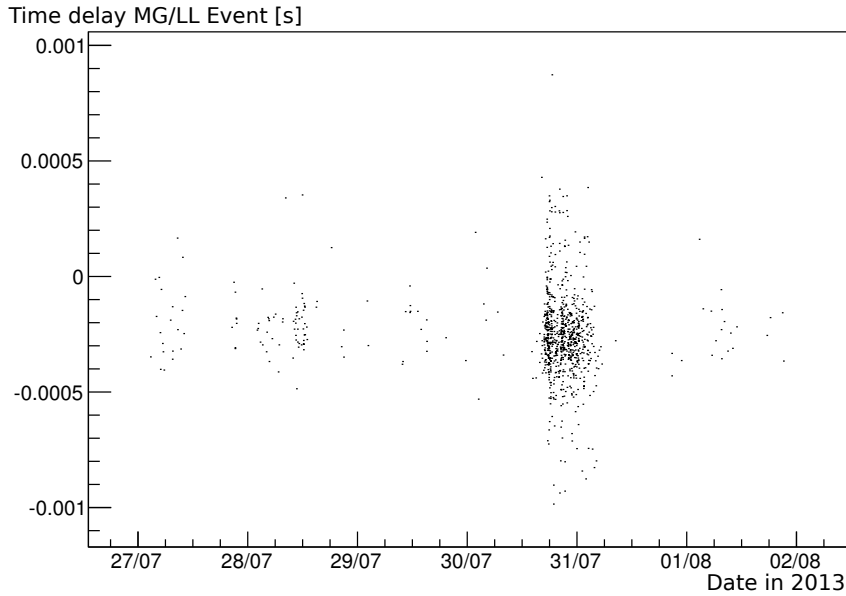
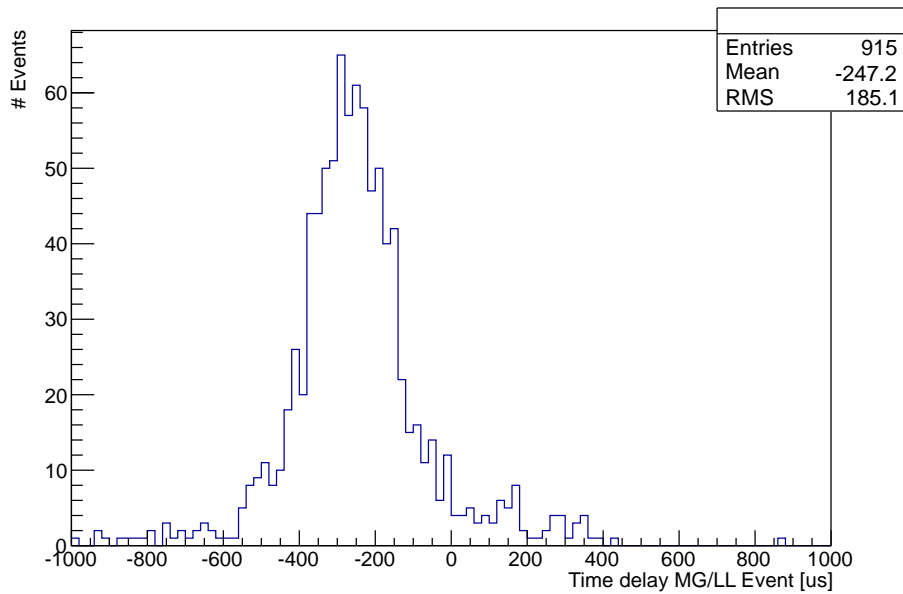


Figure 6.9: Network Time Protocol Timing accuracy: The plot shows on the y-axis the time difference in seconds of lightnings detected within 0.05 s in two stations against the UNIX time in seconds. One can clearly see a systematic drift in the timing. The two bands parallel to the y-axis around $x \approx 1357.86$ s, and $x \approx 1357.93$ s are due to many lightning events inside the large coincidence window used for this plot.

6.2. LIGHTNING DETECTION SYSTEM



(a) Data Points



(b) Histogram

Figure 6.10: PTP Timing accuracy: (a) shows the time difference of lightnings detected within 0.001 s in MG and LL against the date in 2013. (b) shows the distribution of the time difference for the range $\pm 1000 \mu\text{s}$ with a binning of $20 \mu\text{s}$.

6.2.4 GPS-Extension for Boltek StormTracker

The Boltek StormTracker provides an external trigger signal which can be used for time stamping the detected events. In this thesis an approach using the ublox LEA-6T chip⁶ is followed. A picture of the device is given in Fig. 6.11. This is a GPS timing module which has the advantage of an external input for time marking of external trigger signals. The read out of this module can be done via USB and there are Linux drivers available. The company Osmocom delivers a mounted timing board with the ublox LEA-6T. The Boltek StormTracker delivers a trigger signal with a falling edge if the card triggers and a rising edge, if the card is read out and again in operation to detect the next lightning. The module is connected to the external trigger input of the GPS-Module using a low pass. The low pass is needed to avoid multiple triggers per event due to oscillations in the trigger signal. For the low pass a capacitor of 330 pF and a resistor of 51 Ω is used, leading to a time constant of 17 ns and an upper frequency of ~ 10 MHz. The module has the capability of using the NMEA and UBX protocol, but as the timing operation is only available via the UBX protocol this is the one used in the detection software.

In the following the operating mode for maximum time accuracy is described. To increase the timing accuracy it is possible to set the GPS module in Time Mode Configuration. The Time Mode can be used for stationary devices, if the geographic location of the detector is known as exact as possible. For that it is needed to determine a *Survey-In*, where the mean position is calculated till a given accuracy and a minimum time is reached [131]. For the measurements in Argentina a minimum accuracy of 2 m and a minimum of two hours was used, except of Malargüe where a limit of 20 m was used because of the worse GPS reception.

Figure 6.12 shows the measured GPS accuracy of the devices in MG, LL, CO and LM. The GPS Signal in Malargüe is not as good as at the other detectors. The GPS Position in LL was moved to another position with better GPS reception, this is the reason for the small bump on the left side. The following table summarizes the results of a Landau fit applied on the data:

⁶www.u-blox.com/de/gps-moules/u-blox-6-timing-module/lea-6t.html

6.2. LIGHTNING DETECTION SYSTEM

| | MG | LL | CO | LM |
|------------|-------------------|---------------------|---------------------|-------------------|
| MPV [ns] | 131.7 ± 0.0 | 29.35 ± 0.0 | 28.52 ± 0.00 | 25.93 ± 0.01 |
| Sigma [ns] | 2.836 ± 0.013 | 0.4662 ± 0.0010 | 0.5385 ± 0.0010 | 0.876 ± 0.005 |

Table 6.1: GPS accuracy from figure 6.12. Shown is the Most Probable Value (MPV) and the sigma of the Landau fit for the accuracy of the different GPS devices.



Figure 6.11: ublox LEA-6T GPS Module

Each time mark contains beside a counter, the timing information for the last raising and falling edge an accuracy field. During the tests in Wuppertal the estimated accuracy from three GPS modules was ~ 30 ns. The accuracy is calculated by taking the uncertainty of the location and the Time Dilution of Precision (TDOP)⁷ of the GPS Signal into account. Since no absolute time source was available in Wuppertal an absolute measurement of the accuracy was not possible. But as there were three GPS modules available a relative comparison was possible. For that purpose the output of a function generator was connected to the external input of the GPS modules. A rectangular signal was applied to trigger the GPS modules at the same time and the time marks were read out. Comparing the measured time marks the relative accuracy is ~ 9 ns and as expected smaller than the given value for the absolute one provided by the GPS modules.

⁷[http://en.wikipedia.org/w/index.php?title=Dilution_of_precision_\(GPS\)](http://en.wikipedia.org/w/index.php?title=Dilution_of_precision_(GPS))

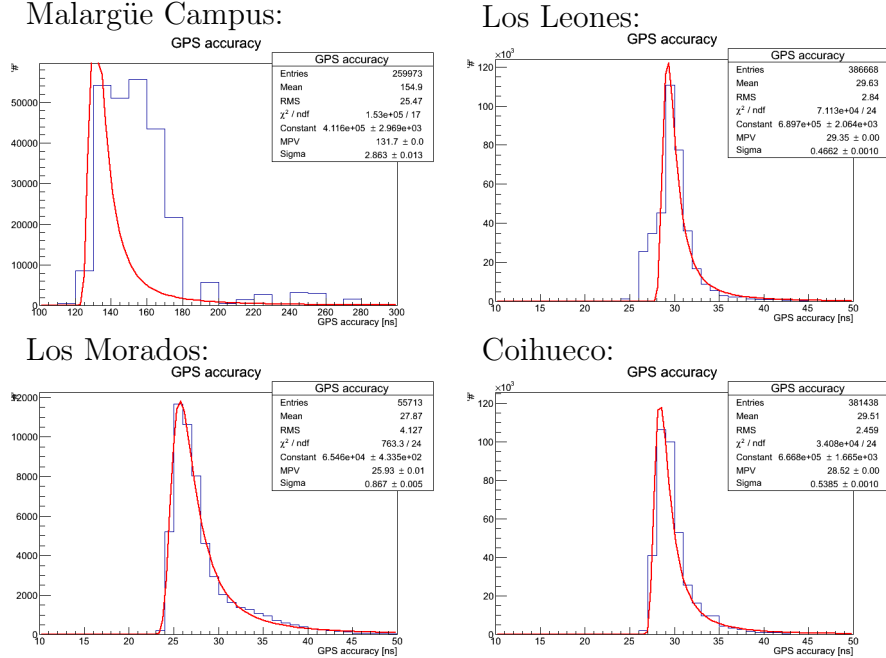


Figure 6.12: Histogram of the GPS accuracy estimated by each GPS module for each detected lightning in Argentina. A Landau fit (red line) was applied to data to estimate an mean value and deviation.

For a correct timing of the lightnings it is important to know the time delay of the Boltek StormTracker to provide the trigger signal if there is a lightning detected. The delay was measured similar to the measurement of the sampling rate. The function generator was used with the winded cable as antenna to trigger the lightning device. To get a clear starting time a rectangular function was used. With a PicoScope 6402⁸ the output of the function generator and the trigger signal was stored into a csv file, which was analysed with a root script to estimate the time delay of each measurement. The results were filled into a histogram and a Gaussian fitted to the data, figure 6.14. The result is a mean time delay for the trigger signal of $32.59 \pm 0.005 \mu\text{s}$, which must be considered in the later analysis. The used antenna cable (CAT-5) was 50 inch (15.24 m) in length, which leads to a delay of 4.2 ns.

This measurement was performed on one of the Boltek StormTracker cards in Wuppertal, since the other cards were at the time of the measurement already deployed in Argentina.

⁸www.picotech.com/picoscope6000.html

6.2. LIGHTNING DETECTION SYSTEM

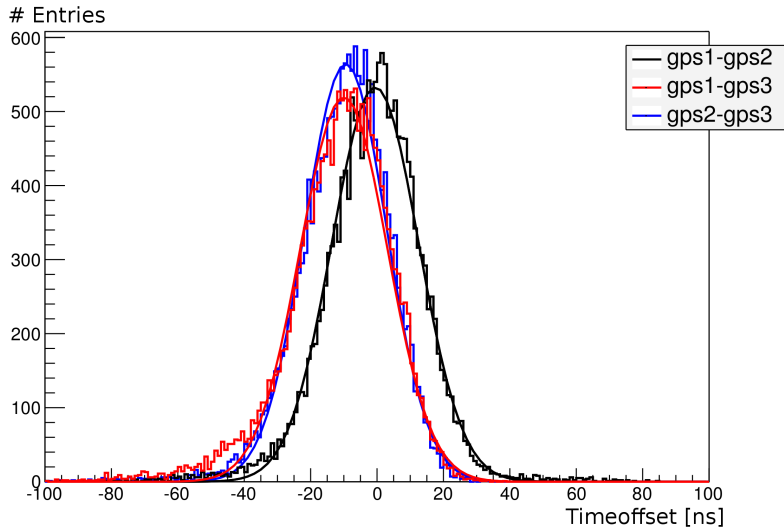


Figure 6.13: Deviation of GPS time marks in ns of three ublox LEA-6T to each other for test measurements in Wuppertal at the same position.

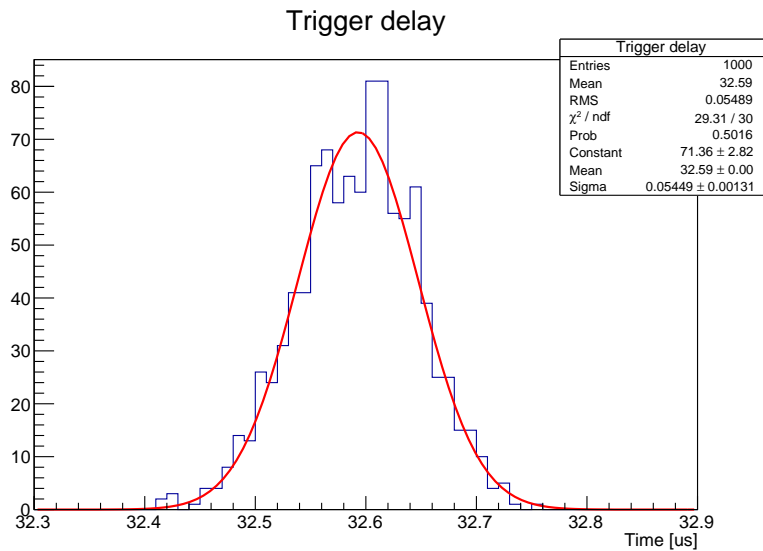


Figure 6.14: Histogram of the measured StormTracker trigger delay in μs . A Gaussian fit is drawn in red.

6.2.5 Dead Time

The read out of the data from the StormTracker and the GPS Device takes some time. During this time span no lightning detection is possible. The evaluation of this dead time is shown in this paragraph.

The easiest way of estimating the dead time is calculating the time between two following lightnings detected within one station. This is plotted in Fig. 6.15. The dead time for all detectors is about 45 ms, where no events were measured, followed by a peak between 50 ms and 200 ms, probably due to multiple triggers related to the same lightning and followed by a flat distribution afterwards. The differences in the sharpness of the falling edges, especially at the device in Malargüe, could be related to the GPS accuracy of each device.

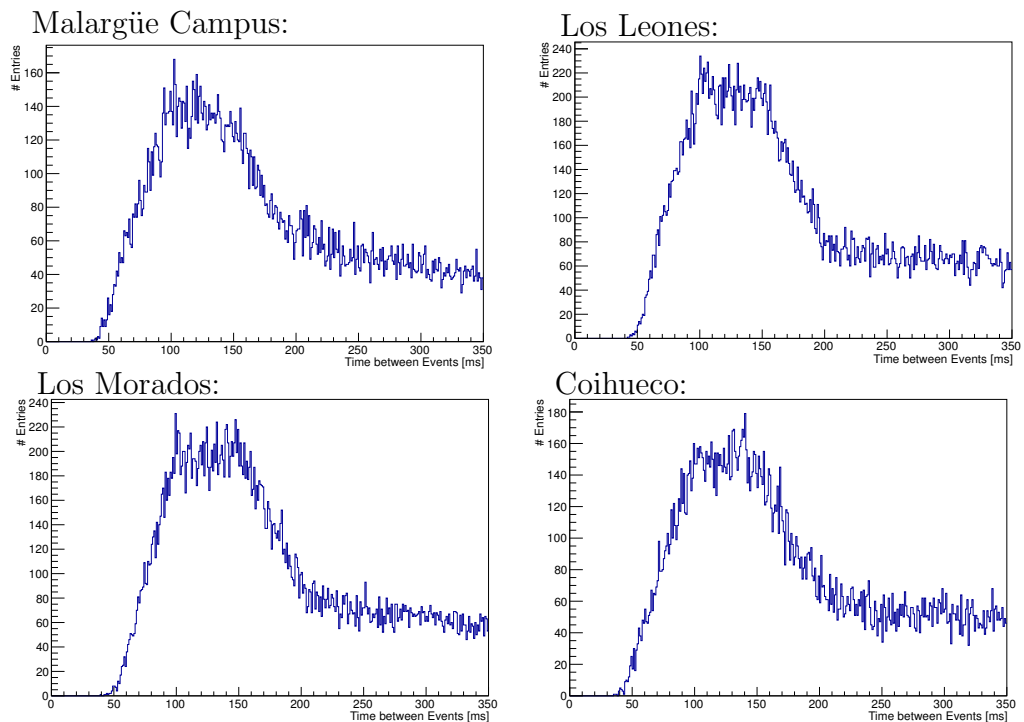


Figure 6.15: Time between two following events in ms to estimate the detector dead time.

6.3 Integration in the Auger Monitoring Page

After discussing the timing accuracy this paragraph describes how the data is provided at the Auger monitoring page. Within this thesis additional sites and tabels for the lightning detection systems were attached to monitoring system (website and database).

Each day at 1:00 o'clock the E-field data of the 24 hours are written to the MySQL database. The E-field data are stored in the database *AERA* inside MySQL. The table *Field* contains the data of the E-field mill located at the CRS, FieldBLS at the BLS and FieldAERAWS within the AERA extension. The table structure is the same for all:

| Field | Type | Null | Default |
|------------------|------------|------|-------------------|
| <i>TimeStamp</i> | timestamp | Yes | CURRENT_TIMESTAMP |
| Record | int(11) | Yes | NULL |
| Field | float | Yes | NULL |
| IsTS | tinyint(1) | Yes | NULL |

Table 6.2: Structure of table Field

Each entry contains the timestamp of the measurement, a running event ID (Record), the measured E-field (Field) in V/m and the Thunderstorm flag (IsTS; 0 = no thunderstorm condition, 1 = thunderstorm condition, 2 = lightning indication, 3 = lightning discharge).

Within this thesis the programs *FindTS*, *FindTSBLS* and *FindTSAeraWS* have been developed to perform the lightning detection based on section 6.1.1. They are available at <http://at-web.physik.uni-wuppertal.de/svn/Lightning/>. The following cron job calls them at 1:45 o'clock every night, after the data have been filled to the database, to evaluate the data with regard to lightning events. The programs needs to be called with the parameters '*TimeStampStart*' and '*TimeStampStop*' with the format '*YYYY-MM-DD*'.

```
# m h dom mon dow  command
45 01 * * * FindTS $(date --date "yesterday" +%Y"-"%m"-"%d)
    $(date +%Y"-"%m"-"%d) > Efield_CRS.log
50 01 * * * FindTS_AERAWS $(date --date "yesterday" +%Y"-"%m"-"%d)
    $(date +%Y"-"%m"-"%d) > Efield_AERAWS.log
```

The pages of the monitoring homepage are written in PHP and the plots are created with JpGraph⁹. Each detector component has its own web site in

⁹<http://jgraph.net>

the monitoring. The E-field data and the lightning data are implemented in the *AERA* part.

The data is made available to the Auger collaboration via the Auger monitoring web-page¹⁰ and its European mirror¹¹ to minimize the network traffic to Argentina.

The E-field data is provided at *AERA*→*weather conditions* of the monitoring homepage. There is the measured E-field for each E-field mill plotted against the time. In addition the lightning flags are shown. The shown time interval can be adjusted with the *Time Preferences* setting in the side bar on the bottom of the monitoring page.

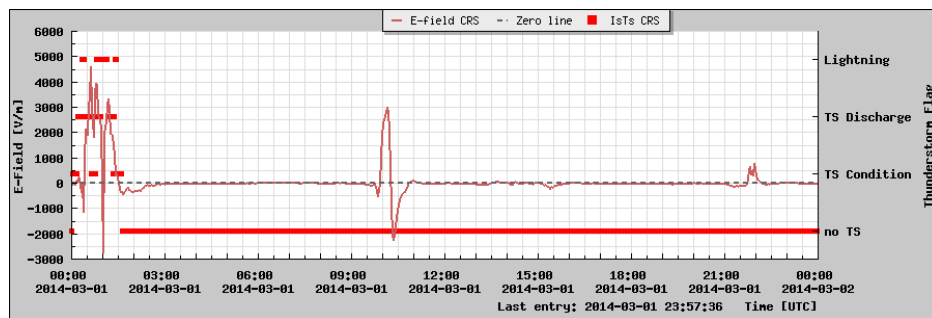


Figure 6.16: E-field plot in the monitoring. The lightning flags are also available.

The LDS data are provided as single station data in the monitoring at *AERA*→*Lightning*. Figure 6.17 shows the detected lightnings at each station in a plot with polar coordinates. In addition in figure 6.18 the lightning rate for each station in number of lightnings detected in 10 minutes is plotted against the time.

¹⁰<http://moni.auger.org.ar/>

¹¹<http://paomon.uni-wuppertal.de/>

6.3. INTEGRATION IN THE AUGER MONITORING PAGE

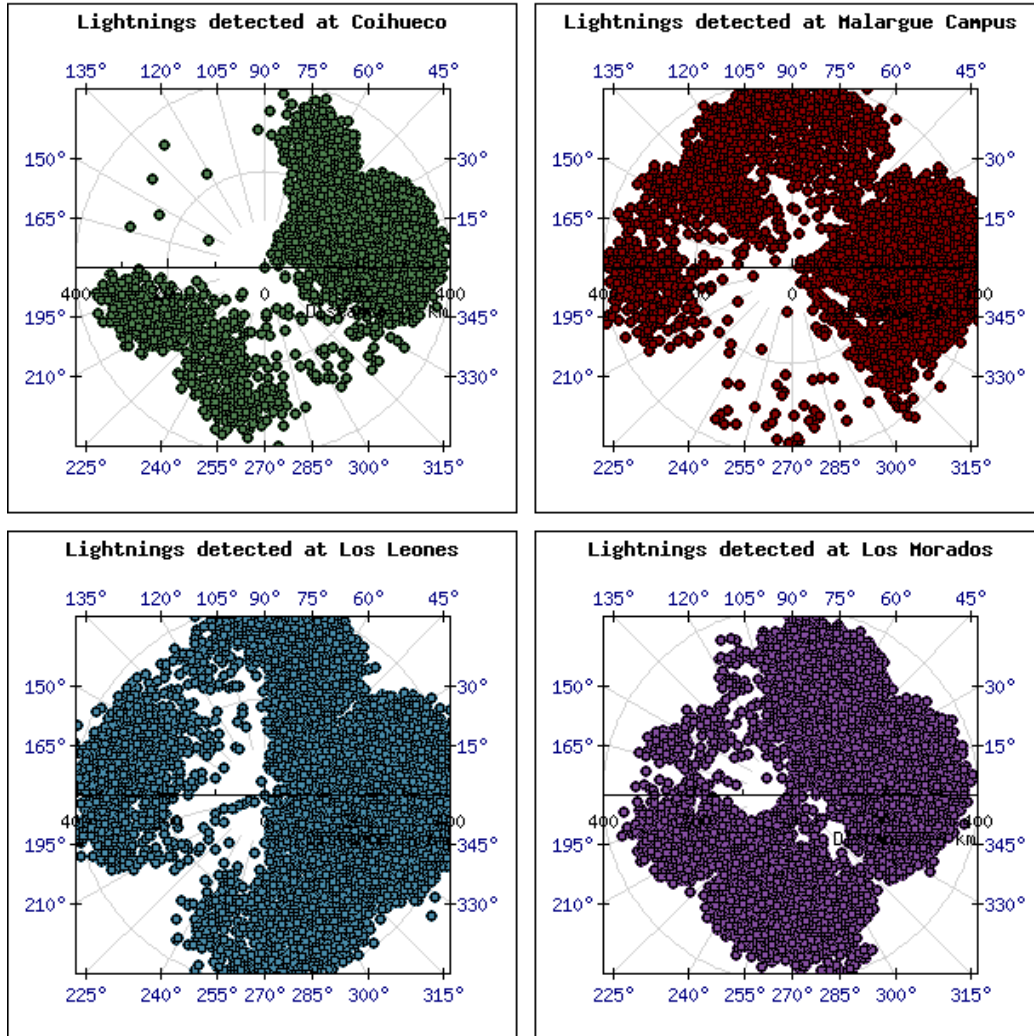


Figure 6.17: Single Lightning Station Data in the Auger monitoring^{10,11}. The direction in degree is plotted with respect to east as 0° , counting counter clockwise with north at 90° .

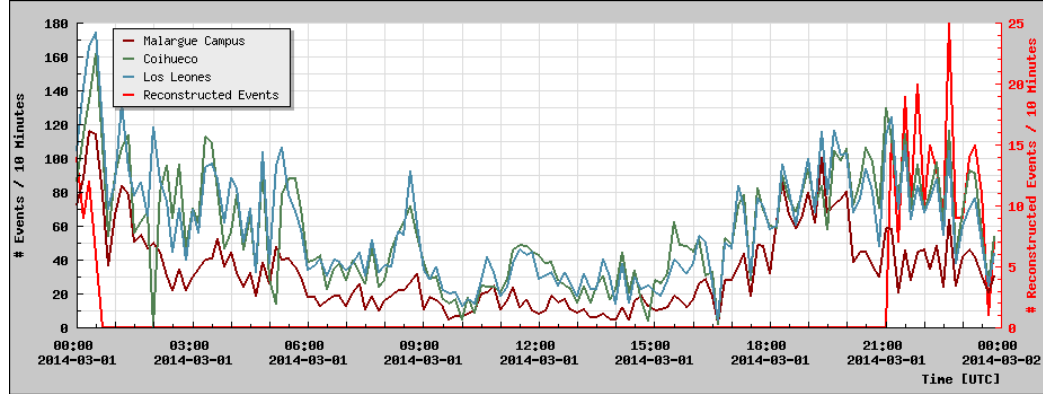


Figure 6.18: This plot shows the lightning rate for each detector in the Auger monitoring for 1st of March 2014. The rate is given in number of lightning events in a 10 minutes time interval. In this example the rates for Malargüe, Coihueco and Los Leones are shown. Also the number of successfully reconstructed lightnings with the MySQL function described in this section is plotted, note the separate scale on the right.

The LDS data are written online to the MySQL database. If at least 3 stations within a time window, given from the maximum distance of the detectors to each other divided by the speed of light, report a lightning event, a MySQL function automatically determines the position and time of the lightning event. In the following the working principle of this function is described. On the MySQL server runs a trigger which searches for coincident lightning events in at least 3 stations a reconstruction function inside MySQL to get the position and time of the lightning. This MySQL function is based on a time of arrival reconstruction.

For the real lightning at time t and position (x,y) the time of the detected lightning t_i at each detector i at position (x_i,y_i) is using the speed of light, c :

$$t_i = t + \sqrt{(x_i - x)^2 + (y_i - y)^2}/c. \quad (6.3)$$

The distance from each detector to the lightning position s_i is described as:

$$s_i(x, y) = \sqrt{(x_i - x)^2 + (y_i - y)^2} = s_0(x, y) + (t_i - t_0) \cdot c. \quad (6.4)$$

Rearranging equation 6.4 yields $s_{0,i}$ the distance of the lightning event from detector 0 calculated using data from detector i :

$$s_{0,i}(x, y) = \sqrt{(x_i - x)^2 + (y_i - y)^2} - (t_i - t_0) \cdot c \quad (6.5)$$

6.3. INTEGRATION IN THE AUGER MONITORING PAGE

Without any measurement errors $s_{0,i}$ are equal for all detectors. Since in reality measurement errors in general lead to deviating values of $s_{0,i}$ the position of the lightning $P(x', y')$ is approximated using equation 6.6.

$$P(x', y') = \min \left(\sum_{i \neq j} (s_{0,i}(x', y') - s_{0,j}(x', y'))^2 \right) \quad (6.6)$$

The minimum of function 6.6 is found in a fit with the root function TMinuit implemented to the MySQL function.

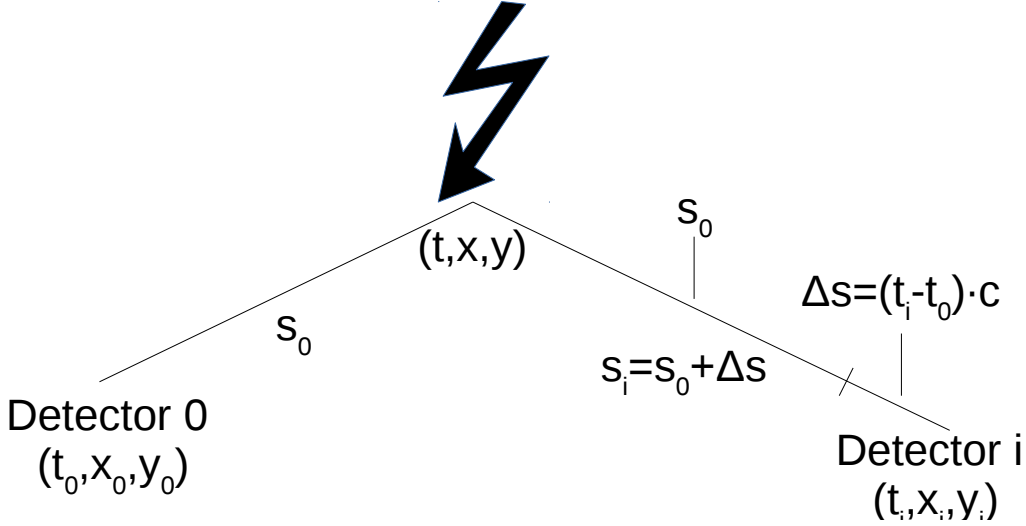


Figure 6.19: Sketch of the working principle of the lightning reconstruction function. The lightning event at (t, x, y) is detected at detector 0 (t_0, x_0, y_0) and detector 1 (t_1, x_1, y_1) .

In order to determine the event position as accurately as possible, it is important that the event time is as precise as possible. The LDS triggers if the measured value of the field in one polarization is above a given threshold. To increase the accuracy of the timing an additional time offset for each detector with respect to the first detector is calculated using the cross correlation of the measured signal. For that purpose the single event data, containing the traces, are fetched from each triggered lightning PC via FTP.

An absolute signal for each detector i and each time bin j is calculated, by using the square root of the sum of the squared raw signal for both polarizations:

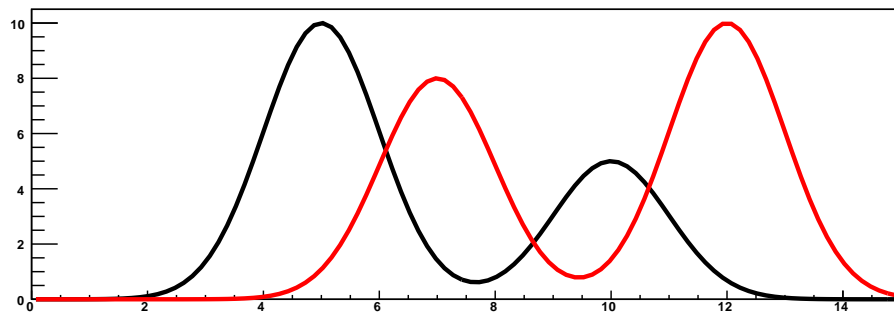
$$S_{i,j} = \sqrt{S_{i,NS,j}^2 + S_{i,EW,j}^2} \quad (6.7)$$

To find the best offset the cross correlation method is used and $CC(\text{offset})$ is maximized:

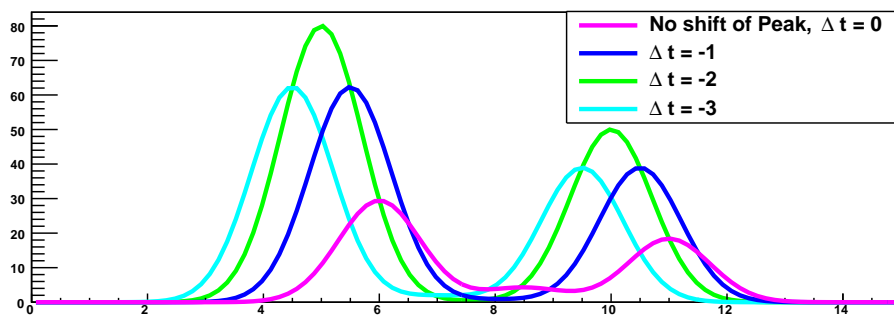
$$CC(\text{offset}) = \max \left(\sum_j (S_{0,j} \cdot S_{i,j+\text{offset}}) \right) \quad (6.8)$$

$$\Delta t_i = \text{offset} \cdot 125 \text{ ns} \quad (6.9)$$

The time mark of each detector is corrected by adding the time offset Δt_i . An example trace, the cross correlation values and the shifted traces are given in figures 6.21.



(a)



(b)

Figure 6.20: Schematic representation of the cross correlation method. (a) shows two signals of each two Gaussian in black and red. The offset of the maximum of both Gaussian is the same for both curves, but the black has the maximum amplitude at the first Gaussian and the red one at the second Gaussian. (b) shows the cross correlation signal for different time offsets of the red curve with respect to the black one. Both signals match the best to each other at the maximum cross correlation value, in this example $\Delta t = -2$.

6.3. INTEGRATION IN THE AUGER MONITORING PAGE

The determined lightning positions and times are written to the MySQL database where they can be accessed later. In addition, they are sent to CDAS via udp packages to generate a lightning trigger for the surface detector (described chapter 9), a sketch of the data flow is shown in Fig. 6.22.

The improvement of the reconstruction accuracy by applying the time shift of each trace estimated with the cross correlation method can be seen later in the comparison of figures 8.9 and 8.10 in section 8.2.

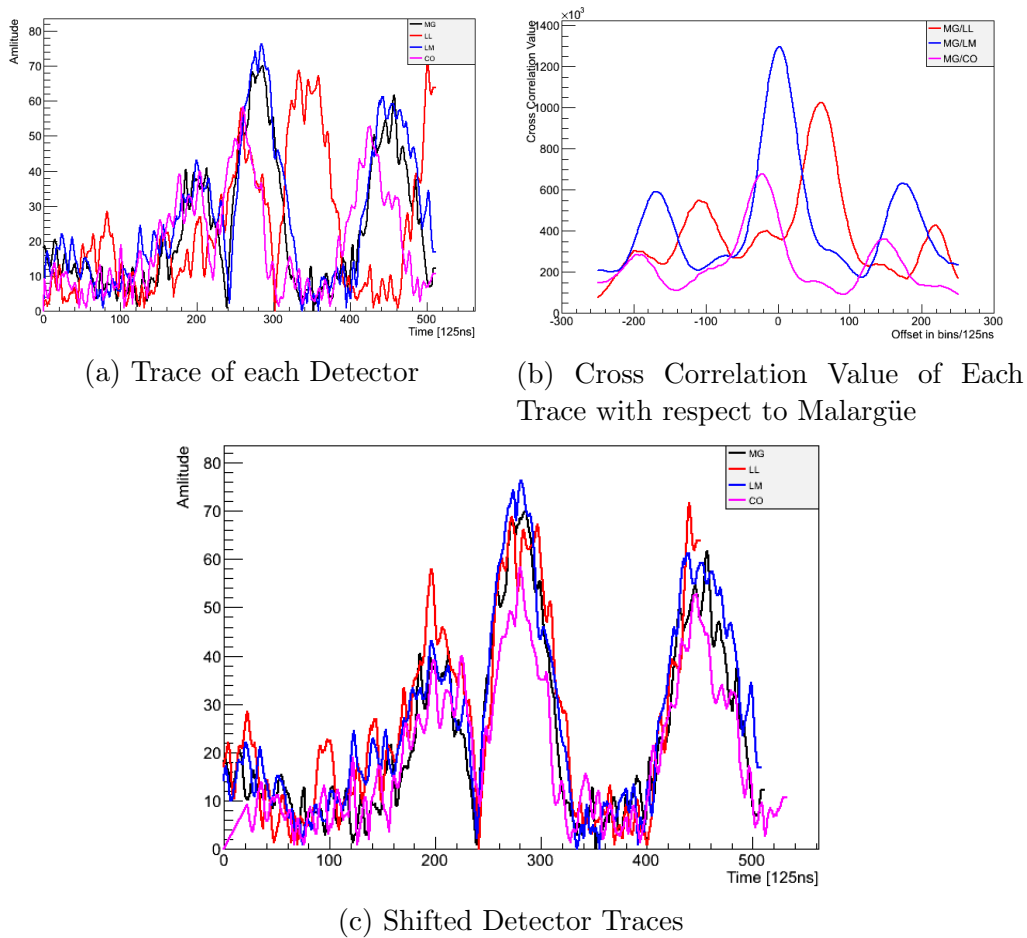


Figure 6.21: (a): Raw trace of the LDS. E-field amplitude over time for the detectors at Malargüe, Los Leones, Los Morados and Coihueco. The traces show a deviation in their timing. (b): Cross Correlation between the Malargüe station and of the stations CO, LL, LM as a function of the time shift. (c) E-field amplitude over time considering the time shift according to the position of the maximum cross correlation value obtained from figure (b).

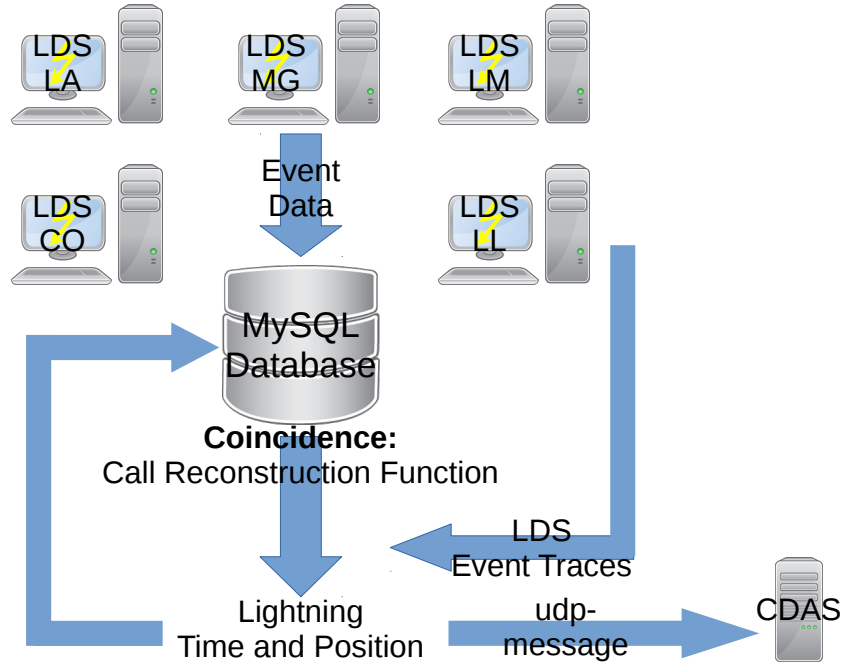


Figure 6.22: Sketch of the MySQL data flow.

For the visualization of the reconstructed lightnings in the Auger monitoring an OpenStreetMap is included where the position of the found lightnings are marked with additionally six colour scaled time bins, figure 6.23. In the shown data period from 28.02.14 21:00:00 ART till 01.03.14 21:00:00 ART there were two time bins within detected lightning events. One period from 28.02.14 21:00:00 ART till 01.03.14 01:00:00 ART and the other one from 01.03.14 17:00:00 ART till 01.03.14 21:00:00 ART. At this time three LDS were taking data. The events aligned to south-east are due to geometric effects from the detector set-up, which can be simulated, compare section 7.

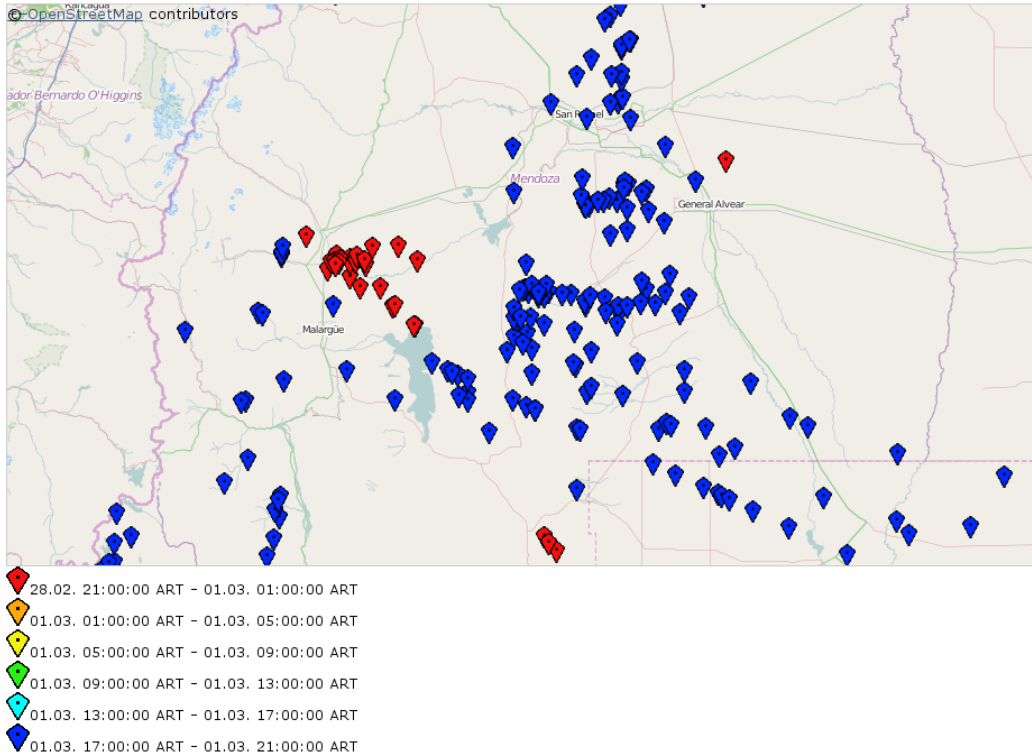


Figure 6.23: Open Streetmap lightning map in the Auger monitoring page. The found lightnings are marked with a coloured flash which shows the position and time in colour scale.

6.4 AERA-Stations

The following section describes how lightnings can be detected with the stations of the AERA extension. For this some changes in the Auger analysis framework Offline were applied.

The New Mexico Tech Lightning Mapping Array (LMA) is a professional lightning detection system. It uses the VHF radiation emitted by lightnings in the frequency spectrum of 60-66 MHz and sample their data with 10 kHz. With this set-up they reach a spacial resolution of ~ 100 m over the detector array [132]. As the frequency ranges of LMA (60-66 MHz) and AERA (30-80 MHz) are similar, it should be possible to detect lightnings with the AERA stations. The sampling rate of LMA (10 kHz) is lower than the one of AERA (200 MHz) which should lead to an even better reconstruction of triggered lightnings. Additionally the buffer of the AERA hardware has the capability of storing traces with 8 s length which would be sufficient as light-

ning strikes can reach the duration of a few seconds. But for that one would have to change the DAQ software of the stations, which is not planned.

6.4.1 Implementation of Cross-Correlation in Offline

The AERA standard reconstruction in Offline was developed to analyse short radio pulses for each triggered radio event. These are reconstructed with a position on ground and a direction of the event in θ and ϕ . For that purpose it is sufficient to create a time stamp for each station by using the maximum amplitude. Lightnings have long traces, with multiple oscillations. This leads to the problem, that the position of the maximum amplitude differs for different stations. To get a better timing for each station to each other the cross-correlation method is used to calculate the time offset of

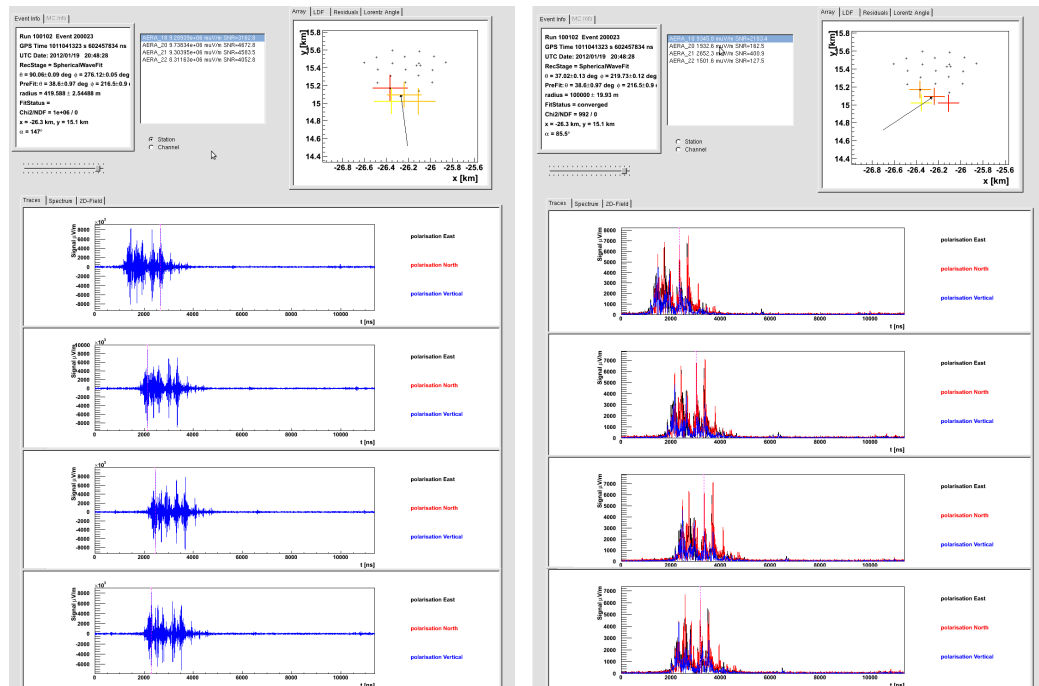


Figure 6.24: This figure shows the traces of each triggered detector of the AERA event 200023 from the Auger Event Display. On the left the standard reconstruction is shown. A vertical red line shows the position of the maximum, which is used as time mark for the reconstruction. On the right the cross correlation was used to calculate the time shift of the stations. Additionally the Hilbert envelope was used. One can see, that now always the corresponding point to the maximum in the first trace is used as time mark.

each trace with respect to the first one. Adding this offset to the GPS time stamp of each station one gets the corrected timing, which can be used for the reconstruction. Figure 6.24 shows an example of AERA traces under lightning condition. Without using the cross correlation method the time stamps in each station do not match to each other, while using the cross correlation method results are in a good agreement.

6.4.2 Data Analysis

The cross correlation method was applied in the Offline reconstruction to increase the quality of the time stamps for each detector, with respect to the trace of the first station. Figure 6.25 shows the angular distribution of events for the data period of 19.01.2012 20:39:29 - 21:35:30. This period was

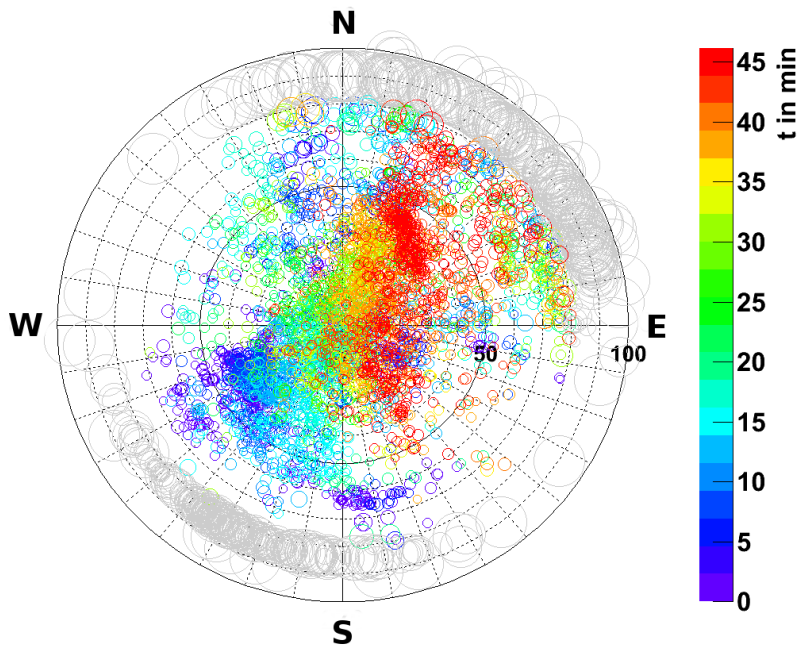


Figure 6.25: Angular distribution of reconstructed AERA events from t_0 19.01.2012 20:39:29 till 21:35:30 UTC with colour coded timing information. The size of each marker is proportional to the reconstructed energy and the direction in azimuth and the zenith as radius in degree. The gray circles are rejected events at the horizon. The events show a movement with time over the AERA array during a lightning period which was detected with the E-field mill.

detected as a lightning period with the E-field mills. Using the new timing method the number of events which get reconstructed to the horizon gets lower. This number is an indicator for the reconstruction quality as most events with wrong timing are reconstructed towards the horizon.

The normal signal for an air-shower is a short pulse on the order of several ns. Therefore, the standard reconstruction uses only a small signal window within the trace to search for a peak. The stored trace of each AERA event is larger than the used signal window, the time period in each trace which is used for the reconstruction. To get more possible lightning information out of each AERA event the events were analysed two times, first with a signal window from $1-5 \mu\text{s}$ and for the second run the time window was shifted to $5-10 \mu\text{s}$. With this data set for every detected lightning indication point with the E-field mill the AERA events in a time window of 1 s before and till 3 s after each lightning are plotted. For each lightning indication point several AERA Events can be within this time window. The negative time offset is used, because of the sampling rate of the E-field data of 1 per second. Figure 6.26 shows the development of the lightnings in one direction to northeast with time.

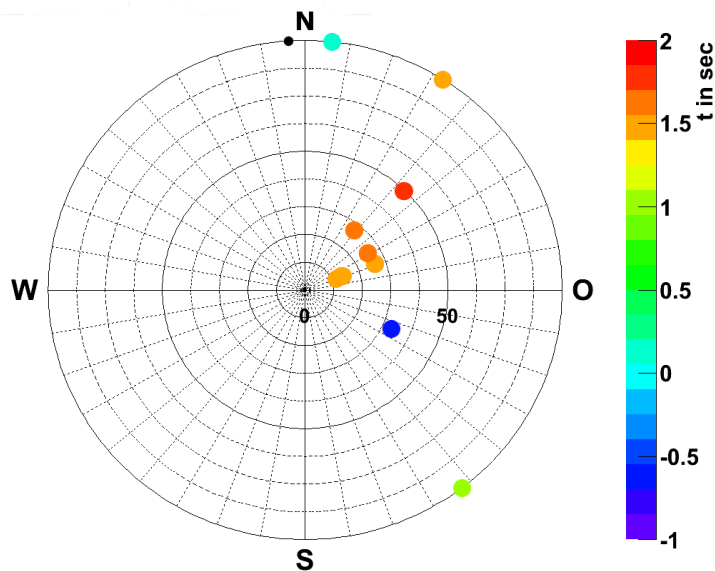


Figure 6.26: Angular distribution of reconstructed AERA events in a time window of -1-3s before around the detected lightning at 19.01.2012 20:52:11 with the E-field mill. In colour code the timing information is given.

Summarising, this shows, that it is in combination with the information from E-Field mills possible to detect lightnings with AERA. For the future one can think about changing the DAQ software to get longer traces which would be necessary for a high quality reconstruction of lightning events.

With LOPES a similar analysis for lightning events was made, they used the beam forming method to estimate the lightning position in dependence of time [85]. This could be promising for the Pierre Auger Observatory, where the implementation of beam forming inside Offline is under construction.

6.5 SD Lightning Flag

After describing the lightning detection with the AREA extension this section is about the lightning flag of the Auger surface detectors. The surface detectors have a very sensitive electronics. Lightning produces high frequent noise, which can be detected by the surface detectors. The PMT cable works as an antenna and noise peaks, for example from lightnings, can be high enough to create a trigger. The lightning noise inside the traces has a characteristic pattern, which makes possible to mark these events in later analysis as lightning. A typical trace is shown in figure 6.27. An online detection is not possible. For the standard Auger analysis these events are rejected [133]. The number of lightning triggered stations for each lightning has a huge variation. While some lightnings are detected by only one station, others are detected by more than 100 stations. Knowing the position of the stations makes possible to

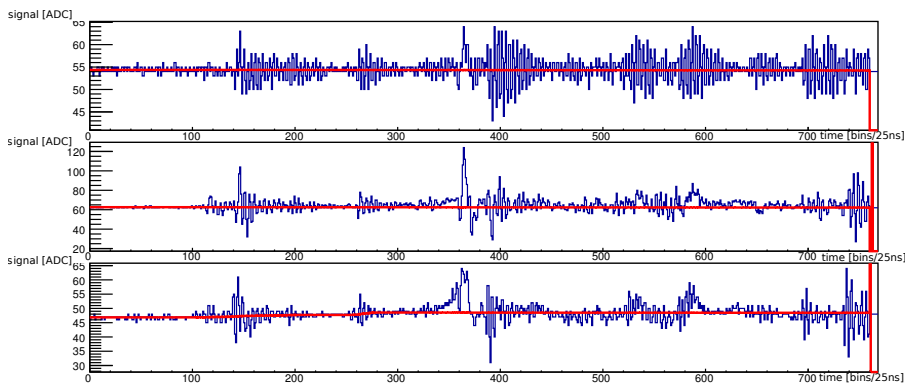


Figure 6.27: Typical FADC trace of a SD event detected as lightning. The signal in ADC of each PMT in one station is shown against the time in bins per 25 ns.

estimate the position of the lightning by calculating the mean position of all triggered stations. The accuracy of the position is approximated with the standard deviation of the spacial distribution. The timing accuracy of the lightning flags is given with μs precision. The detected lightnings will be compared in later analysis to the different lightning detection mechanism. With the surface detectors it is possible to detect lightnings and to approximate a position and time of each event. Figure 6.28 shows the positions of the events with SD lightning flag in 2014. These are compared to the other lightning detection mechanism in section 8.2.

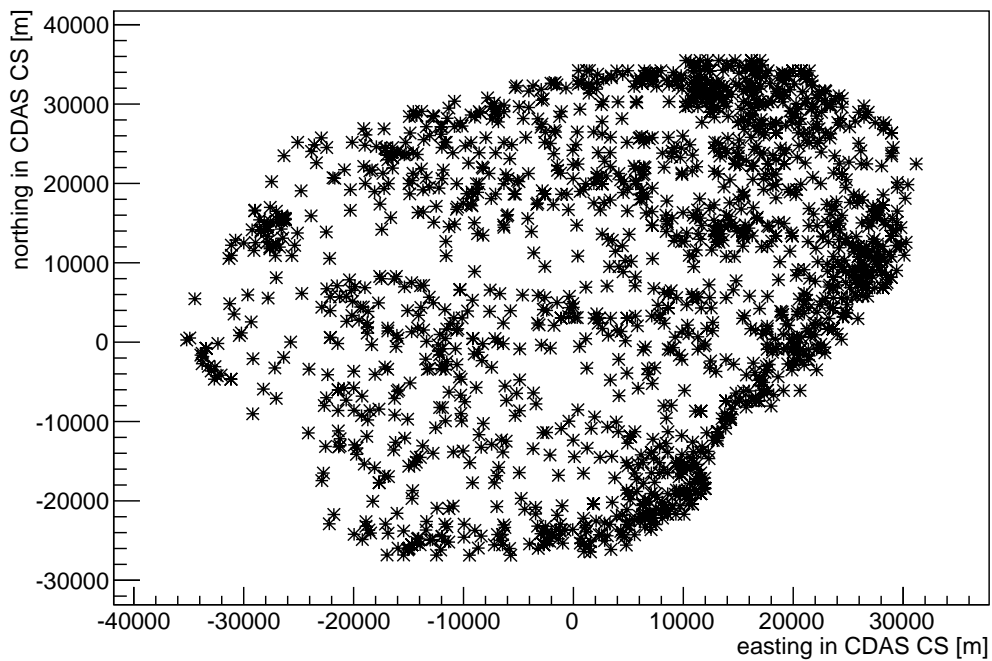


Figure 6.28: Map of all SD Lightnings in 2014 given in northing and easting in CDAS coordinate system.

Chapter 7

Accuracy of Lightning Position

The following section describes the calculation of the position accuracy which can be achieved using the Lightning Detection Station (LDS).

The accuracy of the reconstruction of the lightning position depends on the timing accuracy of each LDS, the detector geometry and on the number of triggered detectors. To get an overview of the accuracy which can be expected for the reconstruction using three, four or five station a simulation was performed including the measured timing accuracy for each station and its position.

For random positions the time delay at each lightning detector given from the distance and the speed of light was calculated. These time delays were folded with a Gaussian with a width given by the GPS-accuracy and half the binning of the detector trace (65 ns). The used number of simulated lightnings is 10 times the number of bins for each plot. The positions are given in northing and easting in the so called CDAS coordinate system (CDAS CS), which has its reference point (0,0) almost in the center of the array at latitude = 35.25° S and longitude = 69.25° W.

Figure 7.2a shows the reconstruction accuracy of lightnings at positions in a range of 500 km to each direction using all lightning detectors. Inside the array, figure 7.2b, the reconstruction works fine, with an uncertainty of ~ 10 m. If one goes farther outside, the accuracy drops to ~ 10 km at 500 km distance. Figure 7.1 shows the histogram of the deviation from figure 7.2a in the distance from the source to the reconstructed position up to a distance of 10 km. In the plot one can see the steep falling of the number of events with an reconstruction error larger than ~ 100 m. The steepness depends of course on the selected maximum distance used for the simulations, as events near by can be better reconstructed than events in a larger distance.

Especially for lightnings outside of the array the estimation of the direction and distance are clearly different, making a polar representation more useful,

as given in figure 7.3. As can be seen, the accuracy is usually about 2.5% in distance and 0.06° in direction.

Using only four of the five stations leads in a loss of position accuracy, which can be seen in Fig. 7.4. Inside the array the detection is compatible with five stations, but for larger distances to the array center the accuracy drops faster. Using four stations leads to an uncertainty of ~ 10 km at 200 km distance. Because of the detector geometry where CO, LL, LM and LA are at the corners of a square and MG and LL are very near by to each other the reconstruction along the parallel lines to the detectors gets difficult which one can see at the red lobes with a reconstruction error larger than 100 km.

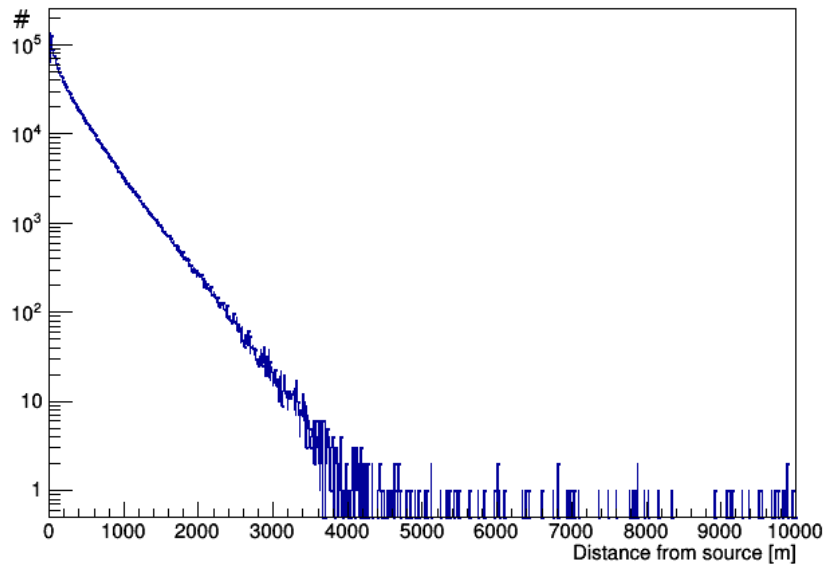
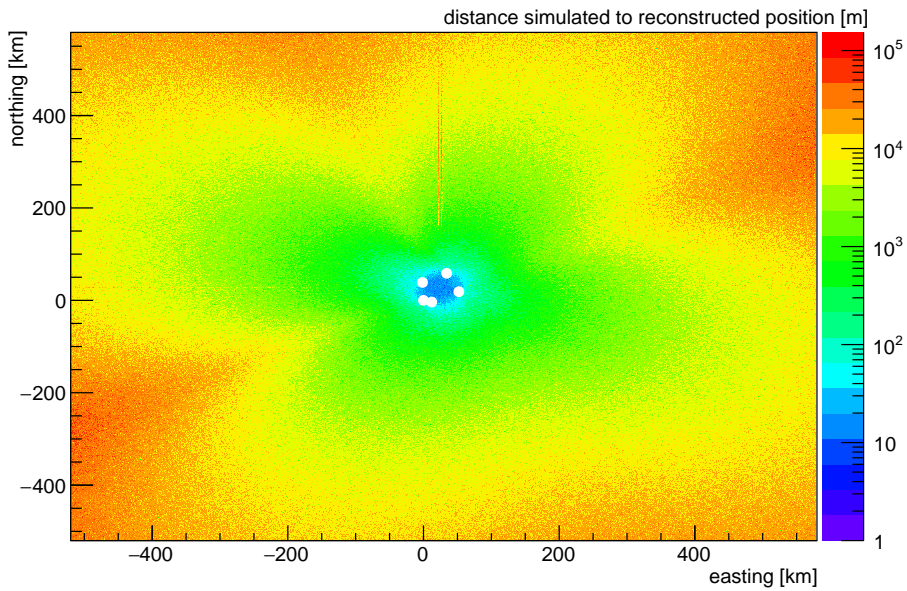
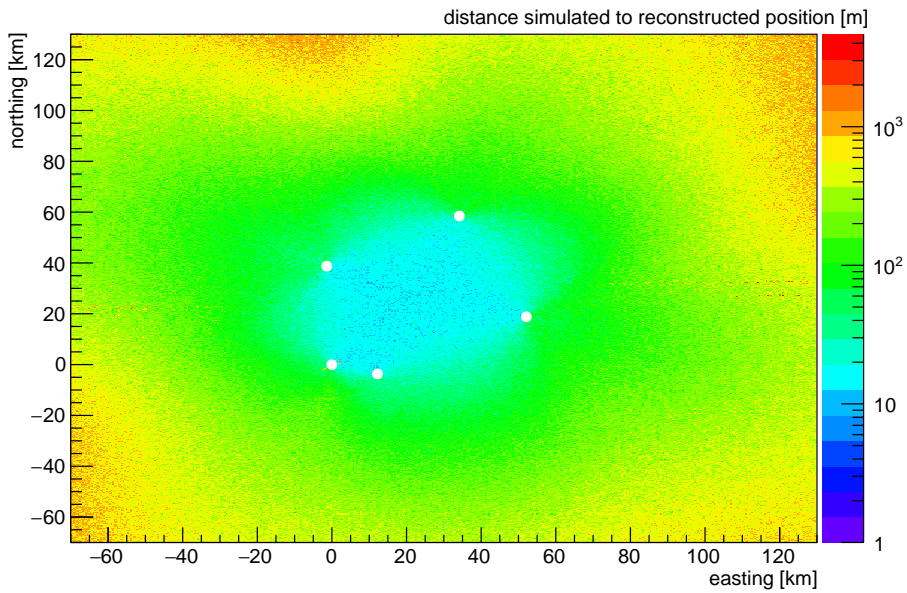


Figure 7.1: Histogram of reconstruction accuracy from simulations for events near by the detector array. This histogram shows the number of events on a logarithmic y -axis against the deviation from the source position to the position of the reconstruction of the lightnings on the x -axis from the simulations in figure 7.2a. The number of events drops fast after the maximum at ~ 10 m.

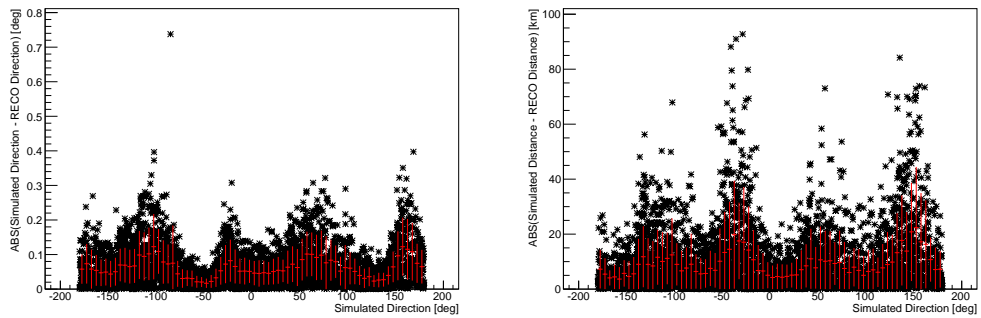


(a) Reconstruction accuracy using 5 stations in a range of 500 km.

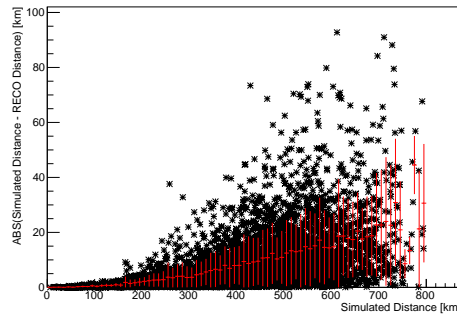


(b) Reconstruction accuracy using 5 stations in a range of 100 km.

Figure 7.2: Reconstruction accuracy of simulated events using five detectors. The color code shows at the source position, in northing and easting in CDAS CS, the distance to the reconstructed position in km. The white circles mark the positions of the lightning detectors. Especially inside the detector array the accuracy is better than 100 m.



(a) difference between reconstructed and simulated direction vs direction (b) difference between reconstructed and simulated distance vs direction



(c) difference between reconstructed distance and simulated distance vs the distance

Figure 7.3: Reconstruction resolution for simulated lightning events smeared according to the absolute time accuracy of the GPS modules. Shown is the difference between reconstructed and simulated direction (a) and distance (b) to the array center vs the azimuth of the direction, as well as the difference in the distance vs the distance (c). In red are the profiles drawn.

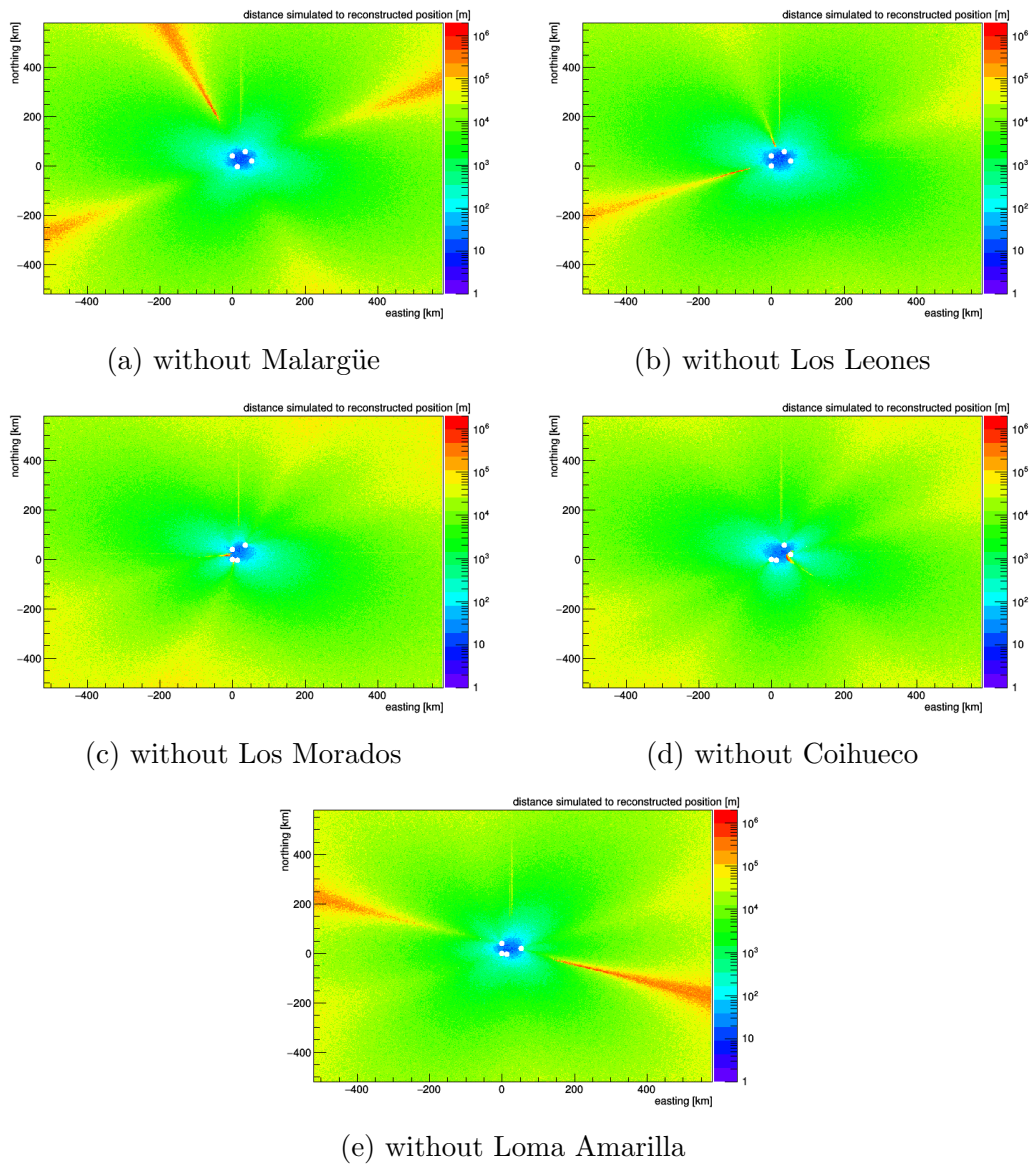


Figure 7.4: Reconstruction accuracy of simulated events using four of the five detectors. The colour code shows at the source position, in northing and easting in CDAS CS, the distance of the reconstructed position in meters. The white circles mark the positions of the lightning detectors.

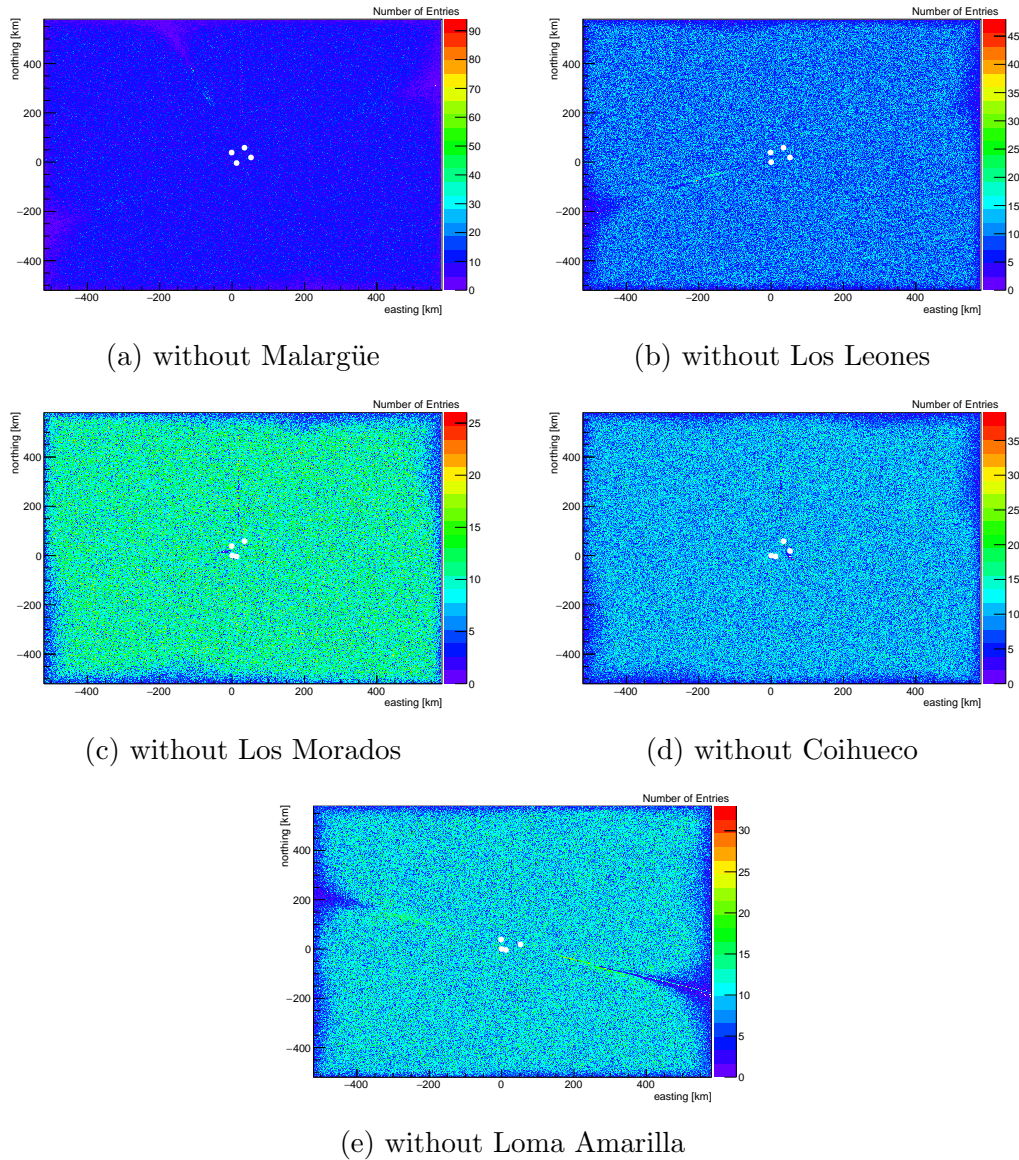
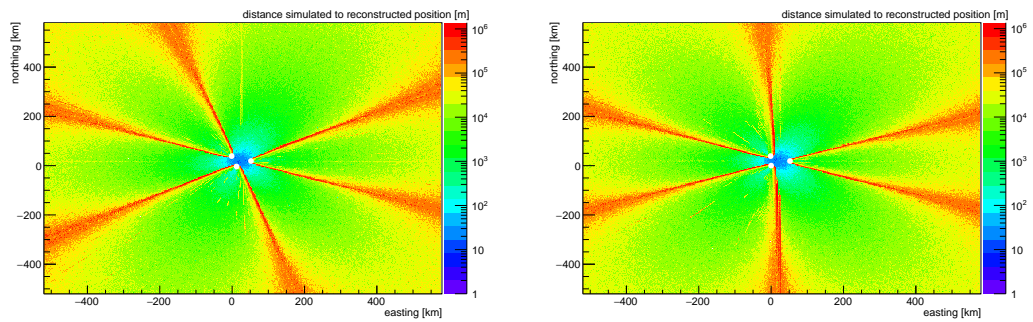


Figure 7.5: Position of the reconstructed events using four of the five detectors from a uniform source distribution. The colour code shows the number of events reconstructed to the position in northing and easting in CDAS CS, note the different scale on the z-axis. The white circles mark the positions of the lightning detectors. One can see especially in the plots without Malargüe, Los Leones and Loma Amarilla an access with many events detected to which are originally further outside. The same can be seen in data, figure 6.23.

Using only three of the five stations results in the simulations to a huge loss of position accuracy as can be seen in Fig. 7.6. Especially if CO or LM are not taken into account. The baseline from MG to LL is too small to get qualitatively good results. If CO and LM are used, the use of MG or LL as third detector does not change the result. Another problem with three station events is, that for some parameters the timing for events inside the triangle, build by the three detectors, is the same as outside. This can result in a wrong position. Inside the array the detection works even with only three detectors, but since the rate of events reconstructed from far away nearby the array these data cannot be used with a high certainty.

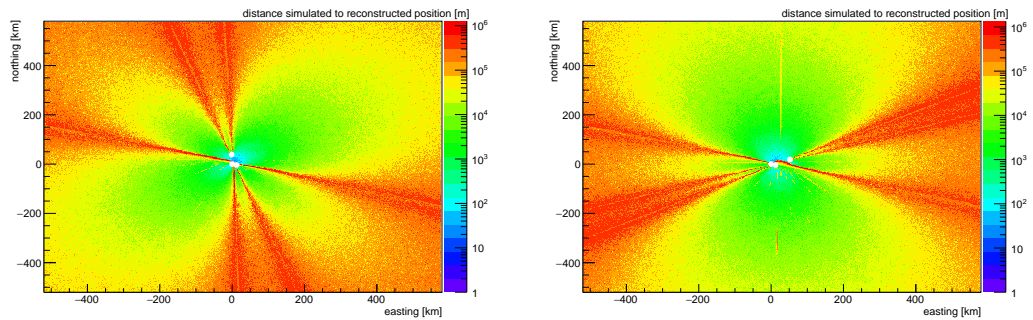
These simulations show, that especially inside the array the reconstruction with at least four lightning detectors works very well. But using four detectors has the disadvantage that for some directions still systematic effects due to the geometry occur, which result in an excess of events from south east, which one can see in the data as well as in the simulations. Events from that direction get reconstructed too close. Using only five lightning detectors reduces this effect, but lowers the number of coincident events and the total uptime, since only data periods can be used where all stations were working.

without Loma Amarilla and



(a) without Malargüe

(b) without Los Leones



(c) without Los Morados

(d) without Coihueco

Figure 7.6: Reconstruction accuracy of simulated events using three of the five detectors. The colour code shows at the source position, in northing and easting in CDAS CS, the distance of the reconstructed position. The white circles mark the positions of the lightning detectors.

Chapter 8

Lightning Data Comparison

After studies of the lightning reconstruction accuracy from simulation this chapter shows the comparison of lightnings detected with the LDS to other lightning detection methods. First analysis were made in Wuppertal and others with the set-up in Argentina and the lightning detection methods described in chapter 6.

8.1 CheckUp-System in Germany

CheckUp-Technik¹ is a German company which writes reports for insurance companies, if there were damages of electric devices. For that purpose they operate a lightning detection network with 14 Boltek StormTracker lightning devices spread over Germany. On their website there was a public event display, which was closed at the beginning of 2013. In a Google map, for example figure 8.1, the detected lightnings for a chosen distance and time period were plotted. By downloading the provided kml-file it is possible to read out the position and time of the detected lightnings. These were compared to the events measured in a test set-up in Wuppertal on single detector base. For the comparison a radius of 1500 km around the university was used to get the CheckUp data.

The test measurements were done with three StormTracker mounted at the university and without the GPS-extension, described in section 6.2.4, which was developed later.

¹<http://www.checkup-technik.de>

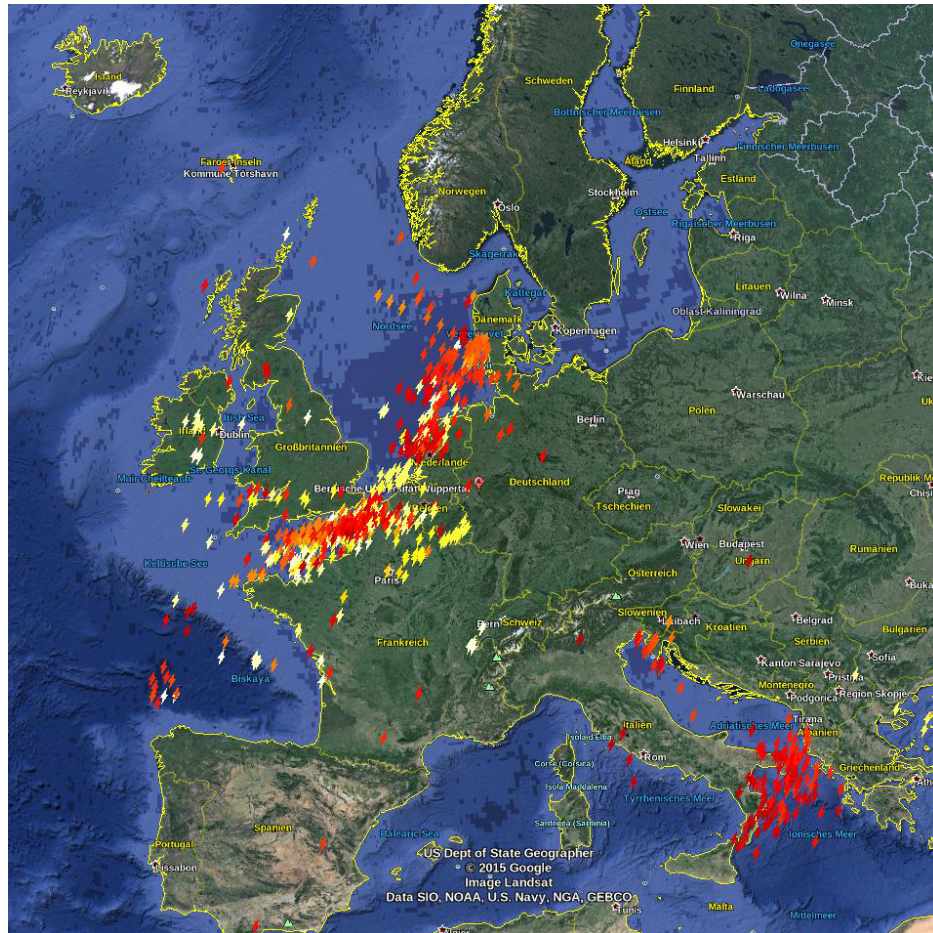


Figure 8.1: Map of CheckUp Events around the university of Wuppertal as center for the period of 01.11.2012 00:00:00 - 02.11.2012 09:00:00 UTC. The provided Google Earth map [134] with colour code for the timing.

8.1.1 Number of Triggers

First studies were made comparing the number of triggers, on the one hand the absolute number and on the other hand in dependence of the distance to the lightning. One can see in figure 8.2 that ca. 95 % of the events found with the CheckUp system trigger at least one detector in Wuppertal. Less than 20% of the coincidences with the CheckUp system trigger only one or two stations. Using only coincidences of three stations would lead in a reduction of a factor ~ 2 in the huge number of the triggered events not detected by the CheckUp system which could be noise. The university creates a lot of noise, for example by switching on the neon tubes in the near by offices, but the

8.1. CHECKUP-SYSTEM IN GERMANY

events could also be real lightnings which are out of the range used for the CheckUp system data. In the later set-up in Argentina the distance between all stations (~ 40 km) is much larger as in Wuppertal, where the antennas are very near to each other (~ 10 m) which should reduce the number of coincident noise peaks in time. Figure 8.3 shows, that in the region up to ~ 1000 km almost every lightning detected by the CheckUp system was also detected in Wuppertal. One has to keep in mind that the detection device is the same.

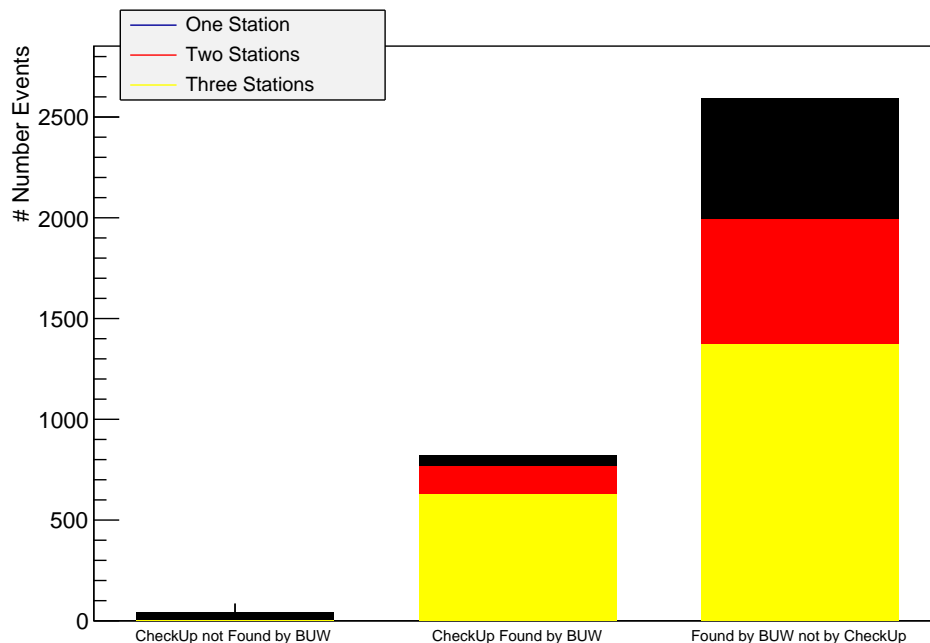


Figure 8.2: This plot shows the number of triggered events of the 01.11.2012 00:00:00 - 02.11.2012 09:00:00 UTC. The left bar shows the number of lightnings detected by the CheckUp system, but not by any device in Wuppertal. The center bar shows the number of lightnings detected by the CheckUp system and by the devices in Wuppertal. In black are the number of events seen by one detector, in red by two detectors and in yellow by all three detectors in Wuppertal. The right bar shows the number of lightnings detected by devices in Wuppertal, but not by the CheckUp system. The color coding is the same as for the center bar.

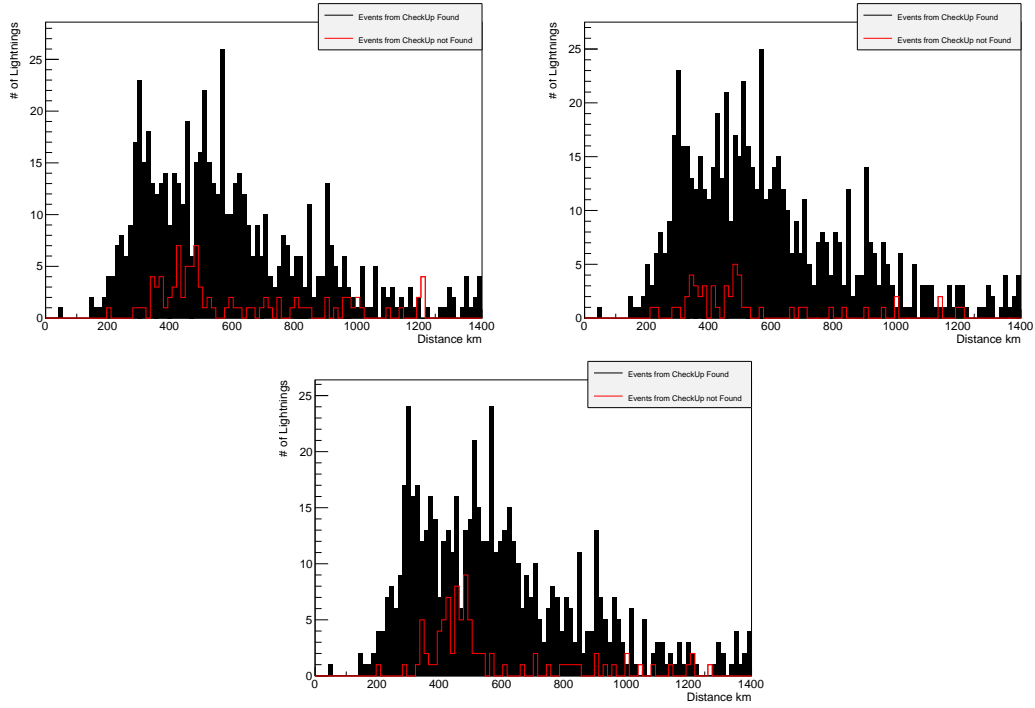


Figure 8.3: In black is shown the number of events triggered in Wuppertal and by the CheckUp system for the 01.11.2012 00:00:00 - 02.11.2012 09:00:00 UTC in dependence of the distance in km for each of the three detectors. In red the events which were triggered by the CheckUp system but not by the devices in Wuppertal are plotted.

8.1.2 Direction

The LDS provides a calculated direction for each lightning detected. This direction can be compared to the real direction calculated from the position of the lightning in the CheckUp system with respect to the position of the detectors in Wuppertal. Figure 8.5 shows the deviations of the directions given by both systems. One can see an agreement of $\sim 20^\circ$. The mean value is not zero, which could be due to a systematic shift, if the antenna was not facing directly to north. In figure 8.4 the position of lightnings detected by both systems are shown. The events from west show a good agreement in the direction, but for the events from south-east there is a deviation, these events are detected from east by the LDS and are visible in figure 8.5 as the second bump.

The calculation of the direction takes only the maximum amplitude of both polarizations and a measured E-field value (0 or 1) into account. Attempts

8.1. CHECKUP-SYSTEM IN GERMANY

to increase the accuracy of the direction by fitting the trace did not show a significant improvement.

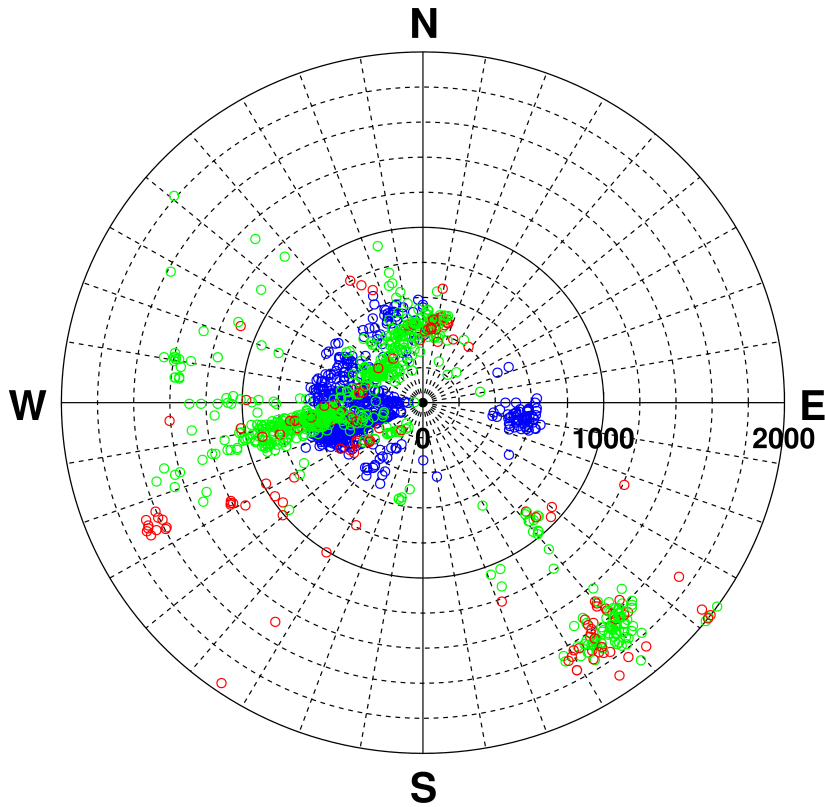


Figure 8.4: Polar plot of the calculated positions of the CheckUp system events around the university of Wuppertal as center for the period of 01.11.2012 00:00:00 - 02.11.2012 09:00:00 UTC. The radius of the events shows the distance in km in a range of 2000 km. The events detected with the LDS in Wuppertal are marked in green, the not detected ones in red. The blue markers are the positions found by one of the LDS.

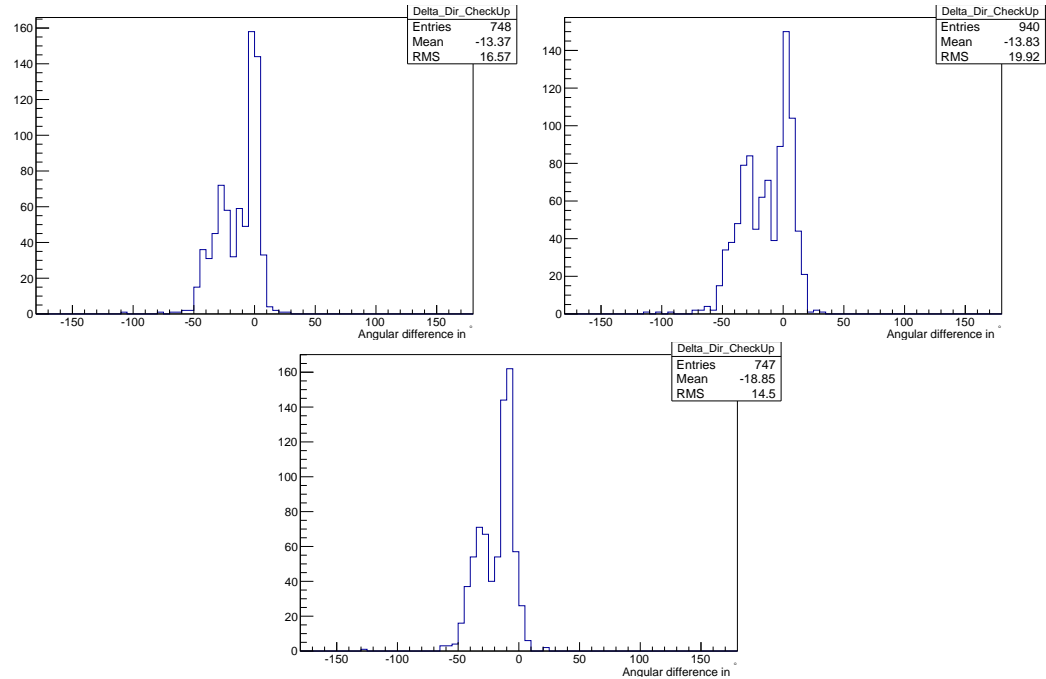


Figure 8.5: Angular difference in degree of the detected lightnings by the CheckUp system and the LDS in Wuppertal.

8.1.3 Distance

The accuracy of the estimated distance of the lightning on single LDS station level is not sufficient for the set-up in Argentina. Figure 8.6 shows, that even the averaged distance has an uncertainty of more than 100 km compared to the distance of the CheckUp events.

8.1.4 Cable Length

The StormTracker PCI Card is connected to the antenna via a Cat 5 cable. The length of the delivered cable is ~ 15 m which is not long enough for the set-up at Malargüe Campus. For that reason a longer cable with 30 m is used there. First tests in Wuppertal have shown a roughly estimated reduction of the number of triggers of a factor ~ 2 . But during the period with the changed cable there were only a very few lightnings. The limited statics does not allow a precise estimation of a possible reduction factor.

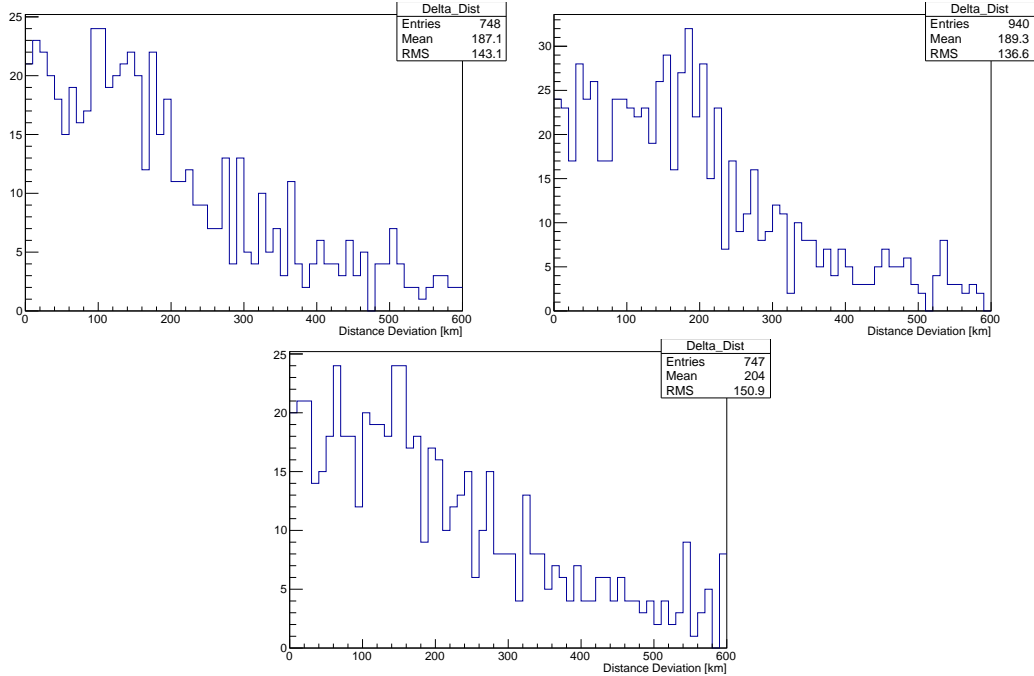


Figure 8.6: Difference of the detected average distance with the LDS to the distance of the position found by the CheckUp system.

8.2 SD Lightning Flag

This section presents the comparison of the LDS to the SD lightning flag. Shown are comparisons of the absolute time, the rate of events taking the uptime into account and the position of the lightnings.

8.2.1 Timing

The first analysis is the comparison of the timing of lightnings detected with both systems to reduce the time window for coincident lightnings as much as possible to reduce random coincidences. To estimate a possible timing offset a large time window of 2.5 ms was used to find lightnings detected with both systems. Taking the position from the SD lightning flag stations into account the runtime of the signal to the lightning detection station is calculated. The runtime is added to the SD time stamp. This can be directly compared to the time stamp of each lightning detection station by calculating the time offset of each lightning. For the runtime corrected time stamps a smaller coincidence window of $250 \mu\text{s}$ is used to select the final events. The same can

be done not only for the position of each lightning detector, but also for the position of the reconstructed lightning. Figure 8.7 shows the runtime corrected time offset of lightnings detected with the lightning detection stations and the SD lightning flags by subtracting the SD time stamp of the GPS time stamp. The results are summarized in table 8.1.

| Detector | Time offset to SD [μs] | Standard deviation [μs] |
|--------------------------|-------------------------------------|--------------------------------------|
| Malargüe ² | $-139.6 \pm 0,7$ | 7.6 ± 0.9 |
| Los Leones ² | -141.1 ± 1.3 | 8.8 ± 1.4 |
| Coihueco ² | -140.9 ± 1.3 | 7.9 ± 1.3 |
| Los Morados ² | $-141.8 \pm 2,3$ | 8.1 ± 1.9 |
| Reconstructed | -135.6 ± 2.0 | 9.1 ± 1.9 |

Table 8.1: Time offset of the GPS time stamps of each lightning detection station with respect to the time stamp of the SD lightning flag. The values are obtained from the Gaussian fits in figure 8.7.

The lightnings are detected with the lightning detection stations about $141 \pm 1 \mu\text{s}$ earlier than the SD lightning flag is set. The standard deviation is about $8.1 \pm 0.5 \mu\text{s}$ which corresponds to a distance of 2.4 km, which is compatible to the precision which can be achieved with the SD lightning flags.

²removed trigger delay of $32.59 \mu\text{s}$

8.2. SD LIGHTNING FLAG

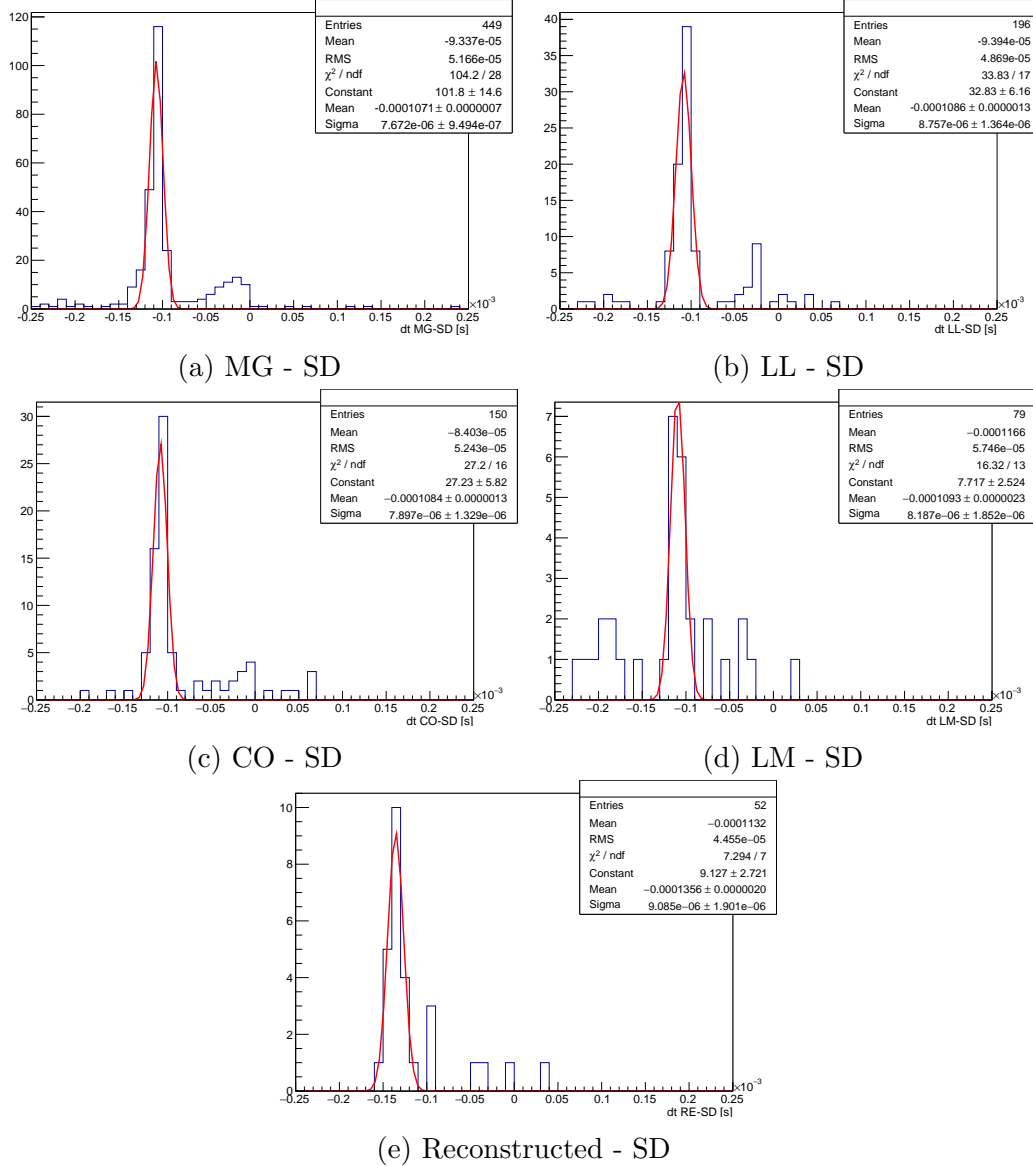


Figure 8.7: Runtime corrected time offset of lightnings detected with the lightning detection stations and the SD lightning flags calculated by subtracting the SD time stamp of the GPS time stamp. Negative values imply that the lightning detection stations measure the lightning earlier than the SD lightning flag.

8.2.2 Reconstruction Position

After comparing the timing of both lightning detection methods the reconstructed positions will be compared in this paragraph.

In section 6.3 and 6.5 the evaluation of the lightning position was described. Applying this to the data of 2014 results in an event map Fig. 8.8. For this analysis for each SD lightning event the mean easting and northing of the SD stations with lightning flag is calculated as position of the lightning. The largest distance of one lightning flagged station to the lightning position is taken as radius for each event. Most lightnings get reconstructed within this radius. Two lightnings are big outliers which get reconstructed out of the SD array. Further analysis leads to the histogram of the deviation of the position evaluated with both lightning detection methods, figure 8.9. A Landau fit results in a most probable value of ~ 1.5 km, which is the same as the spacing between the SD stations.

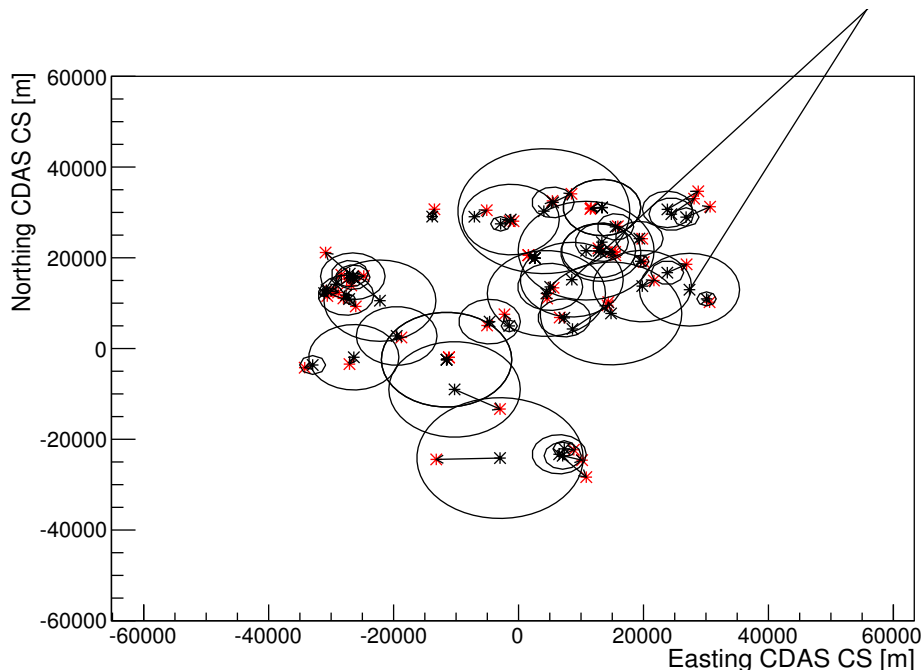


Figure 8.8: Map of Events with SD lightning triggers and also reconstructed by the lightning detection system for 2014. The black marks indicate the calculated position of the SD lightning and the circle around shows the radius of the triggered SD Stations. The arrows point to the reconstructed position with the lightning detection system, marked with a red marker.

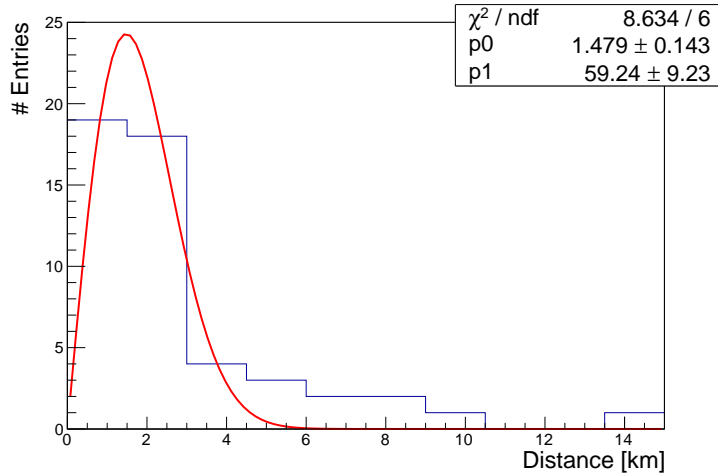


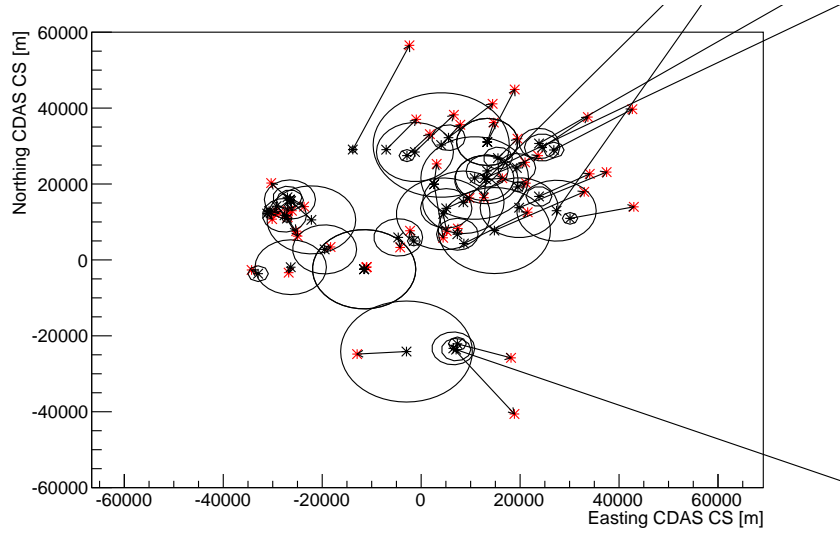
Figure 8.9: The distance of the calculated position of lightning flag to the reconstructed position estimated by the lightning detection system from figure 8.8 shown in a histogram. Each bin on the x-axis is 1.5 km. In red a landau fit is plotted.

Comparing figures 8.9 and 8.10 shows the improvement of the reconstruction accuracy by shifting the traces over each other with the cross correlation method described in section 6.3. Without the correction of each time stamp the quality of the reconstruction drops significantly from a most probable value of the landau fit of ~ 1.5 km to ~ 5 km.

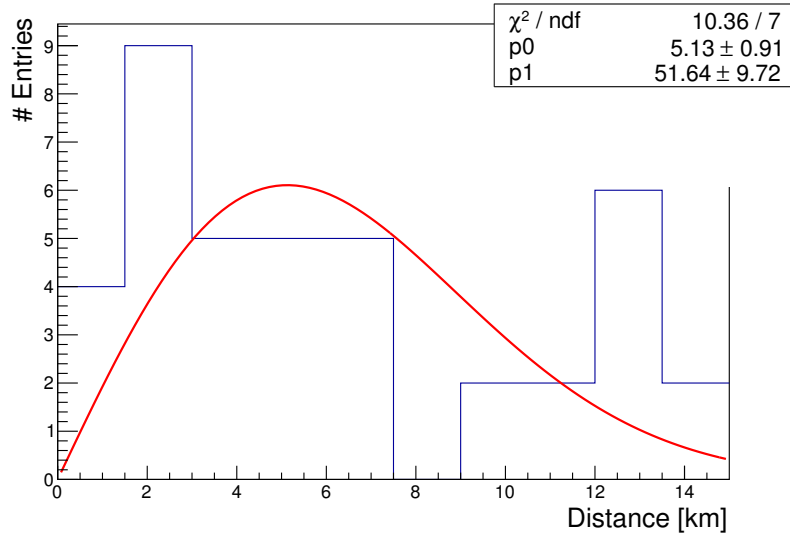
8.2.3 Uptime and Detection Rate

The amount of reconstructed events measured by the lightning detection system and flagged as SD lightning is small. Only 52 of 1657 SD lightnings have been reconstructed. One reason is, that only for 554 events at least three lightning stations were taking data. From these 554 events 77 triggered at least three lightning stations. Surprisingly the Malargüe station has the highest detection rate of coincident events although the total rate of the detector is the lowest in comparison to the other stations.

The uptime at only 1/3 of the lightning detection stations for the SD lightning events in 2014 shows, that an improvement was necessary. Especially if there were lightnings near by, with a high detection rate, the detectors hung up. Mostly due to communication problems with the GPS device and a manual restart of the program was needed. This is solved by running a monitoring script which restarts the lightning detection program on each PC if it gets stuck.



(a) Event Map



(b) Histogram

Figure 8.10: Figure (a) shows an event map of SD lightning triggers and also reconstructed by the lightning detection system without shifting the traces for 2014. The black marks indicates the calculated position of the SD lightning and the circle around it shows the radius of the triggered SD Stations. The arrows point to the reconstructed position with the lightning detection system, marked with a red marker. The distance of the calculated position of lightning flag to the reconstructed position estimated by the lightning detection are plotted in histogram (b). In red a landau fit is drawn.

8.3 World Wide Lightning Location Network

After the data comparison to the SD lightning flag this section describes the comparison to another lightning detection system. *The World Wide Lightning Location Network*(WWLLN), with currently more than 50 sensors [135] around the globe detects spherical activity in the VLF band and provides a realtime location of cloud to ground lightning strikes [136]. The originally determined accuracy of 30 km [101] has been improved to 10 km for regions with a higher density of sensors.

For a validation of the lightning detection system at the Pierre Auger Observatory the WWLLN data of October 2014 within a radius of 1000 km around the center of the SD array have been provided by the WWLLN.

For the time period of the given WWLLN sample in October 2014 four lightning detectors were deployed. The following analysis is performed on lightnings detected by all available lightning detectors and the WWLLN.

8.3.1 Timing

The GPS time stamps of the LDS data were earlier than the SD lightning flag. With the WWLLN data available, it allows to study, if this is a systematic effect of the lightning detection. For that purpose again the time offset of the events detected with the lightning detection system and the WWLLN were calculated and filled into a histogram, figure 8.11. To obtain a mean value and a sigma of the curve a Gaussian is fitted. The data of each station is corrected for the trigger delay of the StormTracker ($32.59 \mu\text{s}$).

| Detector | Time offset to WWLLN [μs] | Standard deviation [μs] |
|---------------|----------------------------------------|--------------------------------------|
| Malargüe | 17.78 ± 0.52 | 24.87 ± 0.63 |
| Los Leones | 19.58 ± 0.56 | 28.91 ± 0.65 |
| Coihueco | 25.88 ± 0.69 | 33.36 ± 0.70 |
| Los Morados | 20.67 ± 0.51 | 28.86 ± 0.59 |
| Reconstructed | 23.55 ± 2.10 | 25.45 ± 1.99 |

Table 8.2: Time offset of the GPS time stamps of each lightning detection station with respect to the time stamp of the WWLLN event. The values are obtained from the Gaussian fits in figure 8.11.

The WWLLN time stamps are about $21.0 \pm 3.5 \mu\text{s}$ earlier than the time stamps of the LDS. Within the uncertainty of position of the lightnings ($10 \text{ km} \hat{=} 33.4 \mu\text{s}$) and within the width of the distribution they are compati-

CHAPTER 8. LIGHTNING DATA COMPARISON

ble. The large systematic offset of about $100 \mu\text{s}$ measured with respect to the SD lightning flag cannot be confirmed with the WWLLN data. The small measured offset with respect to the WWLLN is in the opposite direction of time. Since the width of the Gaussian fit is smaller than $33.4 \mu\text{s}$ the position accuracy is slightly better than 10 km.

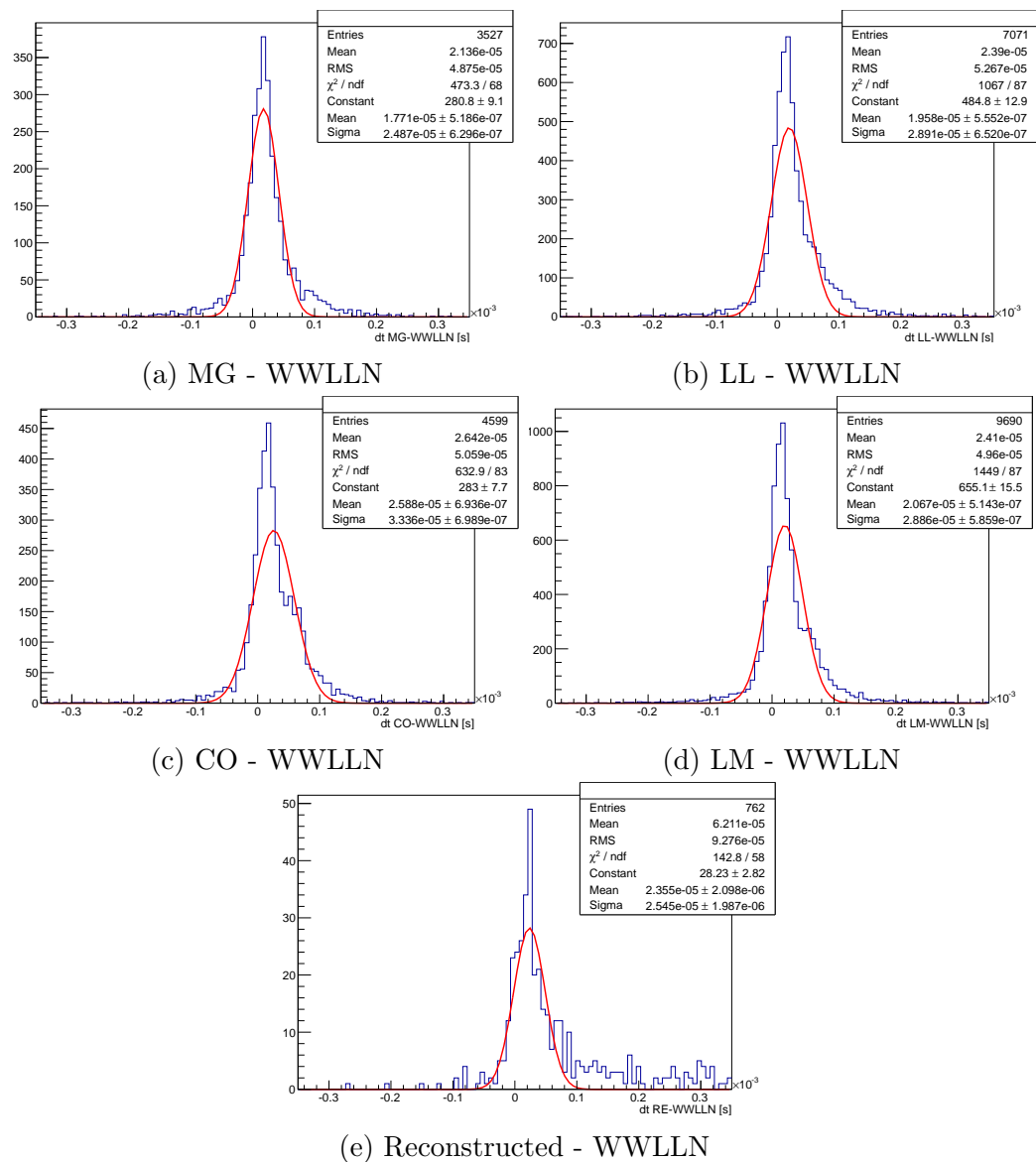


Figure 8.11: Runtime corrected time offset of lightnings detected with the lightning detection stations and the WWLLN. Calculated by subtracting the WWLLN time stamp of the GPS time stamp. In red a Gaussian is fitted.

8.3. WORLD WIDE LIGHTNING LOCATION NETWORK

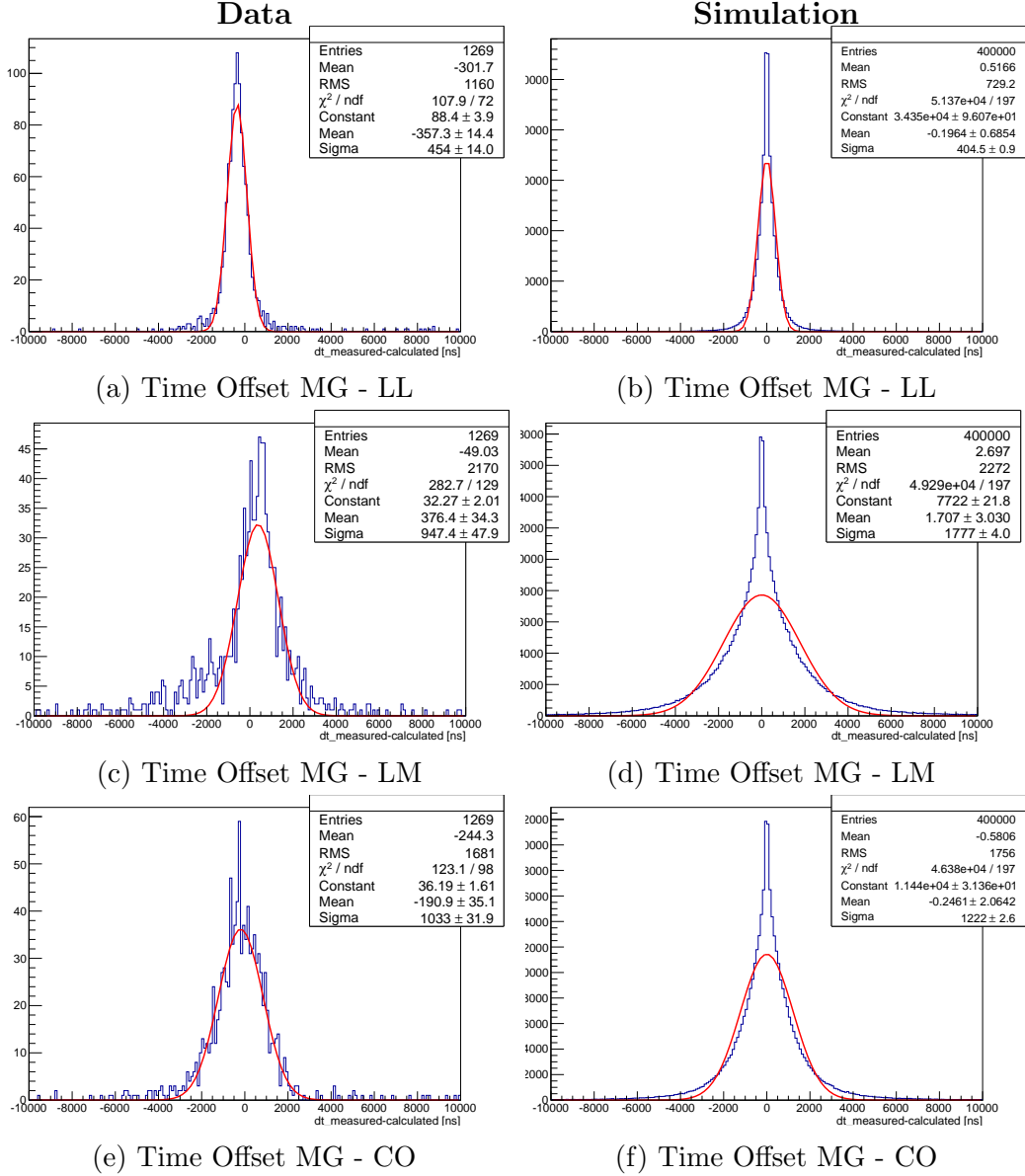


Figure 8.12: Runtime corrected time offset of lightning detection stations to each other, for events detected with the lightning detection stations and the WWLLN on the left and for simulation, using an uncertainty in the position of 5 km on the right. In red a Gaussian is fitted.

For the reconstruction of the lightning position the relative accuracy of the lightning detectors to each other is important. To reduce systematic uncertainties in the comparison of WWLLN and detector data the time offset of

each lightning detection station to the Malargüe station for coincident events with the WWLLN is shown in figure 8.12, while the runtime to the detected WWLLN position is taken into account. For comparison the time offset was also simulated with an uncertainty of 5 km in the position.

The data shows a systematic offset of the mean timing, which is not seen in the simulation. This could be a hint, that the WWLLN events are shifted to one direction. The sigma of the distributions is compatible, which indicates on the one hand that 5 km is a reasonable uncertainty for the WWLLN positions and on the other hand that the timing accuracy of each station is compatible with the simulations.

8.3.2 Uptime and Detection Efficiency

In this paragraph the uptime and the detection rate of the lightning detection stations will be investigated.

Section 8.2.3 has shown, that the uptime especially of Coihueco has some gaps. Mainly if there are lightnings with a high detection rate the detectors get out of order, figure 8.14. As already mentioned this is solved now by running a monitoring program which restarts the lightning detection software, if it stops working.

Comparing the detection rates one can see, that for times with a high number of WWLLN events the detection rate of the lightning detection stations is also increased, but the absolute numbers do not match at all, which is related to the detection efficiency of both systems and the radius of events taken into account. The correlation factors are shown in table 8.3.

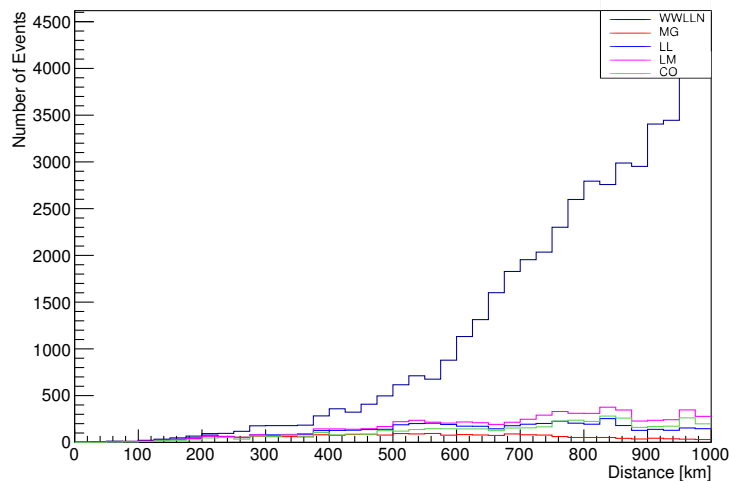
| Lightning Detection Station | Correlation Factor within 500 km | Correlation Factor within 1000 km |
|------------------------------------|-----------------------------------------|------------------------------------------|
| Malargüe | 0.64 | 0.31 |
| Los Leones | 0.71 | 0.46 |
| Los Morados | 0.74 | 0.39 |
| Coihueco | 0.20 | 0.53 |

Table 8.3: For the number of WWLLN events per hour in a range of 500 km and 1000 km the correlation factor to the number of events at each lightning detection station is shown. The uptime of the detectors is considered.

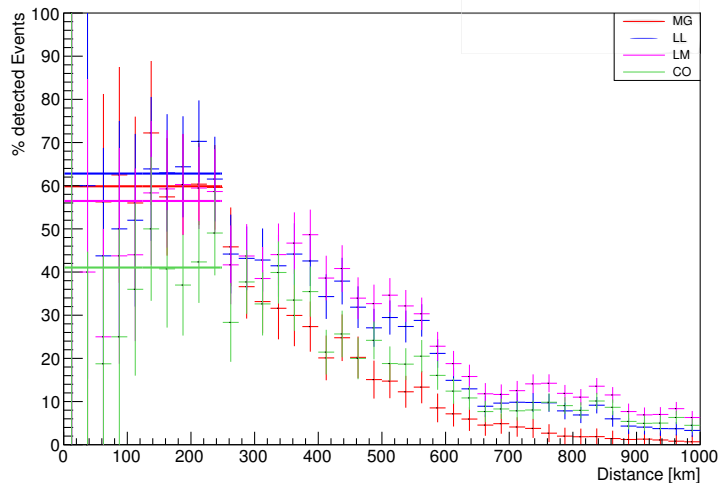
For MG, LL and LM there is a clear correlation in the detection rates within 500 km. For Coihueco the correlation factor with 0.20 is very low. For the data in a range of 1000 km the correlation factor of CO increases to 0.53

8.3. WORLD WIDE LIGHTNING LOCATION NETWORK

while for the other detectors the factor decreases. Especially MG has a low correlation factor of 0.31. This shows, that CO detects events further away than the other detectors while MG detects them only near by, which could be an effect of the longer cat-5 cable used for the connection of the Boltek PCI card to the antenna.

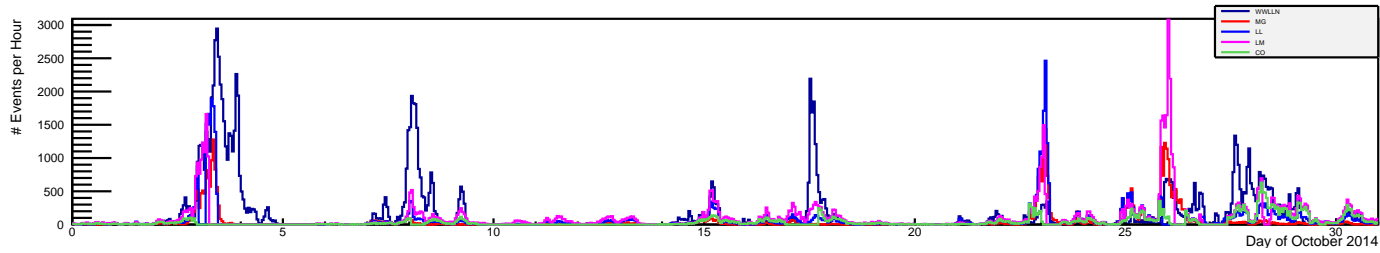


(a) Number of detected WWLLN events.

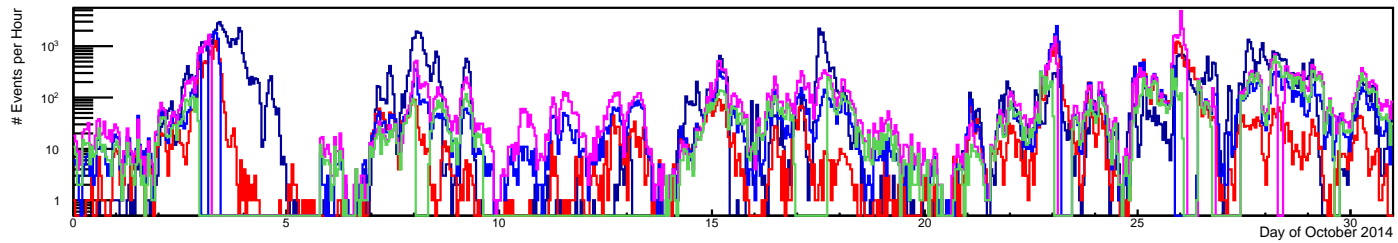


(b) Fraction of detected WWLLN events.

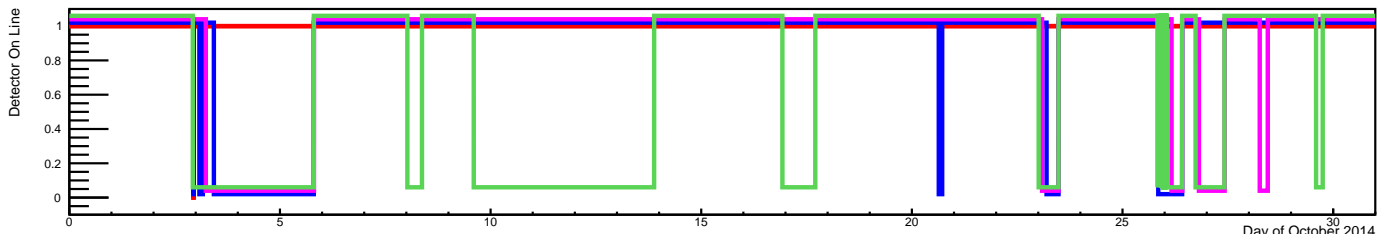
Figure 8.13: Number of detected WWLLN events during the uptime of all stations against the distance of the WWLLN event (a). Figure (b) shows the fraction of the detected WWLLN events and the events detected by each station.



(a) Number of detected events per hour in October 2014



(b) Number of detected events per hour in October 2014 on a logarithmic y axis.



(c) Uptime of the lightning detection stations in October 2014 (1 = available, 0 = out of order).

Figure 8.14: Figure (a) shows the number of detected events per hour of the lightning detection stations in Malargüe in red, Los Leones in blue, Los Morados in purple, Coihueco in green and the WWLLN rate in dark blue for October 2014. In figure (c) the detector availability is plotted (1 = available, 0 = out of order).

8.3. WORLD WIDE LIGHTNING LOCATION NETWORK

For the calculation of the detection efficiency one has to take only the periods into account where each lightning detector was taking data. Figure 8.13a shows the total number of WWLLN events, within the uptime of all lightning detection stations, and the in coincidence detected events at each station against the distance of the WWLLN event. The number of the detected events per station seems to be nearly stable with a small decrease, but the number of WWLLN events grows due to the geometry. Only the Malargüe station has a huge reduction of the number of detected lightnings with the distance. Figure 8.13b shows the fraction of the WWLLN events and the coincident detected events with each station. Within 250 km distance the efficiency for Malargüe, Los Leones and Los Morados is about 60% and drops then for lightnings further away. Coihueco has a significant lower detection fraction for the nearby lightnings of about 40%. The exact values are given in table 8.4.

| Detector | Detected WWLLN Events [%] |
|-------------|---------------------------|
| Malargüe | 59.9 ± 4.8 |
| Los Leones | 62.8 ± 4.8 |
| Los Morados | 56.5 ± 4.8 |
| Coihueco | 41.0 ± 4.8 |

Table 8.4: Fraction of detected WWLLN events within 250 km during the uptime of each station. The values are obtained from the fit in figure 8.13b

To validate the assumption, that Malargüe detects the most events near by and Coihueco the most far away the number of detected events is plotted against the distance of the coincident WWLLN event in figure 8.15. The data can be described by function 8.1. The r^2 part describes the increasing number of events n within the radius r of the detection area and the e^{-r} part the loss of detection efficiency. p_1 is the distance of the most detected coincident events.

$$\text{Fit Function:} \quad n(r) = \frac{r^2}{p_0} \cdot e^{-\frac{2r}{p_1}} \quad (8.1)$$

The results are summarized in table 8.5. One can see, that the assumption is confirmed. The station in Malargüe detects more events nearby, while in Los Leones and in Los Morados they are detected at compatible distances and in Coihueco the events are detected almost two times further away. Since the set-up for all stations is the same except the longer cat-5 cable in Malargüe this is a unexpected result.

CHAPTER 8. LIGHTNING DATA COMPARISON

| Detector | Distance [km] |
|-------------|-----------------|
| Malargüe | 268.1 ± 1.9 |
| Los Leones | 468.3 ± 4.9 |
| Los Morados | 590.7 ± 7.9 |
| Coihueco | 1185 ± 54 |

Table 8.5: Distance with the most detected coincident WWLLN events of the different detectors. The values are obtained from the fit in figure 8.15.

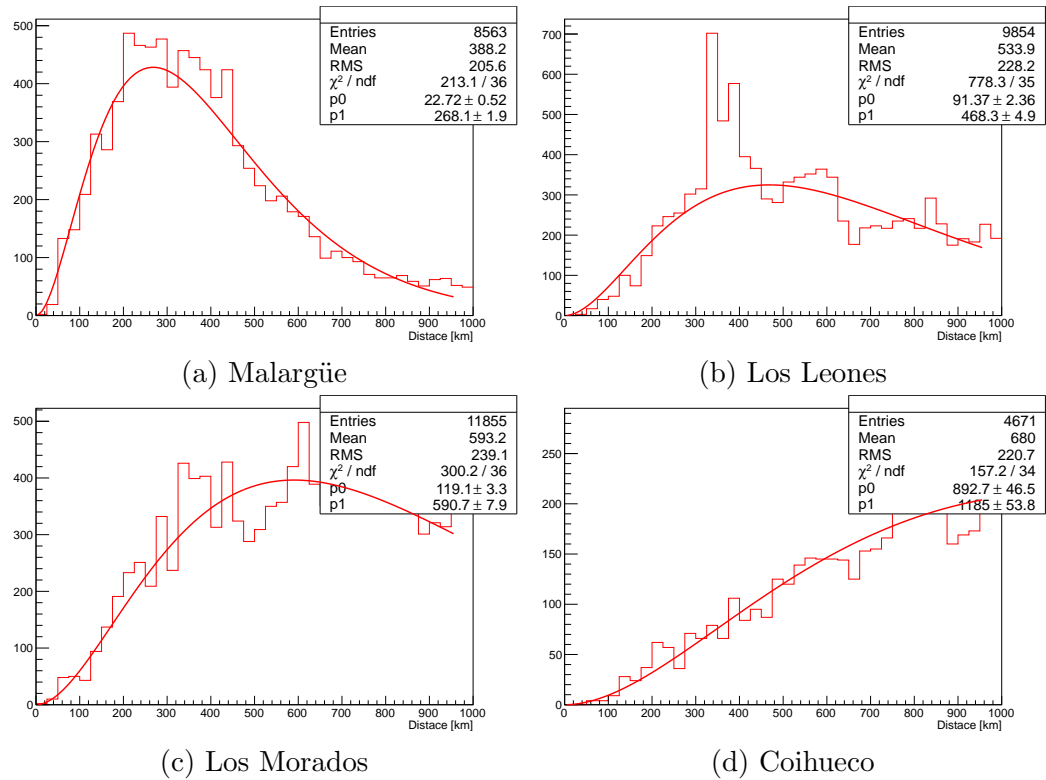


Figure 8.15: Number of detected WWLLN events against their distance for each detector. Additionally, the fit of equation 8.1 is plotted.

8.3. WORLD WIDE LIGHTNING LOCATION NETWORK

So far systematic effects due to the distance have been discussed. Now directional effects are studied. For that purpose the number of WWLLN events and the number of detected events per station are plotted against their direction in figure 8.16. The direction is calculated in the CDAS coordinate system. The cartesian position uncertainty leads to a small directional uncertainty of 2° for large distances as 500 km, for events in a distance of 100 km about 8.5° . The distribution of the WWLLN events in the azimuth angle ϕ is not a flat distribution, there is an excess in the data between -100° and -80° and another between -50° and 110° . A map of the WWLLN events is shown in figure 8.17.

Due to geometrical effects of the antenna polarization and the peak over threshold trigger on the two polarization channel separately a lower trigger efficiency for events at the inter cardinal directions is expected in comparison to the cardinal directions. The signal height should be reduced to $1/\sqrt{2}$, assuming a cosine for the direction dependence, for each polarization. In figure 8.16b one can see the expected behaviour, especially in the region with enough statistical data from about -100° to 100° , but the curves, except Los Morados, are shifted about $\sim 25^\circ$ to positive values.

The efficiency in dependence of the azimuth angle $\varepsilon(\phi)$ is fitted to figure 8.16b with the following function, where E is the maximum efficiency and $\Delta\phi$ a directional offset in the azimuth:

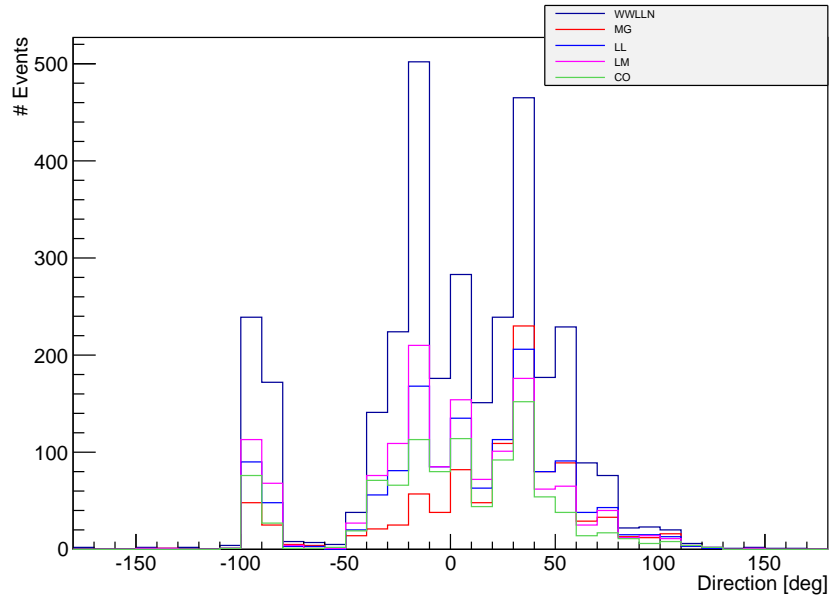
$$\varepsilon(\phi) = E \cdot \max(|\cos(\phi + \Delta\phi)|, |\cos(\phi + \Delta\phi + 90)|). \quad (8.2)$$

The results are given in table 8.6:

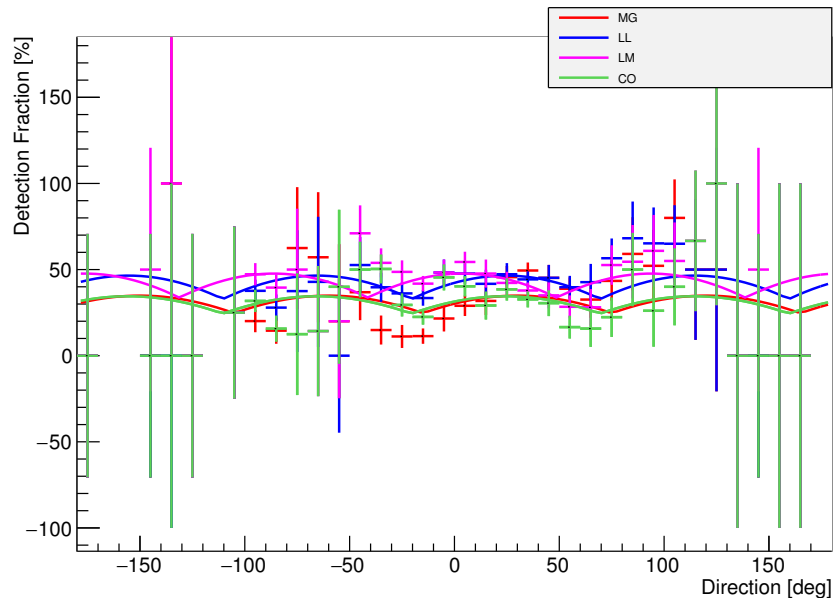
| Detector | Maximum Efficiency [%] | Directional Offset [deg] | chi ² /ndf |
|-------------|------------------------|--------------------------|-----------------------|
| Malargüe | 34.9±2.0 | -30.0±0.1 | 56.9/30 |
| Los Leones | 46.5±2.0 | -24.6±4.8 | 17.5/30 |
| Los Morados | 47.7±1.9 | -3.8±5.1 | 21.5/30 |
| Coihueco | 34.5±2.0 | -24.4±6.5 | 29.4/30 |

Table 8.6: Results of the fit in figure 8.16b.

The chosen model for the description of the angular dependence leads to a significant amplitude. The phase is surprisingly, but during the installation of the antennas has not been much effort to align them very well to north, as for the time of arrival reconstruction only the timing is taken into account.



(a) Number of detected WWLLN events.



(b) Fraction of detected WWLLN events.

Figure 8.16: Number of detected WWLLN events during the uptime of all stations within 500 km against the direction of the WWLLN event for the different stations (a). (b) shows the fraction of the detected WWLLN events by each station. Additionally function 8.2 is fitted for each detector.

8.3.3 Reconstruction Position

After investigating the efficiency with respect to the direction and distance, in the next section the position reconstruction will be compared to the position of the WWLLN data. Figure 8.17 shows the position of the detected WWLLN events in October 2014 within a radius of 1000 km around the center of the CDAS coordinate system.

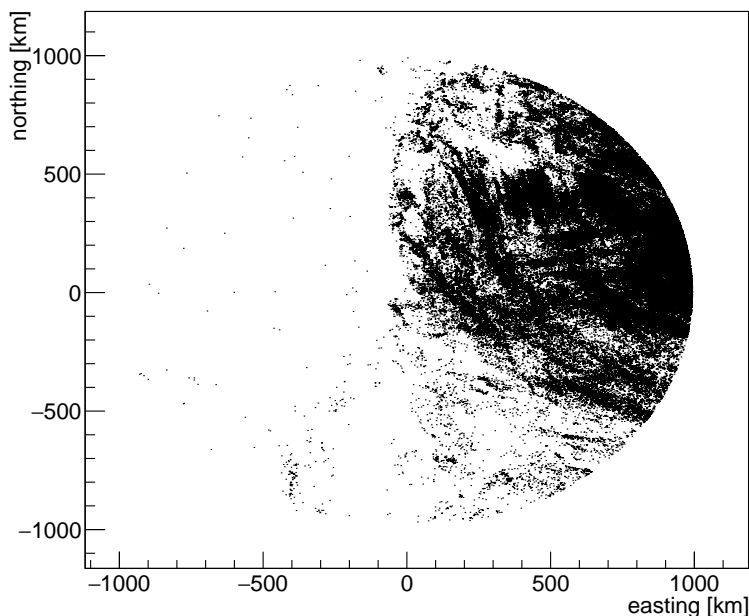


Figure 8.17: Map of WWLLN Lightning Strikes for October 2014. The black points mark the WWLLN lightning positions in CDAS coordinate system.

Figure 8.18 shows a map of the coincident WWLLN events and the ground coordinate of the reconstruction with the lightning detection system. Especially the events within ~ 250 km show a good agreement. Lightnings from farther away are sometimes reconstructed as near by. The deviation is mostly in the distance, not in the direction.

For further studies the profiles of the deviation with respect to the direction and distance are shown in figure 8.19. Within 250-300 km distance the deviation is, as expected, smaller than 20 km, which is slightly more than the uncertainty of the WWLLN data. The result is slightly worse than expected from the simulations in section 7, figure 7.3, but one has also to consider, that these simulation were done using five detectors instead of four. The mean directional deviation with $1.7 \pm 0.1^\circ$ is larger than 0.06° found in the simulation. This could be expected due to the uncertainty of the WWLLN

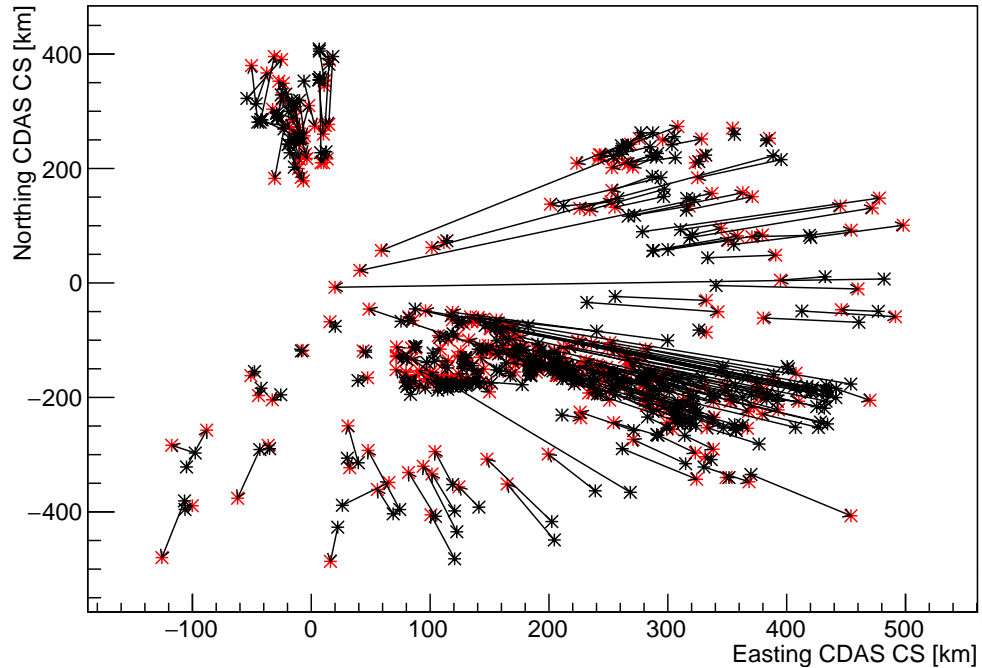


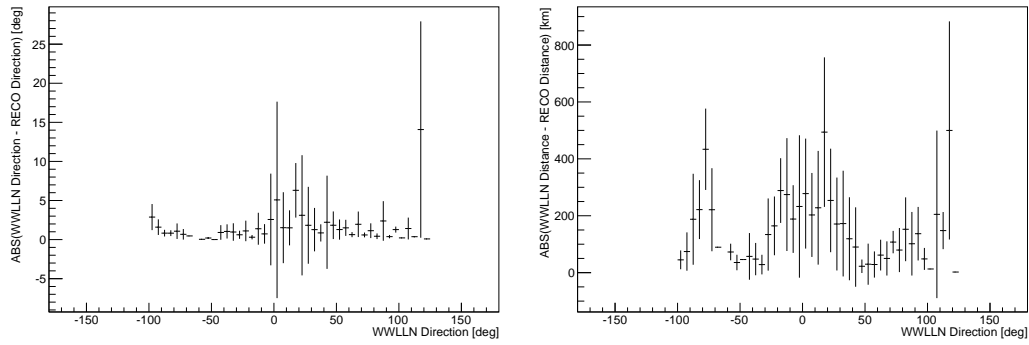
Figure 8.18: Map of WWLLN lightning strikes which are reconstructed by the Lightning Detection System for October 2014. The black stars mark the WWLLN lightning positions. The arrows point to the reconstructed positions with the lightning detection system, marked with a red star.

data, as well as less stations are used for reconstruction. The accuracy in the distance is for events on the cardinal directions lower than for the inter cardinal directions, which can be seen in the simulations, too. This is an effect of the detector geometry and the loss of information if the detectors are aligned. For all distances the time offsets are the same for events from that direction.

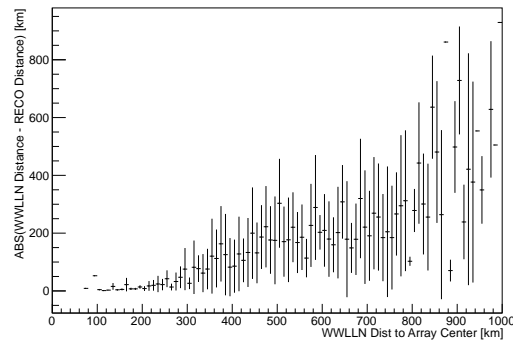
Because of the low statistics of data very nearby one cannot give one unique number for the accuracy within the detector array. But within the radius of 200 km the accuracy is better than ~ 10 km, which is a satisfying number. Taking the uncertainty of the WWLLN data into account, the data for the nearby events are compatible to the simulations. This leads to the assumption that inside the array the reconstruction quality is even better.

The difficulty is to differentiate between lightnings which are nearby and those from further away which are reconstructed to close to the detector array, as seen in figures 6.23 and 7.5. Within the considered period only four stations were deployed. As seen in the simulations using more detectors

8.3. WORLD WIDE LIGHTNING LOCATION NETWORK



(a) deviation between reconstructed and WWLLN direction vs direction (b) deviation between reconstructed and WWLLN distance vs direction



(c) deviation in the distance vs the distance

Figure 8.19: Comparison between the position measured with the lightning detection system and with the one given by the WWLLN for a sample of lightnings in October 2014 (four detectors deployed). The error-bars indicate the spread of the underlying distributions.

reduces the amount of mis-reconstructions. With a larger dataset of events with at least four or better five stations the effect can be studied by removing single stations within the dataset.

8.4 E-Field Mill

The following section describes the comparison of the E-field mill data to the previous mentioned lightning detection techniques. The E-field mills are introduced in section 6.1. In this section also the detection of thunderstorm periods (ISTS) is described.

Within the WWLLN dataset there were no periods marked with the thunderstorm flags (IsTS), which makes it impossible to do any correlation studies on the E-field mills and the WWLLN data.

8.4.1 Comparison of the E-Field Mills to each other

First of all the correlation of the E-field mills to each other is analysed. The field value and the thunderstorm flags (IsTS) will be compared in this paragraph. Since the BLS-station was redeployed as AERAWS a comparison of these two is not possible.

8.4.1.1 E-Field Value

The first analysis compares the signals are at each station. Former analysis have shown, that the detection range of the E-field mills is quite low [137], which should result in a lower correlation of the E-field measured at the CRS and the BLS in comparison to the CRS and the AERAWS, because of the larger distance between them. The distances between CRS and BLS are 21.3 km and between CRS and AERAWS 1.1 km. Figure 8.20 shows the mean E-field over one minute measured at the CRS against the other E-field mills.

| Stations | Correlation Factor |
|--------------|--------------------|
| CRS & BLS | 0.40 |
| CRS & AERAWS | 0.75 |

Table 8.7: Correlation factor of the measured E-field from obtained from figure 8.20.

As expected the correlation between the CRS and the BLS data is quite small, but there is a stronger correlation after the redeployment of the BLS E-field mill as AERAWS to the CRS closer to the CRS.

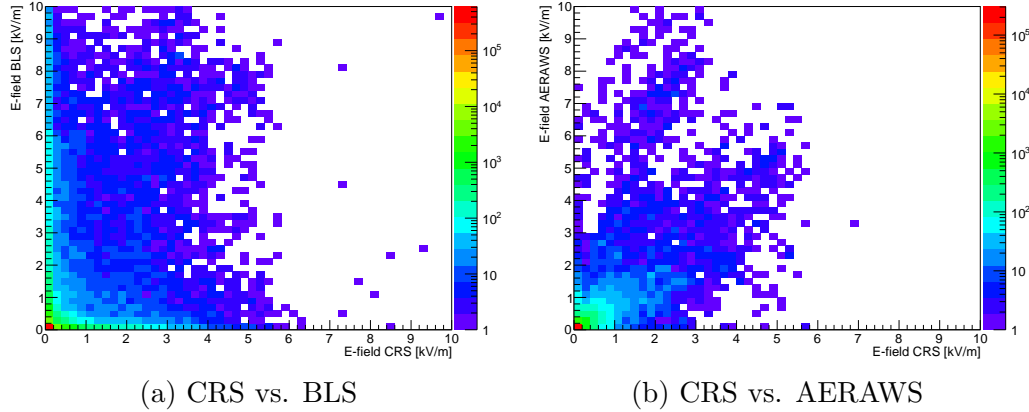


Figure 8.20: The mean E-field of one minute is plotted for the CRS on the x-axis against the BLS (a) respectively the AERAWS (b) on the y-axis. The correlation factors are given in table 8.7.

8.4.1.2 IsTS-Flag Correlation

The different correlation factors of the E-field value result in the question how correlated the thunderstorm flags for the different set-ups are.

For that purpose combined thunderstorm periods were calculated by taking a larger time window of 15 minutes before and after each lightning indication point, in comparison the ISTS-flag, because of the distance between the E-field mills. Overlapping periods in time of one or both stations are combined to one combined thunderstorm period. Within these combined thunderstorm periods one can inspect if both stations had a lightning indication point or only one. In total there were 254 combined thunderstorm periods since 2010 with CRS and BLS and 52 for the set-up with the AERAWS, taking only data into account where both stations were available. One example trace is shown in figure 8.21. The results are given in table 8.8:

| Stations | Total Number | Detected by both | Percentage |
|--------------|--------------|------------------|------------|
| CRS & BLS | 254 | 41 | 16% |
| CRS & AERAWS | 52 | 24 | 46% |

Table 8.8: The table shows the total number of combined thunderstorm periods and the number respectively the fraction of the detected ones by both E-field mills.

Only 16% of the thunderstorm condition periods found by the CRS or BLS

CHAPTER 8. LIGHTNING DATA COMPARISON

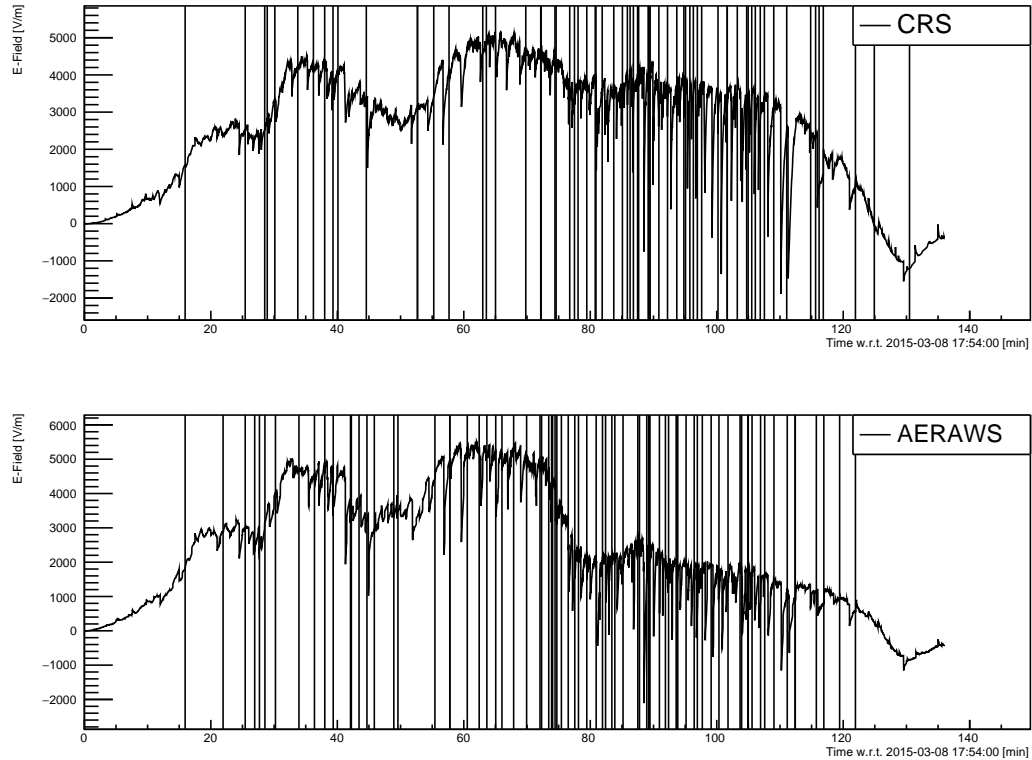


Figure 8.21: E-field [V/m] on the y-axis against the time w.r.t. 03.08.2015 17:54:00 UTC in minutes on the x-axis for one thunderstorm period. On the top for the CRS and on the bottom for the BLS. The vertical black lines mark the lightning indication points.

devices are coincidentally detected. This is a very low fraction, even if the detection range of the E-field mills is low, the size of an average thunderstorm cloud is about 24 km [138]. Even for the set up with both stations near by each other the fraction of coincident periods is only 46%. This leads to the assumption that about 50% of the periods are not related to lightnings, but to noise, for example by cars. These disturbances can lead to single lightning indication points, but real lightnings have typically more than only one lightning discharge. Figure 8.22 shows the number of indication points for each thunderstorm period and differentiates between the ones found by only one station or both.

One can see, that especially the BLS has a huge number of thunderstorm periods with only one lightning indication point, which were not detected at the CRS. But taking these not into account results in a detection fraction for both stations in coincidence of about only 20%. The reason for this low

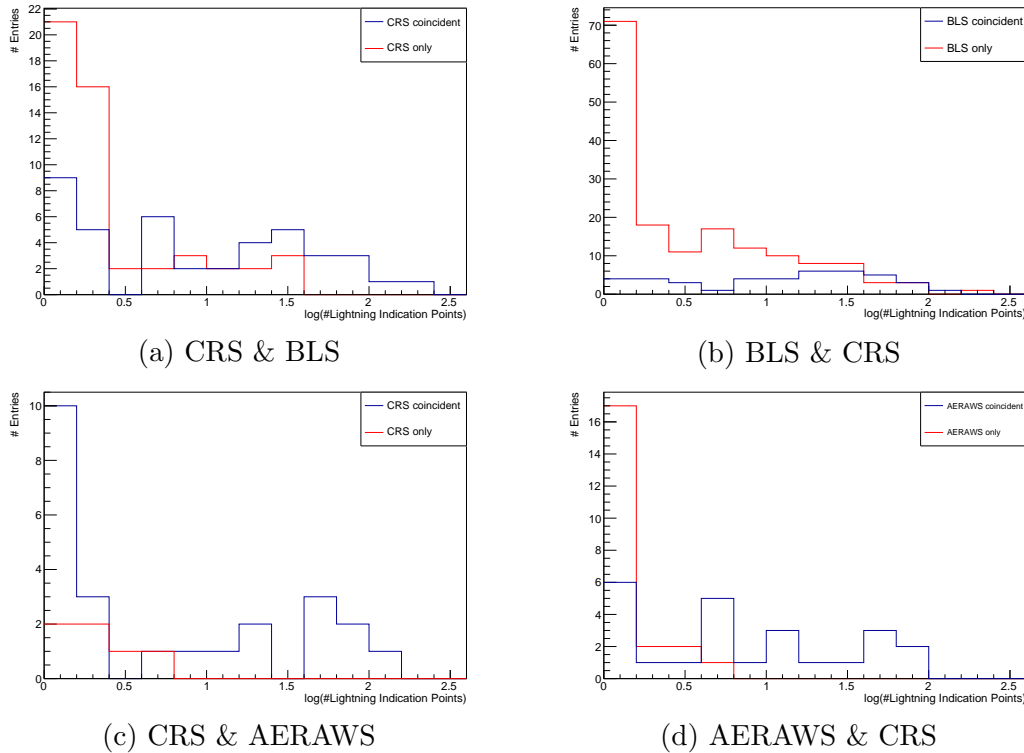


Figure 8.22: For both set ups of the field mills (CRS and BLS on the top (a),(b) and CRS and AERAWS on the bottom (c),(d)) the number of lightning indication points per thunderstorm period is plotted on a logarithmic x-axis against the number of entries on the y-axis. The number of detected periods in both detectors are plotted in black, the ones only detected in one in red.

fraction is the distance of the E-field mills and the smaller local effect of the thunderstorm. For the CRS more periods with only one indication point have BLS events for the same period. Looking to the comparison with the AERAWS, where most coincidences are with only one station, leads to the result, that for the CRS these data can not be neglected. Taking the AERAWS events with only one lightning indication point would lead to a detection fraction of 51%. Summarizing one can say, that this approach achieves an improvement of about 5% in the number of coincidences.

The data of both field mills show a huge deviation with growing distance of each other. The BLS and CRS data are not in a good agreement, but the CRS and AERAWS show a higher correlation. The thunderstorm periods

are mostly detected in only one station, which is not expected, especially for the datasets where the field mills are deployed within a distance of 1.1 km.

8.4.2 Comparison to SD Lighting Flag

This paragraph will describe the comparison to the SD lightning flag. First simply the number of SD lightnings within the combined thunderstorm periods will be calculated. With the lightning position given from the SD lightning flag one can also analyse the range dependence of the field mills.

For the combined thunderstorm periods described in the previous subsection the number of periods with an SD-lightning flag within is calculated for each field mill. The results are given in tabular 8.9:

| Stations with IsTS | #Periods | #with SD | Percentage [%] |
|---------------------------|-----------------|-----------------|-----------------------|
| CRS | 211 | 93 | 44 |
| BLS | 229 | 94 | 41 |
| AERAWS | 38 | 15 | 39 |
| CRS & BLS | 41 | 28 | 68 |
| CRS & AERAWS | 24 | 11 | 45 |

Table 8.9: The tabular shows number of thunderstorm periods for the different E-field mills with an IsTS-flag, and the number / percentage of periods with SD lightnings within.

The fraction of coincident thunderstorm periods of single E-field mills and an SD lightning is about 40%. Taking only the combination of both E-field mills shows for CRS and AERAWS only a small improvement. This can be explained by the poor correlation of the 21 km distant stations (section 8.4.1). But taking CRS and BLS into account results in a correlation of 68% with SD lightnings. Due to the larger distance of both detectors only stronger thunderstorms create an IsTS flag in both E-field mills, which increases of course the probability of SD lightning events.

Only 40% of the thunderstorm periods have a coincidence with SD lightnings. The next step is to calculate the fraction in the other direction. Which is the number of thunderstorm periods during SD lightnings.

Table 8.10 shows the fraction of coincident lightnings, detected by the SD and which here marked as thunderstorm period from the E-field mill. The data for the CRS and AERAWS are in a good agreement, but the fraction

of $\sim 22\%$ is low. The BLS shows a better agreement with the SD Events of 48%. Taking combinations of the two E-field mills into account leads only to an increase of the statistics, but not in the number of coincidences.

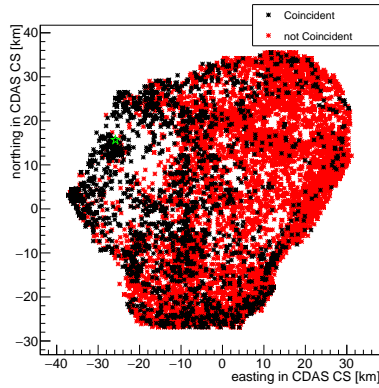
| E-field mill | #SD Lightnings | #IsTS | Percentage [%] |
|---------------------|-----------------------|--------------|-----------------------|
| CRS | 8325 | 1772 | 21 |
| BLS | 6970 | 3357 | 48 |
| AERAWS | 1778 | 287 | 24 |
| CRS or BLS | 7734 | 3692 | 47 |
| CRS or AERAWS | 2534 | 547 | 22 |

Table 8.10: The tabular shows number of SD lightnings, and the number / percentage of periods with an lightning for the different E-field mills.

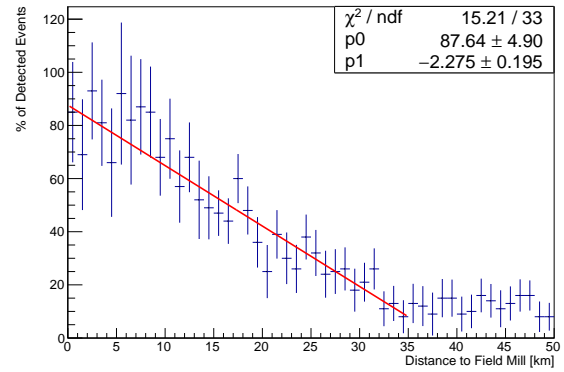
For that analysis all SD lightning events were taken into account. But it was shown, that the range of the detection of the E-field mills is small. So it is no surprise, that the detection efficiency related to the whole SD array is low. Figure 8.23 shows the position of the SD lightnings and differentiates between the ones which have an IsTS-flag and the ones without. Additionally the fraction of the detected lightnings with both systems with respect to the distance to the field mills is shown. The field mill CRS and AERAWS show a compatible behaviour within the errors. The maximum detection efficiency with respect to the SD lightning flag is 87% and drops with a loss in the efficiency with the distance of 2.3% per km. Above 35 km the efficiency is constant at 10%. The BLS shows a difference in the behaviour and seems to be more sensitive. The maximum efficiency is 100% and the loss with the distance is only 1.7% per km. The BLS shows also for large distances a constant detection fraction which is with 20% after 41 km higher than for the other field mills. The flat tale of the distributions is due to random coincidences with a fraction of $12.0 \pm 1.5\%$ for the CRS and $11.3 \pm 1.5\%$ for the AERAWS. For the BLS the fraction of random coincidences with $19.9 \pm 3.4\%$ is slightly larger. Due to the wider distribution there is a larger overlap between real events and the random coincidences.

The measured field strength for each SD lightning at each field mill is plotted in figure 8.24. As one expects the field strength drops with the distance, but taking the large error bars of the profile plot into account one can see, that the deviations for each distance are huge. The field strength at the BLS is significantly higher than for the other devices, what justifies the assumption that the BLS measurements are bias due to the mounting or the ground characteristics.

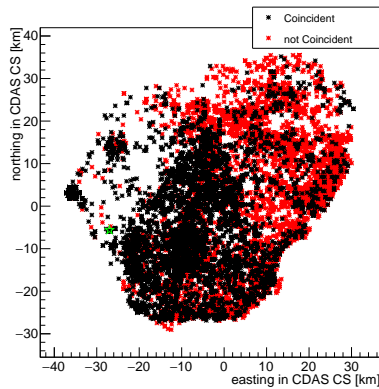
CHAPTER 8. LIGHTNING DATA COMPARISON



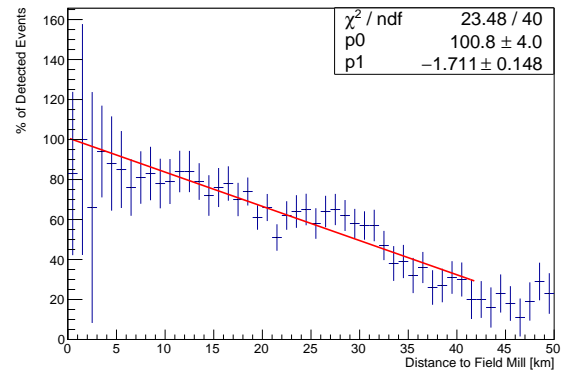
(a) CRS Map



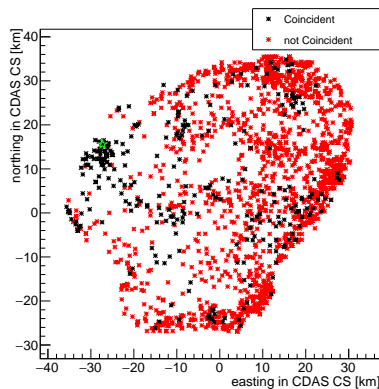
(b) CRS Detection Fraction



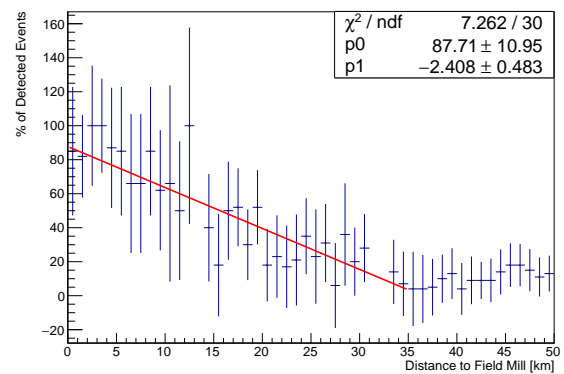
(c) BLS Map



(d) BLS Detection Fraction



(e) AERAWS Map



(f) AERAWS Detection Fraction

Figure 8.23: SD lightning map under consideration of the E-field lightning flag on the left. The field mills are marked with a green star. The position of the SD lightnings in CDAS CS coincident with an IsTS flag are marked with a black asterisk, the ones without with a red asterisk. On the right the percentage of SD lightnings with an IsTS flag is shown against the distance to the E-field mill. The error is calculated by $1/\sqrt{N}$. In red the efficiency is fitted with a linear function.

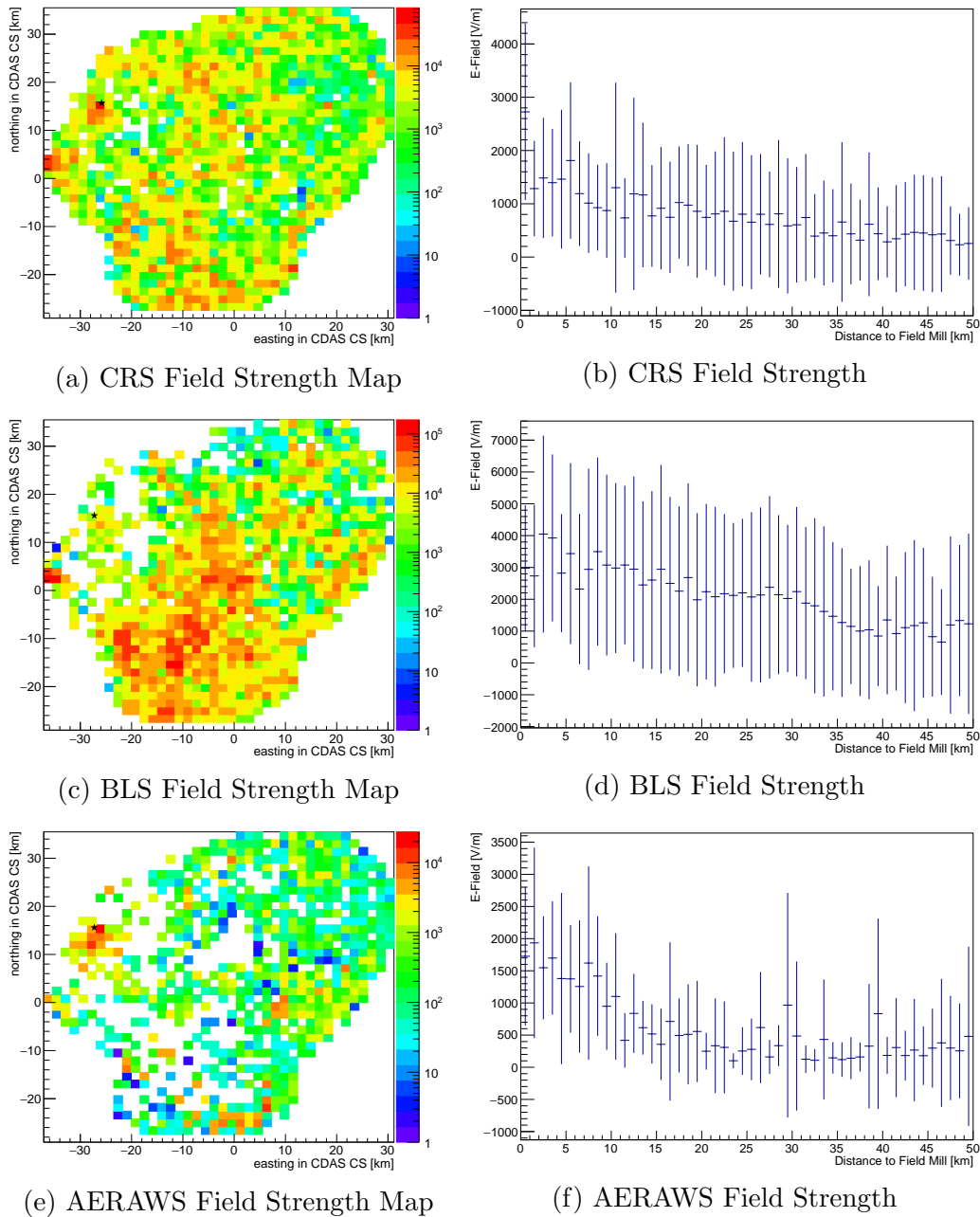


Figure 8.24: On the left the measured field strength as color scale for the lightnings from figure 8.23 at each field mill are plotted in CDAS CS. The position of the field mill is marked with a black star. On the right the profile of the field strength distribution with respect to the distance is shown.

8.4.3 Comparison to Lightning Detection System

After the comparison of the E-field data to the SD lightning flag, this paragraph will do a similar analysis for the lightning detection system based on the LDS. To reduce the number of mis-reconstructed lightnings, only lightnings reconstructed by at least four stations within a radius of 60 km around the E-field mills were selected.

The first analysis takes the lightning periods where at least four lightning detection stations were available and checks if within each lightning period, given from the E-field mills, there was an LDS reconstructed lightning. Table 8.11 gives the number of periods and the number and fraction of the ones which had a lightning within:

| Stations with IsTS | #Periods | #with Lightning | Percentage [%] |
|--------------------|----------|-----------------|----------------|
| CRS | 22 | 7 | 31 |
| AERAWS | 13 | 6 | 46 |
| CRS & AERAWS | 7 | 5 | 71 |

Table 8.11: The tabular shows the number of lightning periods from 01.01.2015 till 27.10.2015 for the different field mills with an IsTS-flag, and the number / percentage of periods with lightnings detected in a radius of 60 km with at least four stations.

The statistics are very low, but one can see a compatible behaviour for the field mills with respect to the comparison to SD Fig. 8.9, but taking only the coincident periods in both stations leads to a higher detection fraction, which had only a small impact in the SD analysis.

The next step is to calculate the detection fraction the other way round. Table 8.11 gives the number of detected LDS lightnings within a thunderstorm period of the E-field mills. With the same argument as for the SD analysis we do not expect a high detection fraction for all lightnings, but the resulting number is with only 14% within a range of 25 km much lower than expected from the previous section. Figure 8.23 takes the lightning positions into account and plots them with a differentiation between those which have an IsTS flag or not. Additionally the fraction of the lightnings with IsTS flag is plotted with respect to the distance to the field mill. For the small dataset of lightnings with four stations taken into account the error bars are large. Never the less a trend is visible. Even for the very nearby events only a detection-efficiency lower than 50% could be achieved. One reason could

| E-field mill | #Lightnings | #IsTS | Percentage [%] |
|---------------------|--------------------|--------------|-----------------------|
| CRS | 357 | 46 | 13 |
| AERAWS | 281 | 40 | 14 |
| CRS or AERAWS | 380 | 55 | 14 |

Table 8.12: The tabular shows number of detected lightnings within a distance of 25 km to the field mills, and the number / percentage of periods with an IsTS-flag for the different E-field mills.

be, that these lightnings are mis-reconstructed, or the LDS are much more sensitive than the field mills. Fitting a linear function to the data leads to a maximum detection efficiency of $31\pm 19\%$ for the CRS and $54\pm 23\%$ for the AERAWS. The constant rate of coincidence by chance for distances larger than ~ 25 km is about 5%. All numbers are about the half of the result for the SD analysis.

The measured field strength at each field mill for each lightning is plotted in figure 8.26. As expected from the previous analysis for the SD lightning flags, one expects a decrease in the field strength with the distance. For the AERAWS the near by events show a high field strength, which gets lower with the distance, but for the CRS the nearby events show a huge variation.

The data of the E-field mill show only a significant lightning detection within a small distance. The detection fraction with respect to the distance of the SD lightnings is about twice the one from the lightning detection systems. The field mill mounted at the BLS shows a different behaviour as the same device redeployed as AERAWS and the CRS, while AERAWS and CRS are compatible. The detection of lightnings is more correlated for the set up with CRS and AERAWS than for the CRS and BLS due to the lower distance of the stations to each other.

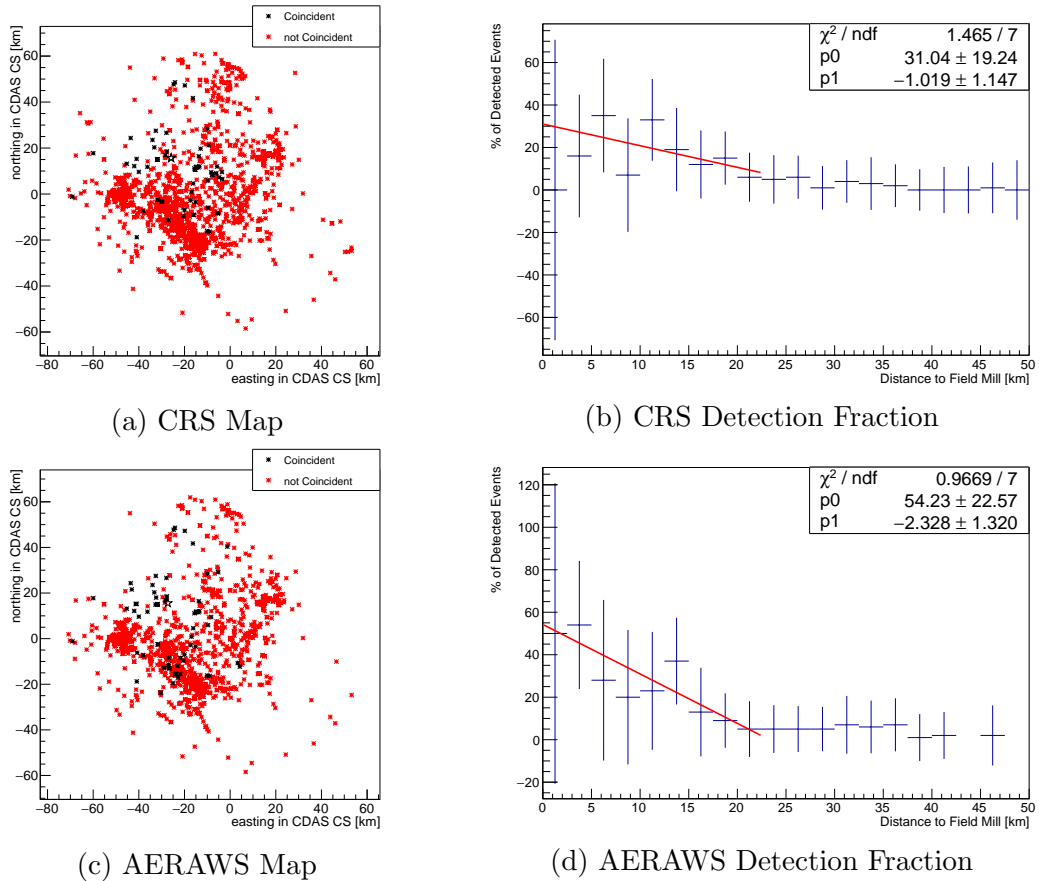


Figure 8.25: LD lightning map under consideration of the E-field lightning flag on the left. The field mills are marked with a green star. The position of the LD lightnings in CDAS CS coincident with an IsTS flag are marked with a asterisk, the ones without a red asterisk. On the right the percentage of LD lightnings with an IsTS flag is shown against the distance to the E-field mill. The error is calculated by $1/\sqrt{N}$. In red the efficiency is fitted with a linear function.

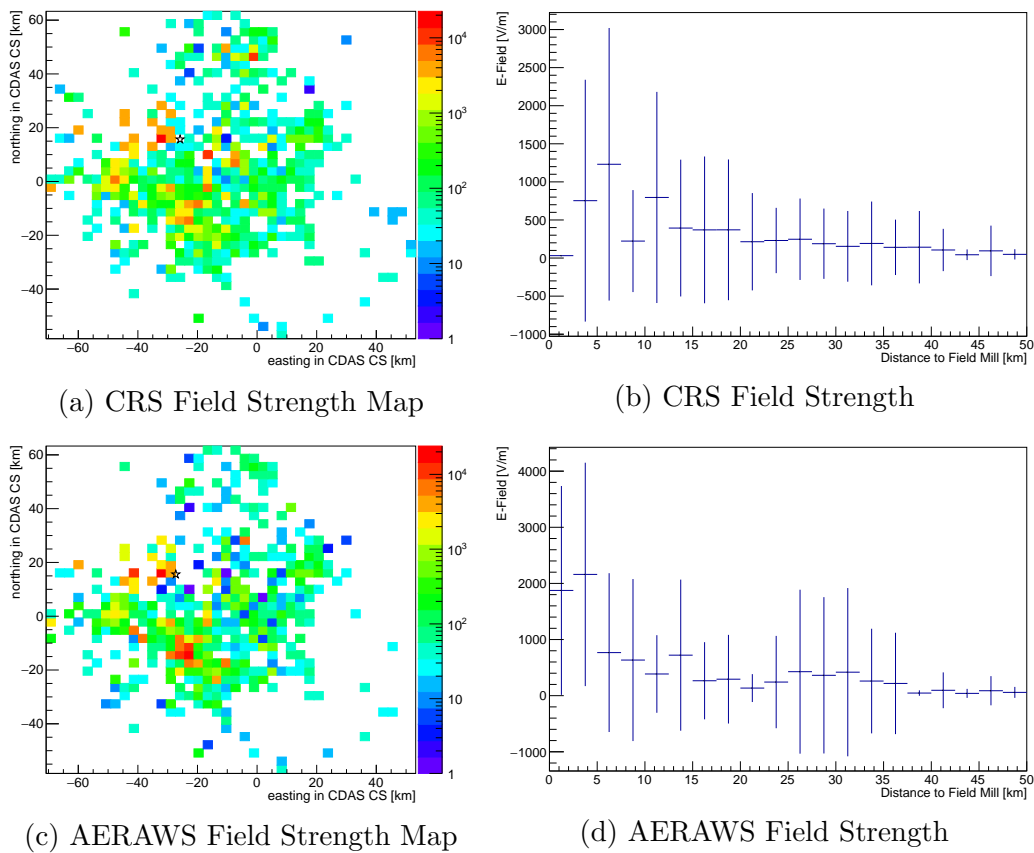


Figure 8.26: On the left the measured field strength as color scale for the lightnings from figure 8.25 at each field mill are plotted in CDAS CS. The field mills are marked with a green star. On the right the profile of the field strength distribution with respect to the distance. For bins with more than one entry the error bars show the spread.

CHAPTER 8. LIGHTNING DATA COMPARISON

Chapter 9

SD Lightning Trigger

Based on the LDS Lightning reconstruction an additional SD trigger was developed to lower the energy threshold, to the region where the RREA mechanism should take place ($E \geq 10^{16}$ eV). With this new trigger it is possible to read out single SD stations, if a lightning was detected near by. This is not possible with the standard triggers.

The reconstruction algorithm, running on the monitoring database, sends immediately an UDP message to CDAS, containing the position and time of the lightning. The lightning CDAS trigger was implemented on September 26, 2015, asking for up to one trigger per minute, within 5 km distance of a lightning strike and a time window of $[-1 \text{ ms}; +5\mu\text{s}]$. Single stations with a trigger within the cut values are read out for later analysis. The reduction to only one event per minute is implemented to reduce the amount of communication.

Since the external lightning trigger is implemented in the SD data acquisition it is now possible to perform studies on the correlation of lightnings and cosmic rays. First analysis for a few weeks have not shown a clear signal up to now, but also do not exclude a correlation. Figure 9.1 shows the area over peak (A/P) distribution for a random event selection and the lightning events. For the random data one expects a distribution around one, but for events with a cosmic ray signal a wider trace resulting in a larger A/P value [139] is expected. Therefore, events with $A/P > 1.3$ are selected. For the first data sample 1.3 events over the cut were expected and two measured. The traces of the two selected events show no special feature. By getting more statistics within one year a first conclusion can be expected. [140]

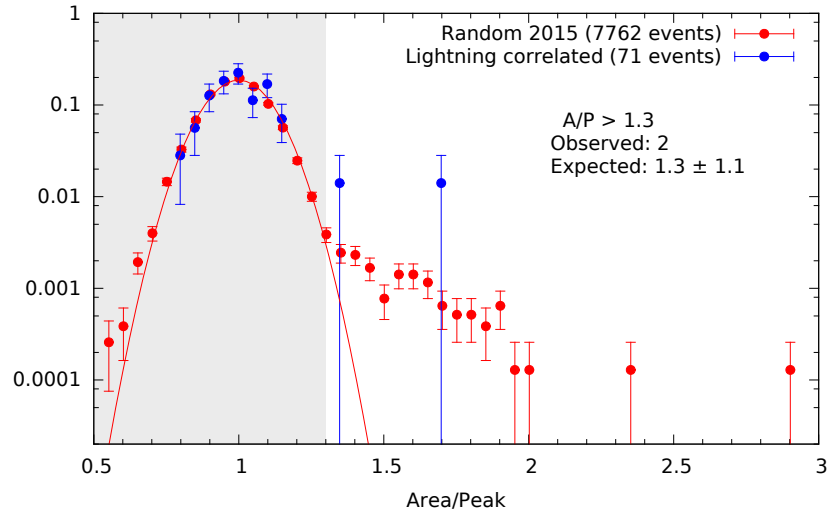


Figure 9.1: First analysis of SD data gained with the lightning trigger. Plotted is the area over peak distribution for random events in red and the lightning events in blue, from [140].

Chapter 10

Outlook

The lightning detection system provides data which can be used to gain additional information for interdisciplinary science at the Pierre Auger Observatory, as the study of Elves or SD-rings which will be described in this section.

Up to now only the time information of the lightning detection system is used. But the detector traces should contain additional information as the polarity and the strength of the lightning strike.

10.1 Additional Lightning Information

The Check-Up System described in section 8.1 delivered not only the position and time of the lightning events, but also the polarisation (positive and negative) and a classification of the strength of the lightning (middle, strong, very strong). As they used the Boltek StormTracker, it is worth to perform studies for our data to get access to these parameters.

10.1.1 Polarisation

Since the reconstruction of the lightning position is working, it is possible to calculate the direction θ of the lightning strike with respect to the detection device. This opens the possibility to calculate a source trace S_{source} from both polarisations S_{NS} and S_{EW} .

$$S_{\text{NS}} = \sin(\theta) \cdot S_{\text{source}} \text{ and } S_{\text{EW}} = \cos(\theta) \cdot S_{\text{source}} \quad (10.1)$$

Expecting a bipolar pulse in the trace, one can perform a classification by checking if the the maximum is first or the minimum. These classification

can be compared for the data measured in Wuppertal with the polarisation given from the CheckUp-System and than applied to the data in Argentina.

10.1.2 Lightning Strength

Additionally to the polarisation the strength of the lightning strike can be obtained. For that purpose it is necessary to fold the detected trace with the directional acceptance of the detector and with the loss due to the distance. This results in the source trace. Expecting a correlation of the strength of the lightning and the emitted energy in the pulse, a classification of the lightning strength should be possible by the amplitude. Again the data in Wuppertal can be classified by comparing them to the Check-Up data and the results can be applied to the data in Argentina. But for that purpose one has to keep in mind, that not all cables from the antenna to the PCI card have the same length, and additional calibrations are required.

10.2 Interpolation

An other improvement of the reconstruction accuracy could perhaps be achieved by interpolating the signal within the time bins (125 ns) of the detector traces before calculating the cross correlation factor, compare section 6.3.

10.3 Elves

After looking into the traces to gain more parameters for each lightning event, this paragraph will mention the possibility to gain additional information for other fields studied at the Pierre Auger Observatory, as for example Elves or later SD-rings and the possible correlation of cosmic rays and lightnings.

Elves are part of the bigger group of Transient Luminous Events (TLE), described in section 5.5 and created in the D-layer of the ionosphere in a height of ~ 90 km with a lateral size of up to 600 km [141]. The duration of < 1 ms makes them difficult to observe. But it was shown, that the fluorescence detectors are able to detect them [142] and the FD-lightning rejection trigger was modified to increase the number of detected Elves. Figure 10.1 shows the altitude and the characteristic shape of different TLEs. The images of Elves in the FD Telescopes is given in figure 10.2.

A rough correlation study has shown, that for about 30% of the detected Elves LDS data are available [143]. Further studies are currently in progress.

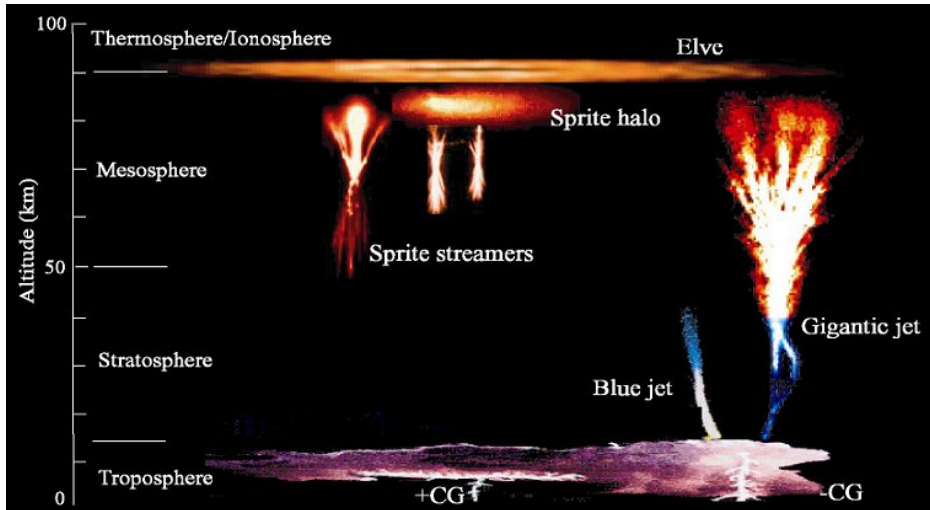


Figure 10.1: Sketch of TLE types and their height in the atmosphere, from [112].

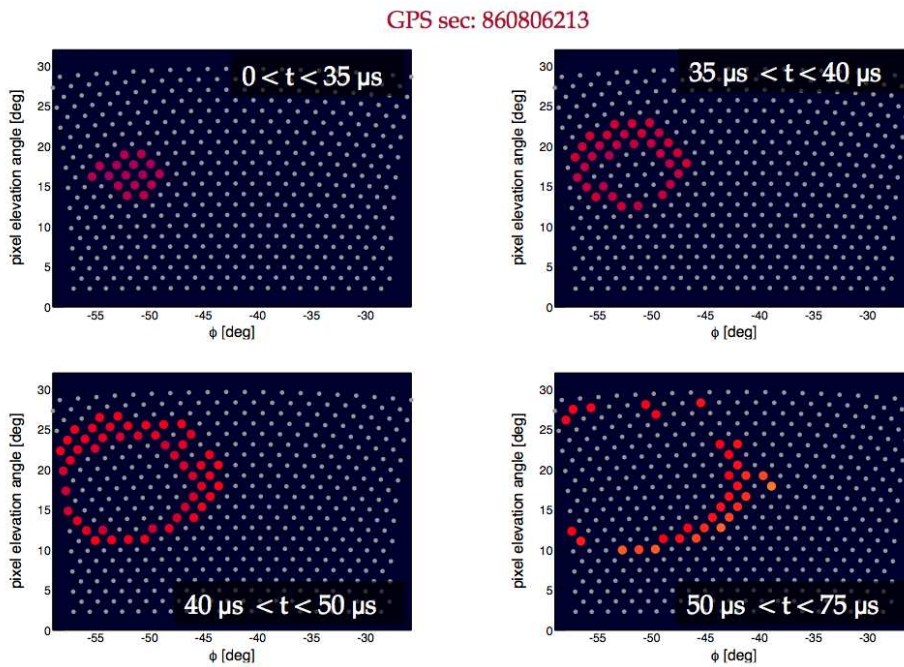


Figure 10.2: Example of an Elve detected with FD in a distance of 580 km from the observatory in a height of about 80 km. The four plots are consecutive time windows as indicated and shown the evolution with time [142].

10.4 SD-Rings

In the SD data strange events were found, which had a ring shape, figure 10.3 and a longer duration of $\sim 10\mu\text{s}$ compared to the signal of cosmic rays which last for $\sim 0.1\mu\text{s}$, figure 10.4.

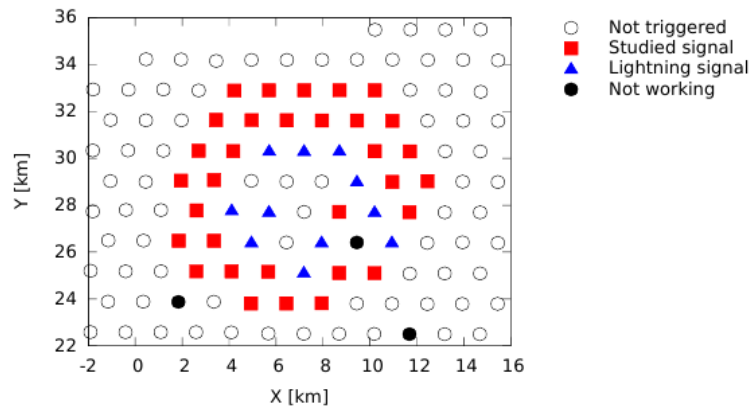


Figure 10.3: Shape of SD event 4067441 as detected with the surface detector. The triggered stations are distributed in a ring shape and some of the stations have a lightning signal, from [144].

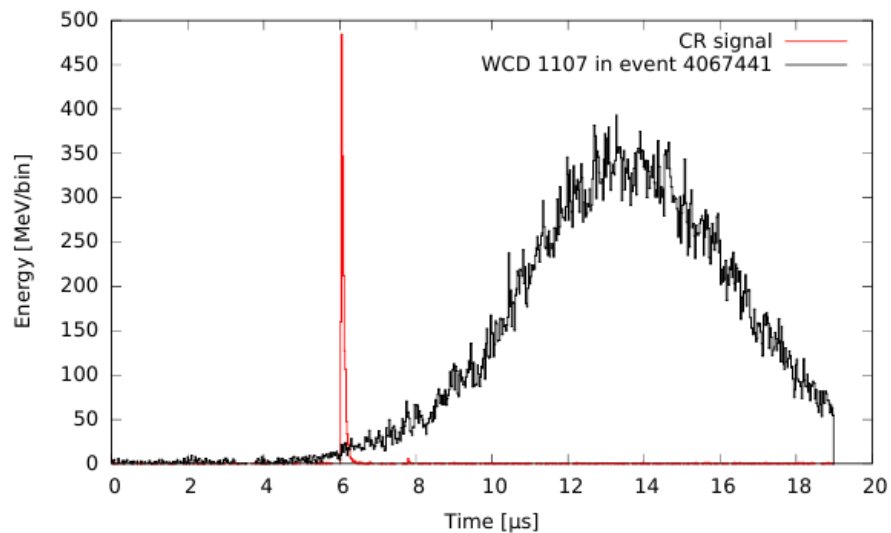


Figure 10.4: Trace of SD Event 4067441 (black) in comparison to a typical CR signal (red), from [144].

These SD-ring events could be related to TLE events. A correlation to lightnings detected with the WWLLN was shown [144]. First checks indicate, that for most of the SD-ring events lightning information from the lightning detection system in at least one station is available. These data can provide additional information of the events. Further studies are in progress [140].

CHAPTER 10. OUTLOOK

Chapter 11

Summary

Within this thesis a lightning detection system has been developed and been compared to different additional lightning detection systems available at the Pierre Auger Observatory in Argentina.

The accuracy of the reconstructed position is in the same order as the uncertainty of the systems compared to, at least for events near by the observatory. From the comparison to the WWLLN data and simulations it follows, that the uncertainty increases with the distance. The directional accuracy depends on the detector geometry and is overall about $1.7 \pm 0.1^\circ$.

The timing is compatible with the other systems, but with a significant shift with respect to the SD time, which cannot be confirmed with the WWLLN data. The lightning precedes the SD lightning flag, which can be a physical reason and enables to distinguish the EAS data and the lightning initiated noise in the SD data in later analysis.

In addition a lightning detection based on the E-field data was implemented in the Auger online monitoring, and the different lightning systems have been compared to each other. The detection efficiency of lightnings with the E-field mills decreases fast with the distance, but for lightnings within the array it is from simulations < 20 m and from the comparison with the SD lightnings within the 1.5 km distance of the SD stations. In total the agreement for near by events between SD and the E-field data was better than for E-field and the reconstruction with the lightning detection system.

Only 14% of the SD lightning events triggered at least three LDS within the uptime of the system, which will be increased by running a monitoring script on each lightning PC, that restarts the lightning detection if it is not

CHAPTER 11. SUMMARY

running properly. With a more stable running system and the additional detectors this number will increase.

A new SD Trigger has been developed, which enables the study of a correlation between cosmic rays and lightnings, which would be expected from the relativistic runaway electron avalanches mechanism. Up to now, there was, due to the low statistic, no conclusion possible.

In summary, it was shown, that the different lightning detection systems are working and especially the new lightning reconstruction systems provides the capability of additional studies in the future, as proving lightning-EAS connection, or more informations for current studies, as the SD-rings or Elves.

CHAPTER 11. SUMMARY

Appendix

Appendix A

MySQL Table Structure

Table A.1: Structure of table LightningDetectionData

| Field | Type | Null | Default |
|------------------|-----------|------|-------------------|
| <i>Time</i> | timestamp | Yes | CURRENT_TIMESTAMP |
| <i>usec</i> | int(10) | Yes | 0 |
| GPSSec | int(11) | Yes | 0 |
| GPSns | int(11) | Yes | 0 |
| GPSAccuracy | int(11) | Yes | 0 |
| <i>Site</i> | char(2) | Yes | NULL |
| Direction | float | Yes | NULL |
| Distance | float | Yes | NULL |
| AveragedDistance | float | Yes | NULL |

Table A.2: Structure of table LightningDetectionEvents

| Field | Type | Null | Default |
|---------------|---------|------|---------|
| <i>GPSSec</i> | int(11) | Yes | 0 |
| <i>GPSns</i> | int(11) | Yes | 0 |
| PositionX | int(11) | Yes | NULL |
| PositionY | int(11) | Yes | NULL |

Table A.3: Structure of table LightningDetectionLifetime

| Field | Type | Null | Default |
|-------------|-----------|------|-------------------|
| <i>Time</i> | timestamp | Yes | CURRENT_TIMESTAMP |
| <i>Site</i> | char(2) | Yes | NULL |

APPENDIX A. MYSQL TABLE STRUCTURE

Bibliography

- [1] Viktor F. Hess. Über Beobachtungen der durchdringenden Strahlung bei sieben Freiballonfahrten. *Physik. Zeitschr.* 13, pages 1084–1091, 1912.
- [2] VF Hess Society, Schloss Pöllau/Austria.
- [3] P. Auger et al. Extensive Cosmic-Ray Showers. *Reviews of Modern Physics* 11, pages 288–291, 1939.
- [4] C.D. Anderson. The Positive Electron. *Physical Review* 43 (6), pages 491–494, 1933.
- [5] C.D. Anderson S.H. Neddermeyer. Note on the Nature of Cosmic-Ray Particles. *Physical Review* 51, pages 884–886, 1937.
- [6] D. Kuempel. PhD thesis, Bergische Universität Wuppertal, 2011.
- [7] J. Neuser. PhD thesis, Bergische Universität Wuppertal, 2015.
- [8] J. W. Cronin, T. K. Gaisser, and S. P. Swordy. Cosmic Rays at the Energy Frontier. *Scientific American*, pages 44–49, 1997.
- [9] D. Ravnani. Measurement of the energy spectrum of cosmic rays above 10¹⁷ eV using the AMIGA 750 m surface detector array of the Pierre Auger Observatory. *Proceedings of the 33th International Cosmic Ray Conference, Rio de Janeiro, Brazil*, 2013.
- [10] The KASCADE-Grande Collaboration. Cosmic Rays in the Knee-Region - Recent Results from KASCADE. *Acta Physica Polonica B* 35, pages 1799–1812, 2004.
- [11] A. Hillas. The Origin of Ultra-High-Energy Cosmic Rays. *Annual Review of Astronomy and Astrophysics* 20, pages 425–444, 1984.

BIBLIOGRAPHY

- [12] V. Berezhinsky, A. Gazizov, and S. Grigorieva. Propagation and signatures of ultra high energy cosmic rays. *Nucl. Phys. Proc. Suppl.*, 136:147–158, 2004.
- [13] Kenneth Greisen. End to the cosmic ray spectrum? *Phys. Rev. Lett.*, 16:748–750, 1966.
- [14] G. T. Zatsepin and V. A. Kuzmin. Upper limit of the spectrum of cosmic rays. *JETP Lett.*, 4:78–80, 1966. [Pisma Zh. Eksp. Teor. Fiz.4,114(1966)].
- [15] Thomas K. Gaisser and Todor Stanev. High-energy cosmic rays. 2005.
- [16] W.D. Apel, J.C. Arteaga, A.F. Badea, K. Bekk, J. Blümer, H. Bozdog, I.M. Brancus, M. Brüggemann, P. Buchholz, F. Cossavella, K. Daumiller, V. de Souza, P. Doll, R. Engel, J. Engler, M. Finger, D. Fuhrmann, H.J. Gils, R. Glasstetter, C. Grupen, A. Haungs, D. Heck, J.R. Hörandel, T. Huege, P.G. Isar, K.-H. Kampert, D. Kang, D. Kachelbick, H.O. Klages, Y. Kolotaev, P. Luczak, H.J. Mathes, H.J. Mayer, J. Milke, B. Mitrica, S. Nehls, J. Oehlschläger, S. Ostapchenko, S. Over, M. Petcu, T. Pierog, H. Rebel, M. Roth, G. Schatz, H. Schieler, F. Schröder, O. Sima, M. Stümpert, G. Toma, H. Ulrich, J. van Buren, W. Walkowiak, A. Weindl, J. Wochele, M. Wommer, and J. Zabierowski. Energy spectra of elemental groups of cosmic rays: Update on the {KASCADE} unfolding analysis. *Astroparticle Physics*, 31(2):86 – 91, 2009.
- [17] K.-H. Kampert and M. Unger. Measurements of the cosmic ray composition with air shower experiments. *Astroparticle Physics*, 35:660–678, May 2012.
- [18] *The Pierre Auger Observatory: Contributions to the 34th International Cosmic Ray Conference (ICRC 2015)*, 2015.
- [19] ENRICO Fermi. On the origin of the cosmic radiation. *Phys. Rev.*, 75:1169–1174, Apr 1949.
- [20] T. K. Gaisser. *Cosmic Rays And Particle Physics*. Cambridge University Press, 1990.
- [21] R. D. Blandford and J. P. Ostriker. Particle Acceleration by Astrophysical Shocks. *Astrophys. J.*, 221:L29–L32, 1978.

-
- [22] Hans Blümer and Karl-Heinz Kampert. Die suche nach den quellen der kosmischen strahlung: Antworten versprechen die luftschauerexperimente kascade und auger. *Physik Journal*, 56(3):39–45, 2000.
- [23] Diego F. Torres and Luis A. Anchordoqui. Astrophysical origins of ultrahigh energy cosmic rays. *Rept. Prog. Phys.*, 67:1663–1730, 2004.
- [24] Christopher T. Hill. Monopolonium. *Nucl. Phys.*, B224:469, 1983.
- [25] M. B. Hindmarsh and T. W. B. Kibble. Cosmic strings. *Rept. Prog. Phys.*, 58:477–562, 1995.
- [26] V. Berezhinsky, M. Kachelriess, and A. Vilenkin. Ultrahigh-energy cosmic rays without GZK cutoff. *Phys. Rev. Lett.*, 79:4302–4305, 1997.
- [27] Michael Birkel and Subir Sarkar. Extremely high-energy cosmic rays from relic particle decays. *Astropart. Phys.*, 9:297–309, 1998.
- [28] Z. Fodor and S. D. Katz. Grand unification signal from ultrahigh-energy cosmic rays? *Phys. Rev. Lett.*, 86:3224–3227, 2001.
- [29] Thomas J. Weiler. Resonant Absorption of Cosmic Ray Neutrinos by the Relic Neutrino Background. *Phys. Rev. Lett.*, 49:234, 1982.
- [30] Thomas J. Weiler. Cosmic ray neutrino annihilation on relic neutrinos revisited: A Mechanism for generating air showers above the Greisen-Zatsepin-Kuzmin cutoff. *Astropart. Phys.*, 11:303–316, 1999.
- [31] Daniele Fargion, B. Mele, and A. Salis. Ultrahigh-energy neutrino scattering onto relic light neutrinos in galactic halo as a possible source of highest energy extragalactic cosmic rays. *Astrophys. J.*, 517:725–733, 1999.
- [32] Pijushpani Bhattacharjee and Gunter Sigl. Origin and propagation of extremely high-energy cosmic rays. *Phys. Rept.*, 327:109–247, 2000.
- [33] C. Bleve for the Pierre Auger Collaboration. Update of the neutrino and photon limits from the pierre auger observatory. *Proceedings of the 34th International Cosmic Ray Conference, The Hague, The Netherlands*, 2015.
- [34] John D. Barrow, Pedro G. Ferreira, and Joseph Silk. Constraints on a primordial magnetic field. *Phys. Rev. Lett.*, 78:3610–3613, 1997.

BIBLIOGRAPHY

- [35] Philipp P. Kronberg. Extragalactic magnetic fields. *Rept. Prog. Phys.*, 57:325–382, 1994.
- [36] Arno A. Penzias and Robert Woodrow Wilson. A Measurement of excess antenna temperature at 4080-Mc/s. *Astrophys. J.*, 142:419–421, 1965.
- [37] Denis Allard, M. Ave, N. Busca, M. A. Malkan, A. V. Olinto, E. Parizot, F. W. Stecker, and T. Yamamoto. Cosmogenic Neutrinos from the propagation of Ultrahigh Energy Nuclei. *JCAP*, 0609:005, 2006.
- [38] J. W. Cronin. Cosmic rays: The most energetic particles in the universe. *Rev. Mod. Phys.*, 71:S165–S172, 1999.
- [39] John Linsley. Evidence for a primary cosmic-ray particle with energy 10^{20} -eV. *Phys. Rev. Lett.*, 10:146–148, 1963.
- [40] Douglas R. Bergman. Observation of the GZK Cutoff Using the HiRes Detector. *Nucl. Phys. Proc. Suppl.*, 165:19–26, 2007. [19(2006)].
- [41] J. Abraham et al. Measurement of the energy spectrum of cosmic rays above 10^{18} eV using the Pierre Auger Observatory. *Phys. Lett.*, B685:239–246, 2010.
- [42] N. Hayashida et al. The Anisotropy of cosmic ray arrival directions around 10^{18} -eV. *Astropart. Phys.*, 10:303–311, 1999.
- [43] J. A. Bellido, R. W. Clay, B. R. Dawson, and M. Johnston-Hollitt. Southern hemisphere observations of a 10^{18} -eV cosmic ray source near the direction of the galactic center. *Astropart. Phys.*, 15:167–175, 2001.
- [44] M. Aglietta et al. Anisotropy studies around the Galactic Centre at EeV energies with the Auger Observatory. *Astropart. Phys.*, 27:244–253, 2007.
- [45] M. P. Veron-Cetty and P. Veron. A catalogue of quasars and active nuclei: 12th edition. *Astron. Astrophys.*, 455:773–777, 2006.
- [46] J. Abraham et al. Correlation of the highest energy cosmic rays with nearby extragalactic objects. *Science*, 318:938–943, 2007.
- [47] P. Abreu, M. Aglietta, E. J. Ahn, D. Allard, I. Allekotte, J. Allen, J. Alvarez Castillo, J. Alvarez-Muñiz, M. Ambrosio, A. Aminaei, and et al. Update on the correlation of the highest energy cosmic rays with nearby extragalactic matter. *Astroparticle Physics*, 34:314–326, 2010.

- [48] Alexander Aab et al. Searches for Anisotropies in the Arrival Directions of the Highest Energy Cosmic Rays Detected by the Pierre Auger Observatory. *Astrophys. J.*, 804(1):15, 2015.
- [49] W. Heitler. *The Quantum Theory of Radiation*. Dover, New York, third edition, 1984.
- [50] D. Heck, J. Knapp, J. N. Capdevielle, G. Schatz, and T. Thouw. *CORSIKA: a Monte Carlo code to simulate extensive air showers*. February 1998.
- [51] T. K. Gaisser and A. M. Hillas. Reliability of the method of constant intensity cuts for reconstructing the average development of vertical showers. *International Cosmic Ray Conference*, 8:353–357, 1977.
- [52] M. Nagano and Alan A. Watson. Observations and implications of the ultrahigh-energy cosmic rays. *Rev. Mod. Phys.*, 72:689–732, 2000.
- [53] Johannes Blümer, Ralph Engel, and Jörg R. Hörandel. Cosmic rays from the knee to the highest energies. *Progress in Particle and Nuclear Physics*, 63(2):293 – 338, 2009.
- [54] F. Arciprete et al. AIRFLY: Measurement of the air fluorescence radiation induced by electrons. *Nucl. Phys. Proc. Suppl.*, 150:186–189, 2006. [,186(2006)].
- [55] M. S. Longair. *HIGH-ENERGY ASTROPHYSICS. AN INFORMAL INTRODUCTION FOR STUDENTS OF PHYSICS AND ASTRONOMY*. 1981.
- [56] P. Abreu et al. The Pierre Auger Observatory II: Studies of Cosmic Ray Composition and Hadronic Interaction models. In *Proceedings, 32nd International Cosmic Ray Conference (ICRC 2011)*, volume 3, page 208, 2011.
- [57] D. J. Bird. Detection of a Cosmic Ray with Measured Energy Well Beyond the Expected Spectral Cutoff due to Cosmic Microwave Radiation. 1994.
- [58] G. A. Askar’yan. Excess negative charge of an electron-photon shower and its coherent radio emission. *Sov. Phys. JETP*, 14(2):441–443, 1962. [*Zh. Eksp. Teor. Fiz.*41,616(1961)].
- [59] H. Falcke et al. Detection and imaging of atmospheric radio flashes from cosmic ray air showers. *Nature*, 435:313–316, 2005.

BIBLIOGRAPHY

- [60] A. Belletoile. First results of the new Autonomous Antenna Array of the CODALEMA radio detection experiment. *International Cosmic Ray Conference*, 1:231, 2011.
- [61] A. M. van den Berg. Radio detection of cosmic rays at the southern Auger Observatory. *ArXiv e-prints*, aug 2009.
- [62] The LOFAR Collaboration. LOFAR: The LOw-Frequency ARray. *Astronomy & Astrophysics*, 556:A2, aug 2013.
- [63] D. Kostunin et al. Tunka-Rex: Status and results of the first measurements. *Nucl. Instrum. Meth.*, A742:89–94, 2014.
- [64] I. Lerche. Theory of radio pulses from cosmic ray air showers. *Nature*, 215:268–269, 1966.
- [65] F. D. Kahn and I. Lerche. Radiation from cosmic ray air showers. *Proceedings of the Royal Society of London A: Mathematical, Physical and Engineering Sciences*, 289(1417):206–213, 1966.
- [66] Harm Schoorlemmer. *Tuning in on cosmic rays. Polarization of radio signals from air showers as a probe of emission mechanisms*. PhD thesis, Nijmegen U., 2012.
- [67] W. N. Charman. Atmospheric electric field as a possible cause of radio pulses from extensive air showers. *Nature*, 215, 1967.
- [68] M. Ender for the LOPES Collaboration. Radio emission of extensive air showers during thunderstorms. *Proceedings of the 31th International Cosmic Ray Conference, Lodz, Poland*, 2009.
- [69] J. Jackson. *Classical Electrodynamics*, volume 2. John Wiley & Sons Inc., 1975.
- [70] Horneffer et al. Primary Particle Energy Calibration of the EAS Radio Pulse Height. *Proceedings of the International 30th Cosmic Ray Conference, Merida, Mexico*, 4:83–86, 2007.
- [71] P. W. Gorham et al. Observations of Microwave Continuum Emission from Air Shower Plasmas. *Phys. Rev.*, D78:032007, 2008.
- [72] R. Šmída et al. First Experimental Characterization of Microwave Emission from Cosmic Ray Air Showers. *Phys. Rev. Lett.*, 113(22):221101, 2014.

-
- [73] J. Alvarez-Muñiz, A. Berlin, M. Bogdan, M. Boháčová, C. Bonifazi, W. R. Carvalho, Jr., J. R. T. de Mello Neto, P. Facal San Luis, J. F. Genat, N. Hollon, E. Mills, M. Monasor, P. Privitera, L. C. Reyes, B. Rouille d'Orfeuill, E. M. Santos, S. Wayne, C. Williams, E. Zas, and J. Zhou. Search for microwave emission from ultrahigh energy cosmic rays. *Proceedings of the 33th International Cosmic Ray Conference, Rio de Janeiro, Brazil*, 86(5):051104, sep 2012.
- [74] Christopher Williams. Microwave detection of cosmic ray air showers at the pierre auger observatory. *Physics Procedia*, 37:1341 – 1348, 2012. Proceedings of the 2nd International Conference on Technology and Instrumentation in Particle Physics (TIPP 2011).
- [75] Google. Google Earth, December 2015. <http://maps.google.de/>, ©2015 Google, INEGI.
- [76] The Pierre Auger Collaboration. Auger Homepage. www.auger.org.ar.
- [77] The Pierre Auger Collaboration. The fluorescence detector of the pierre auger observatory. *Nuclear Instruments and Methods in Physics Research Section A: Accelerators, Spectrometers, Detectors and Associated Equipment*, 620(2–3):227 – 251, 2010.
- [78] S. Saffi, 2014. www.auger.org.ar.
- [79] The Pierre Auger Collaboration. Depth of maximum of air-shower profiles at the Pierre Auger Observatory. I. Measurements at energies above $10^{17.8}$ eV. *Phys. Rev.*, D90(12):122005, 2014.
- [80] Laura Valore. Atmospheric Aerosol Attenuation Measurements at the Pierre Auger Observatory. In *International Workshop on Atmospheric Monitoring for High-Energy Astroparticle Detectors (Atmo-HEAD 2013) Gif-sur-Yvette, France, June 10-12, 2013*, 2014.
- [81] S. Y. BenZvi et al. The Lidar System of the Pierre Auger Observatory. *Nucl. Instrum. Meth.*, A574:171–184, 2007.
- [82] C. Bonifazi and Pierre Auger Collaboration. The angular resolution of the Pierre Auger Observatory. *Nuclear Physics B Proceedings Supplements*, 190:20–25, may 2009.
- [83] Klaus Frank Weidenhaupt. *Antenna calibration and energy measurement of ultra high energy cosmic rays with the Auger Engineering Radio*

BIBLIOGRAPHY

- Array*. PhD thesis, Aachen, 2014. Online-Ausg.: Weidenhaupt, Klaus Frank: Antenna calibration and energy measurement of ultra high energy cosmic rays with the Auger Engineering Radio Array; Aachen, Techn. Hochsch., Diss., 2014.
- [84] J. B. Eser. Verschiedene methoden der zeitkalibration für das auger engineering radio array. Diploma thesis, Karlsruhe Institute of Technology, 2013.
- [85] W.D. Apel, J.C. Arteaga, L. Bähren, K. Bekk, M. Bertaina, P.L. Biermann, J. Blümer, H. Bozdog, I.M. Brancus, P. Buchholz, S. Buitink, E. Cantoni, A. Chiavassa, K. Daumiller, V. de Souza, F. Di Pierro, P. Doll, M. Ender, R. Engel, H. Falcke, M. Finger, D. Fuhrmann, H. Gemmeke, C. Grupen, A. Haungs, D. Heck, J.R. Hörandel, A. Horneffer, D. Huber, T. Huege, P.G. Isar, K.-H. Kampert, D. Kang, O. Krömer, J. Kuijpers, K. Link, P. Luczak, M. Ludwig, H.J. Mathes, M. Melissas, C. Morello, S. Nehls, J. Oehlschläger, N. Palmieri, T. Pierog, J. Rautenberg, H. Rebel, M. Roth, C. Rühle, A. Saftoiu, H. Schieler, A. Schmidt, F.G. Schröder, O. Sima, G. Toma, G.C. Trincherro, A. Weindl, J. Wochele, M. Wommer, J. Zabierowski, and J.A. Zensus. Thunderstorm observations by air-shower radio antenna arrays. *Advances in Space Research*, 48(7):1295 – 1303, 2011.
- [86] F. G. Schröder, T. Asch, L. Bähren, J. Blümer, H. Bozdog, H. Falcke, A. Haungs, A. Horneffer, T. Huege, P. G. Isar, O. Krömer, and S. Nehls. New method for the time calibration of an interferometric radio antenna array. *Nuclear Instruments and Methods in Physics Research A*, 615:277–284, apr 2010.
- [87] Alexander Aab et al. Nanosecond-level time synchronization of autonomous radio detector stations for extensive air showers. 2015.
- [88] S. Argiro, S. L. C. Barroso, J. Gonzalez, L. Nellen, Thomas Cantzon Paul, T. A. Porter, L. Prado, Jr., M. Roth, R. Ulrich, and D. Veberic. The Offline Software Framework of the Pierre Auger Observatory. *Nucl. Instrum. Meth.*, A580:1485–1496, 2007.
- [89] C. Glaser. Energy measurement and strategy for a trigger of ultra high energy cosmic rays measured with radio technique at the pierre auger observatory. Master thesis, RWTH Aachen, 2012.
- [90] Joseph R. Dwyer and Martin A. Uman. The physics of lightning. *Physics Reports*, 534(4):147 – 241, 2014. The Physics of Lightning.

- [91] C. T. R. Wilson. On some determinations of the sign and magnitude of electric discharges in lightning flashes. *Proceedings of the Royal Society of London A: Mathematical, Physical and Engineering Sciences*, 92(644):555–574, 1916.
- [92] C. T. R. Wilson. Investigations on lightning discharges and on the electric field of thunderstorms. *Philosophical Transactions of the Royal Society of London A: Mathematical, Physical and Engineering Sciences*, 221(582-593):73–115, 1921.
- [93] Encyclopedia Britannica Online. Lightning, 2007. <http://search.eb.com/eb/article-9048228>.
- [94] Maribeth Stolzenburg, W. David Rust, Bradley F. Smull, and Thomas C. Marshall. Electrical structure in thunderstorm convective regions: 1. mesoscale convective systems. *Journal of Geophysical Research: Atmospheres*, 103(D12):14059–14078, 1998.
- [95] M.A. Uman. *The Lightning Discharge*. International Geophysics. Elsevier Science, 1987.
- [96] Blitzstrom-parameter von aufwärtsblitzen. *Bull. Schweiz. Elektrotech. Ver.*, 69(8):353–360, 1979.
- [97] Hugh J. Christian, Richard J. Blakeslee, Dennis J. Boccippio, William L. Boeck, Dennis E. Buechler, Kevin T. Driscoll, Steven J. Goodman, John M. Hall, William J. Koshak, Douglas M. Mach, and Michael F. Stewart. Global frequency and distribution of lightning as observed from space by the optical transient detector. *Journal of Geophysical Research: Atmospheres*, 108(D1):ACL 4–1–ACL 4–15, 2003. 4005.
- [98] H.J. Christian, R.J. Blakeslee, and S.J. Goodman. Lightning imaging sensor (lis) for the earth observing system. *NASA Technical Memorandum 4350, MSFC, Huntsville, AL, February*, 1992.
- [99] K.L. Cummins, E.P. Krider, and M.D. Malone. The us national lightning detection network and applications of cloud-to-ground lightning data by electric power utilities. *Electromagnetic Compatibility, IEEE Transactions on*, 40(4):465–480, Nov 1998.
- [100] W. Schulz, G. Diendorfer, S. Pedebay, and D. R. Poelman. The european lightning location system euclid – part 1: Performance validation.

BIBLIOGRAPHY

- Natural Hazards and Earth System Sciences Discussions*, 3(9):5325–5355, 2015.
- [101] C. J. Rodger, J. B. Brundell, R. L. Dowden, and N. R. Thomson. Location accuracy of long distance vlf lightning location network. *Annales Geophysicae*, 22(3):747–758, 2004.
- [102] A.V. Gurevich, L.M. Duncan, Yu.V. Medvedev, and K.P. Zybin. Radio emission due to simultaneous effect of runaway breakdown and extensive atmospheric showers. *Physics Letters A*, 301(3–4):320 – 326, 2002.
- [103] Alexander V. Gurevich and Kirill P. Zybin. Runaway breakdown and the mysteries of lightning. *Physics Today*, 58(5):37–43, 2005.
- [104] D.R. MacGorman and W.D. Rust. *The Electrical Nature of Storms*. Oxford University Press, 1998.
- [105] C T R Wilson. The electric field of a thundercloud and some of its effects. *Proceedings of the Physical Society of London*, 37(1):32D, 1924.
- [106] H.D. Betz, U. Schumann, and P. Laroche. *Lightning: Principles, Instruments and Applications: Review of Modern Lightning Research*. Springer Netherlands, 2008.
- [107] M. Le Boulch, J. Hamelin, and C. Weidman. Uhf-vhf radiation from lightning. *Electromagnetics*, 7(3-4):287–331, 1987.
- [108] F. Horner and P.A. Bradley. The spectra of atmospheric from near lightning discharges. *Journal of Atmospheric and Terrestrial Physics*, 26(12):1155 – 1166, 1964.
- [109] F J Hewitt. The study of lightning streamers with 50 cm radar. *Proceedings of the Physical Society. Section B*, 66(10):895, 1953.
- [110] E. L. Kosarev, V. G. Zatspein, and A. V. Mitrofanov. Ultrahigh frequency radiation from lightnings. *Journal of Geophysical Research*, 75(36):7524–7530, 1970.
- [111] R. C. Franz, R. J. Nemzek, and J. R. Winckler. Television image of a large upward electrical discharge above a thunderstorm system. *Science*, 249(4964):48–51, 1990.
- [112] “TARANIS satellite to study lightning,” CNES, 2015. <https://cnes.fr/en/web/CNES-en/9128-gp-taranis-satellite-to-study-lightning.php>.

-
- [113] D.D. Sentman and E.M. Wescott. *Red Sprites and Blue Jets: Transient Electrical Effects of Thunderstorms on the Middle and Upper Atmospheres*, pages 45–55. American Geophysical Union, 2013.
- [114] C L Kuo, A B Chen, J K Chou, L Y Tsai, R R Hsu, H T Su, H U Frey, S B Mende, Y Takahashi, and L C Lee. Radiative emission and energy deposition in transient luminous events. *Journal of Physics D: Applied Physics*, 41(23):234014, 2008.
- [115] W. L. Boeck, O. H. Vaughan, R. Blakeslee, B. Vonnegut, and M. Brook. Lightning induced brightening in the airglow layer. *Geophysical Research Letters*, 19(2):99–102, 1992.
- [116] U. S. Inan, S. A. Cummer, and R. A. Marshall. A survey of elf and vlf research on lightning-ionosphere interactions and causative discharges. *Journal of Geophysical Research: Space Physics*, 115(A6):n/a–n/a, 2010. A00E36.
- [117] Alfred B. Chen, Cheng-Ling Kuo, Yi-Jen Lee, Han-Tzong Su, Rue-Ron Hsu, Jyh-Long Chern, Harald U. Frey, Stephen B. Mende, Yukihiko Takahashi, Hiroshi Fukunishi, Yeou-Shin Chang, Tie-Yue Liu, and Lou-Chuang Lee. Global distributions and occurrence rates of transient luminous events. *Journal of Geophysical Research: Space Physics*, 113(A8):n/a–n/a, 2008. A08306.
- [118] E. M. Wescott, D. Sentman, D. Osborne, D. Hampton, and M. Heavner. Preliminary results from the sprites94 aircraft campaign: 2. blue jets. *Geophysical Research Letters*, 22(10):1209–1212, 1995.
- [119] E. M. Wescott, D. D. Sentman, M. J. Heavner, D. L. Hampton, D. L. Osborne, and O. H. Vaughan. Blue starters brief upward discharges from an intense arkansas thunderstorm. *Geophysical Research Letters*, 23(16):2153–2156, 1996.
- [120] William L. Boeck, Otha H. Vaughan, Richard J. Blakeslee, Bernard Vonnegut, Marx Brook, and John McKune. Observations of lightning in the stratosphere. *Journal of Geophysical Research: Atmospheres*, 100(D1):1465–1475, 1995.
- [121] W. A. Lyons Ccm, T. E. Nelson, R. A. Armstrong, V. P. Pasko, and M. A. Stanley. Upward Electrical Discharges From Thunderstorm Tops. *Bulletin of the American Meteorological Society*, 84:445–454, apr 2003.

BIBLIOGRAPHY

- [122] Victor P. Pasko, Mark A. Stanley, John D. Mathews, Umran S. Inan, and Troy G. Wood. Electrical discharge from a thundercloud top to the lower ionosphere. *Nature*, 416(6877):152–154, Mar 2002.
- [123] Victor P. Pasko. Atmospheric physics: Electric jets. *Nature*, 423(6943):927–929, Jun 2003.
- [124] H. T. Su, R. R. Hsu, A. B. Chen, Y. C. Wang, W. S. Hsiao, W. C. Lai, L. C. Lee, M. Sato, and H. Fukunishi. Gigantic jets between a thundercloud and the ionosphere. *Nature*, 423(6943):974–976, Jun 2003.
- [125] Oscar A. van der Velde, Walter A. Lyons, Thomas E. Nelson, Steven A. Cummer, Jingbo Li, and James Bunnell. Analysis of the first gigantic jet recorded over continental north america. *Journal of Geophysical Research: Atmospheres*, 112(D20):n/a–n/a, 2007. D20104.
- [126] Steven A. Cummer, Jingbo Li, Feng Han, Gaopeng Lu, Nicolas Jaugey, Walter A. Lyons, and Thomas E. Nelson. Quantification of the troposphere-to-ionosphere charge transfer in a gigantic jet. *Nature Geosci*, 2(9):617–620, Sep 2009.
- [127] Paul R. Krehbiel, Jeremy A. Rioussset, Victor P. Pasko, Ronald J. Thomas, William Rison, Mark A. Stanley, and Harald E. Edens. Upward electrical discharges from thunderstorms. *Nature Geosci*, 1(4):233–237, Apr 2008.
- [128] S. Nehls. *Calibrated Measurements of the Radio Emission of Cosmic Ray Air Showers*. PhD thesis, Universität Karlsruhe, Institut für Experimentelle Kernphysik, 2008.
- [129] Boltek Homepage, 2013. <http://www.boltek.com/product/stormpci-long-range-detection-kit>.
- [130] Precision Time Protocol daemon, 2015. <http://sourceforge.net/p/ptpd/wiki/Home>.
- [131] *u-blox 6 Receiver Description, Including Protocol Specification*. u-blox AG, Zuercherstrasse 68, CH8800 Thalwil, Switzerland, April 2013.
- [132] P. Krehbiel, T. Hamlin, Y. Zhang*, J. Harlin, R. Thomas, and W. Rison. Three-dimensional total lightning observations with the lightning mapping array. In *2002 Intn'l. Lightning Detection Conf. Tucson, AZ*, October 2002.

- [133] X. Bertou. Looking for correlation between lightning and uhecr. GAP Note 2009-099.
- [134] Google. Google Earth, January 2015. <https://earth.google.de/>, US Dept. of State Geographer ©2015 Google, Image Landsat, Dafa SIO, NOAA, U.S. Navy, NGA, GEBCO.
- [135] World Wide Lightning Location Network, June 2015. <http://wwlln.net>.
- [136] Richard L Dowden, James B Brundell, and Craig J Rodger. {VLF} lightning location by time of group arrival (toga) at multiple sites. *Journal of Atmospheric and Solar-Terrestrial Physics*, 64(7):817 – 830, 2002.
- [137] R. A. Torres. Tracking thunderstorm lightning at the Pierre Auger Observatory. Bachelor Thesis, KVI, Kernfysisch Versneller Instituut, University of Groningen, 2012.
- [138] National Severe Storms Laboratory, 2013. A Severe Weather Primer: Questions and Answers about Thunderstorms”. National Oceanic and Atmospheric Administration. http://www.nssl.noaa.gov/primer/tstorm/tst_basics.html.
- [139] A.Castellina. Accuracy of signal measurements in the auger surface detector. *internal Auger note*, GAP-2003-031, 2003.
- [140] R. Bertou. private communication, 2015.
- [141] Y. N. Taranenko, U. S. Inan, and T. F. Bell. Optical signatures of lightning-induced heating of the d region. *Geophysical Research Letters*, 19(18):1815–1818, 1992.
- [142] Aurelio S. Tonachini. Observation of elves with the fluorescence detectors of the Pierre Auger Observatory. In *Proceedings, 32nd International Cosmic Ray Conference (ICRC 2011)*, volume b, page 401, 2011.
- [143] R. Mussa. private communication, 2014.
- [144] X. Bertou V. H. Purrello. Study of strange sd events detected during thunderstorms. *internal Auger note*, GAP-2015-012, 2015.

BIBLIOGRAPHY

BIBLIOGRAPHY

List of Abbreviations

| | |
|-------|-----------------------------------------|
| AERA | Auger Engineering Radio Array |
| AGN | Active Galactic Nuclei |
| BLS | Balloon Launching Station |
| CDAS | Central Data Acquisition System |
| CG | Cloud to Ground lightning |
| CMB | Cosmic Microwave Background |
| CO | Coihueco |
| CRS | Central Radio Station |
| EAS | Extensive AirShower |
| FD | Fluorescence Detector |
| GRB | Gamma Ray Bursts |
| IC | Intra Cloud lightning |
| ISM | Interstellar Medium |
| ISTS | IS ThunderStorm flag |
| LA | Loma Amarilla |
| LDF | Lateral Distribution Function |
| LDS | Lightning Detection Station |
| LF | Low Frequency |
| LIDAR | LIght Detection And Ranging |
| LL | Los Leones |
| LM | Los Morados |
| LMA | New Mexico Tech Lightning Mapping Array |
| MG | Malargüe |
| MPV | Most Probable Value |
| PMT | PhotoMultiplier Tubes |
| SD | Surface Detector |
| TDOP | Time Dilution Of Precision |
| TLE | Transient Luminous Events |
| VEM | Vertical Equivalent Muon |
| VHF | Very High Frequency |
| VLF | Very Low Frequency |
| WWLLN | World Wide Lightning Location Network |

Acknowledgement

First of all, I am very thankful to Prof. Dr. Karl-Heinz Kampert. He offered me the opportunity to work on this interesting topic within the working group and the Pierre Auger Collaboration. Beside his mentoring, he was always willing to discuss open questions.

I am grateful to Dr. Hernán Asorey for writing the second report as well as for fruitful discussions within the Cosmo-Geo meetings.

The author wishes to thank the World Wide Lightning Location Network (<http://wwlln.net>), a collaboration among over 50 universities and institutions, for providing the lightning location data used in this paper.

Besonders danken möchte ich Dr. Julian Rautenberg für seine fachliche und persönliche Unterstützung auch in stressigen Zeiten.

Mit meinen “Detektiv”-Kollegen Sven “Peter” Querchfeld und Jens “Bob” Neuser hatte ich nicht nur nette Kollegen, sondern habe in ihnen auch gute Freunde gefunden. Mögen uns noch viele offene Fragen und Rätsel zusammenführen.

Der gesamten Arbeitsgruppe der Astroteilchenphysik danke ich für die tolle Atmosphäre, sowohl bei fachlichen Diskussionen als auch beim obligatorischen Grillen. Insbesondere mit Nicole, Ruth, Sebastian, Jörg und Christan habe ich schöne Stunden verbracht. Ein Dank geht auch an Frau Schaarwächter für ihre stetige Unterstützung.

Meiner Familie, insbesondere meinen Eltern und meiner Schwiegermutter, danke ich für die Unterstützung, die ich durch sie in vielfältiger Weise erfahren habe.

Der größte Dank gebührt meiner Frau Uta, die mir stets den Rücken frei hielt und mich stetig motiviert hat die Arbeit zum Abschluss zu bringen. Die gemeinsamen Stunden bei uns im Home-Office, bei denen der größte Teil der Arbeit niedergeschrieben wurde, habe ich sehr genossen. Danke auch für unsere wundervollen Kinder Ina und Lena, die mir immer wieder zeigen, was im Leben wirklich wichtig ist und helfen den Kopf frei zu bekommen.